UNIVERSIDADE D
COIMBRA

Sandro Miguel Ribeiro Saltão

OPTIMIZATION OF THE VERTICAL SEPARATION OF MULTIPLE SCATTER EVENTS IN THE LZ DETECTOR WITH APPLICATIONS IN THE SENSITIVITY TO THE $0\nu\beta\beta$ DECAY OF ^{136}XE

Dissertação no âmbito do Mestrado de Física Nuclear e de Partículas orientada pelo Professor Doutor Alexandre Miguel Ferreira Lindote e pelo Professor Doutor Paulo Alexandre Brinca da Costa Braz e apresentada ao Departamento de Física da Faculdade de Ciências e Tecnologia da Universidade de Coimbra.

Fevereiro de 2023

FACULDADE DE
CIÊNCIAS E TECNOLOGIA
UNIVERSIDADE D
COIMBRA

Sandro Miguel Ribeiro Saltão

Optimization of the vertical separation of multiple scatter events in the LZ detector with applications in the sensitivity to the $0\nu\beta\beta$ decay of ^{136}Xe

Tese no âmbito do Mestrado em Física Nuclear e de Partículas orientada pelo Professor Doutor Alexandre Miguel Ferreira Lindote e pelo Professor Doutor Paulo Alexandre Brinca da Costa Braz e apresentada ao departamento de Física da Faculdade de Ciências e Tecnologia da Universidade de Coimbra.

Fevereiro de 2023

Optimization of the vertical separation of multiple scatter events in the LZ detector with applications in the sensitivity to the $\mathbf{0\nu\beta\beta}$ *decay of* $^{\mathbf{136}}\boldsymbol{Xe}$

Abstract

The neutrinoless double beta ($0\nu\beta\beta$) decay is a hypothesized process which, if observed, would show that lepton number violating processes are possible, giving a plausible explanation to the mechanism that lead to a matter dominated Universe, denominated as leptogenesis. It would also lead to a better understanding of the Majorana nature of the neutrino (the neutrino as its own antiparticle) and possibly clarify the neutrino mass hierarchy. The field of research for the $0\nu\beta\beta$ is extremely active, with several running and planned experiments using distinct technologies to the search for this decay.

The LZ experiment is a dual-phase xenon time projection chamber (TPC) designed to search for dark matter in the form of WIMPs. The discovery potential of the LZ experiment does not only fall on the dark matter WIMP search but in a wide range of rare decays and new physics, such is the case of $0\nu\beta\beta$. With a projected 90% CL sensitivity of 1.06×10^{26} years for the half life of $0\nu\beta\beta$ decay in ^{136}Xe (for an experimental live time of 1000 days), it can rival dedicated $0\nu\beta\beta$ experiments. But as in other fields of science, the future of dark matter and rare event searches is being planned now, with the new XLZD Consortium that intends to build a much larger detector based on the work done in LZ, DARWIN and XENONnT.

For $0\nu\beta\beta$, the main background sources are high energy gamma-rays, which have a high probability of interacting multiple times. The importance of the development of a *single scatter/multiple scatter* discrimination tool stands on the fact that the sensitivity of the LZ experiment for high energies can be improved with a better distinction between single scatter and multiple scatter events. This is done to some extent with the data processing and analysis framework of LZ (LZap), but can be improved using dedicated technologies. In this work an algorithm was developed to explore the shape of the electroluminescence signal as a mean to characterize single-site and multi-site interactions and improve the minimum vertical pulse vertex separation.

LZap can natively discriminate pulses down to vertical separations of 4.4 mm for all events near the top of the TPC. The developed algorithm was tested with real data from the LZ detector and demonstrated that it is possible to identify multiple scatter interactions vertically separated down to 2 mm for all drift times of the TPC. It also showed good potential in discriminating pulses with a multiplicity higher than two, surpassing the original objective.

Optimization of the vertical separation of multiple scatter events in the LZ detector with applications in the sensitivity to the $\mathbf{0\nu\beta\beta}$ *decay of* $^{\mathbf{136}}\boldsymbol{Xe}$

Resumo

O decaimento duplo de electrões sem emissão de neutrinos ($0\nu\beta\beta$) é um processo teorizado que, se observado, mostrará que processos que violem a concervação do número leptónico poderão existir, podendo explicar o mecanismo que conduziu o Universo a ser dominado por matéria, denominado por leptogenesis. Poderá também explicar a natureza Majorana do neutrino (sendo a sua própria antipartícula) e possívelmente clarificar a hierarquia de massas dos neutrinos. A área de pesquisa do $0\nu\beta\beta$ é extremamente ativo, com diversas experiências em funcionamento e a serem planeadas usando diversas tecnologias para procurar este decaímento.

A experiência LZ consiste numa câmara de projeção temporal (TPC) de duas fases de Xenon projetada para a descoberta the matéria escura na forma the WIMPs. O potencial de descoberta da experiência de LZ não está só limitado à procura de WIMPs mas, também a outros decaimentos raros e física nova, como é o caso do $0\nu\beta\beta$. Com uma sensibilidade para o tempo de meia vida para o decaimento $0\nu\beta\beta$ do ^{136}Xe de 1.06×10^{26} anos (para 1000 dias de aquisição de dados) assumindo um intervalo de confiança de 90%, consegue rivalizar com experiências puramente dedicadas a $0\nu\beta\beta$. De forma semelhante a outras área de ciência, o futuro está a ser planeado agora, como é o caso do Consórcio XLZD que pretende construir um detector de grande dimensões baseado no trabalho realizado em LZ, DARWIN e XENONnT.

Para o decaimento $0\nu\beta\beta$, a principal fonte de fundos são raios-gama de alta energia, que têm uma elevada probabilidade de interagirem multiplas vezes. A importância do desenvolvimento de ferramentas de discriminação entre eventos simples ou multiplos é justificada pelo facto de a sensibilidade da experiência de LZ para altas energias poder ser melhorada com uma melhor distinção entre eventos de simples ou múltiplos. Isto é conseguido pela framework de processamento de dados de LZ (LZap), mas pode ser melhorada usando técnicas dedicadas. Neste trabalho um algoritmo foi desenvolvido para explorar o perfil do sinal de eletroluminescência,

de forma a caracterizar melhor a topologia dos eventos e melhorar a separação vertical miníma entre pulsos.

LZap pode discriminar nativamente pulsos até uma separação vertical mínima de 4.4 mm para eventos no topo da TPC. O algoritmo desenvolvido foi testado com dados reais adquiridos pela experiência LZ e demonstrou que é possível identificar pulsos com interações verticais múltiplas até a um mínimo de 2 mm para todos os tempo de deriva da TPC. Além disso, também mostrou potencial para discriminar pulsos com multiplicidades superiores a dois, ultrapassando o objetivo inicial.

Acknowledgements

This thesis is dedicated to my grandparents and parents as they carried me along my life with their love, care and belief in me. A heart full thanks also goes to my dear Joana, which has been my corner stone and greatest teammate for years. This work is as much mine, as is theirs.

I would like to present my special thanks to my supervisors Alexandre Lindote and Paulo Braz for their guidance, knowledge and endless patience over the path taken during the development of the work for this thesis project.

I would like to thank the University of Coimbra and the Laboratório de Instrumentação e Física Experimental de Partículas (LIP) for hosting this work. A special thanks to the LIP Dark Matter Group for making me feel welcome since the first day and for the help and time given to me.

I also would like to extend my gratitude to the LZ community and Dr. Fabian Kuger of XLZD Consortium for their inputs and constructive discussions about my work.

Cofinanciado por:

Contents

Symbols and Abbreviations

AF	Analysis Framework
BG	Background
CSD	Calibration Source Deployment
DER	Detector Electronics Response
DM	Dark Matter
ER	Electron Recoil
GdLS	Gadolinium-loaded Liquid Scintillator
GR	General Relativity
ICV	Inner Cryostat Vessel
LS	Liquid Scintillator
LUX	Large Underground Xenon
LXe	Liquid Xenon
LZ	LUX-ZEPLIN
LZap	LZ Analysis Programme
MDC	Mock Data Challenge
NEST	Noble Element Simulation Technique
NR	Nuclear Recoil
OCV	Outer Cryostat Vessel
PHE	Photoelectron

PHD	Photons detected
PMT	Photomultiplier Tube
PTFE	Polytetrafluoroethylene
RQ	Reduced Quantity
SM	Standard Model
SURF	Sanford Underground Research Facility
TPC	Time Projection Chamber
VUV	Vacuum-Ultraviolet
WIMP	Weakly Interactive Massive Particle

Chapter 1

Overview

The LUX-ZEPLIN (LZ) experiment is dual-phase xenon time projection chamber (TPC) with 7 tonnes of active target mass, dedicated to rare event searches, such as WIMP dark matter or neutrinoless double beta decay ($0\nu\beta\beta$). This work is focused on improving the vertical position discrimination of multi-site interactions as a way of improving the sensibility to the $0\nu\beta\beta$ decay on ^{136}Xe, for which the LZ experiment has a projected sensitivity of 1.06×10^{26} years. Because of the rare event search focus, the inner region of the LZ detector is an incredible quiet laboratory due to the deep underground location of the detector in order to reduce the muon flux from the upper atmosphere, physical shielding, background veto systems and the self-shielding nature of liquid xenon (LXe).

The $0\nu\beta\beta$ decay is characterized by a mono-energetic peak, as all of the energy is shared by the two electrons emitted. The $0\nu\beta\beta$ decay is a hypothesized lepton number violating (LNV) process. If observed, it can shed light on the Majorana nature of the neutrino as its own antiparticle and could provide some insights on the mechanisms that generated the baryon-antibaryon asymmetry observed in the Universe today, most notably leptogenesis. This decay may also provide good estimates for the value of the effective Majorana neutrino mass, since it is deeply tied to the $0\nu\beta\beta$ decay rate.

The sensitivity of the $0\nu\beta\beta$ decay is dependent on the minimal vertical vertex separation of multi-site interaction in the TPC, which is projected to be 3 mm for LZ. The data processing and analysis framework of LZ (LZap), which is mostly tuned for WIMP search, does not achieve this level of vertical separation (as per design) when analysing high energy events. This results on the possibility of multiple scatter (MS) events being classified as single scatter (SS) at this vertex separation scale. To increase the sensitivity for the $0\nu\beta\beta$ decay, it was necessary to develop a dedicated tool to discriminate between SS and MS events in this regime.

The algorithm developed in this work uses non-linear least squares regression methods, in order to ascertain the topology of the event based on two prior topology assumptions: either a single scatter or a double scatter high-energy event. Two regressions models are used assuming both classifications (SS or MS) and analysed using two different metrics. To develop and fine tune the algorithm, several sets of generated data from a simple S2 pulse generator were used. From this data, it was possible to explore both algorithm and metric capabilities with promising preliminary results. The algorithm also explored SS classified pulses from the first *Science Run* (SR1) data of LZ. From this data it was determined that the algorithm could out-perform LZap by reaching a minimal vertical vertex separation of 2 mm for all drift times and less than 1.5 mm for low drift time events, reaching the limit from which the signal loss starts to negatively impact the sensitivity of the $0\nu\beta\beta$ decay. The algorithm also surpassed the initial expectations by being able to identify events with multiplicity higher than two. The flexibility shown by the algorithm at analysing different sets of data, gives promising prospects of its usages in different experiments besides LZ, such as is the case of the third generation dark matter detector being designed by the XLZD Consortium.

To understand the neutrinoless double beta ($0\nu\beta\beta$) decay, it is fundamental to first understand all the knowledge that lead to it. So, an overview on the neutrino physics and on some evidences that may indicate that LNV processes may be possible are done in Chapter 2, where a brief review on the different experimental techniques on the research of the $0\nu\beta\beta$ decay can also be found. On Chapter 3, the LUX-ZEPLIN (LZ) experiment is presented, and the detector and the physics behind xenon detectors are described. On Chapter 4 the framework used on the LZ experiment (LZap) is deconstructed into its parts and the tool used to tune the developed algorithm and the algorithm itself are explained. On Chapter 5 the results given by the algorithm, both for simulated and real data, are presented and discussed. And finally, on Chapter 6 the conclusions of the work done and some future prospects are discussed.

Chapter 2

Neutrino Physics and Experimental Techniques

2.1 Beta Decay and the Neutrino Hypothesis

The β-decay is a type of nuclear decay, of which three modes exist, the β^- (see Figure 2.1), β^+-decay and electron capture, corresponding to a electron and positron emission and a electron capture from the nucleus, respectively. This single β emission would give rise to a discrete energy spectrum, which is not consistent with the continuous spectrum observed as Figure 2.2. The existence of an additional neutral particle was first theorized by Pauli to explain the continuous nature of β-decay spectrum, as being the case, both leptonic particles would share the kinetic energy corresponding to the Q-value of the reaction. This explains how the β-decay conserves momentum, energy and spin. This new particle is known as the neutrino, and being a lepton it interacts via the weak force. Now, the three modes previously mentioned become, $n \rightarrow p + e^- + \bar{\nu}$ (for β^-) and $p \rightarrow n + e^+ + \nu$ (for β^+) and $e^- + p \rightarrow n + \nu$ (for the electron capture) [Kra88].

2.2 Neutrinos

2.2.1 Discovery of Neutrino Flavours

In 1936, Hans Bethe, using Fermi's theory, postulated a process by which a neutrino would be detected by direct observation, resorting to the inverse β-decay, described by the process $p + \nu \rightarrow n + e^+$. However, the estimated cross section is of the order $10^{-44} cm^2$ for a 1 MeV neutrino [GK07], a value which seemed too low for a feasible experimental detection at the time.

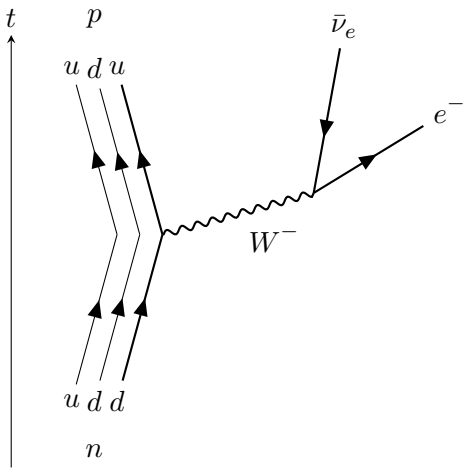

Figure 2.1: Feynman diagram for the single β^- decay. The u and d represent the up and down quarks, beginning with a udd configuration correspondent of a neutron, n and transforming into a udu configuration correspondent of a proton, p. W^- represent the mediator boson for the weak force, e^- the electron and $\overline{\nu}_e$ the electron anti neutrino.

It took almost 20 years to devise an experiment capable of such measurement. This advance, done by Clyde Cowan and Frederick Reines, consisted on both having access to a large flux of neutrinos, which consisted on the use of a nuclear reactor with a neutrino flux of $5 \times 10^{13} s^{-1} cm^{-2}$ and a large amount of detector target material (1400 litres of Cadmium-doped liquid scintillator layered in between water targets and observed by light sensors) to overcome the low cross section [Gri08]. The choice of water as the target was due to the fact that it is a proton rich environment where the detection process is favoured. The positron is annihilated, producing back-to-back 511 keV γ-rays and the neutrons are absorbed by the Cadmium (which has a large cross section for low energy neutron capture), producing a metastable nucleus that emits a photon when goes to the ground state. The Cd neutron absorption is given by

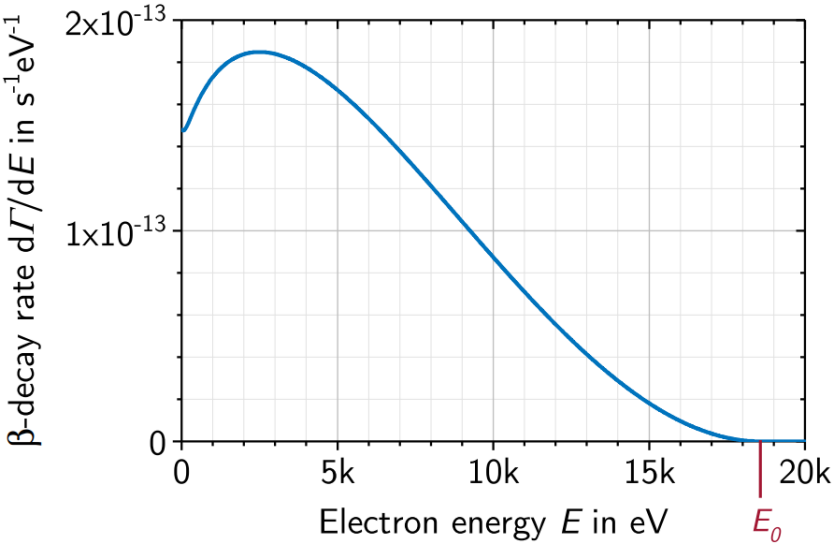

Figure 2.2: Energy spectrum of electrons emitted during β decay in Tritium. Image from [K+19]

$$n + {}^{108}Cd \rightarrow {}^{109m}Cd \rightarrow {}^{109}Cd + \gamma \tag{2.1}$$

where an exited state of ^{109m}Cd is generated and then subsequently emits a 8 MeV γ [RC53]. Together these two photon channels produce the signature of the inverse β-decay, which are then detected by light sensors (photo-multipliers tubes or PMTs) .

In 1962, Lederman, Schwartz and Steinberger demonstrated that more than one type of neutrino flavour existed, the muon and tau neutrinos. A beam of energetic protons striking a Beryllium target was used to produce a shower of positive pions (π^+), which were guided toward a steel wall letting the neutrinos and a very small number or muons pass by to the spark chamber. In the spark chamber, the relevant processes were at the time

$$\nu_e + n \rightarrow p + e^- \tag{2.2}$$

$$\nu_\mu + n \rightarrow p + \mu^- \tag{2.3}$$

where ν_e and ν_μ represent the electron an muon neutrinos respectively, n the neutron, p the proton, e^- the electron and μ^- the muon. Both e^- and μ^- generate distinct tracks that can be discriminated based on their topology. To consider an event as a valid candidate, the produced track must be contained within the fiducial volume of the chamber. If we assume that ν_e is the same as ν_μ, then the rate of electron and muon production must be the same, contradicting the observations, where only 6 electron showers of 29 predicted occur, proving the existence of ν_μ [D$^+$62]. In 2001, the DONUT Collaboration found evidence of the tau neutrino (ν_τ), resorting to the visualization of the "kink" angle of the tau decay [Pat01].

Today 3 different neutrinos flavours are known, corresponding to the three flavours of leptons: electron, muon and tau. The Gargamelle Collaboration at CERN found evidence for neutral currents involved in neutrino interactions, confirming the unification of electromagnetic and weak forces [DLL19]. Later, the UA1 and UA2 experiments, also at CERN, discovered the Z and $W^\pm$ bosons which mediate the weak interactions [DLR15].

2.3 Neutrino Flavour Oscillations

2.3.1 Oscillation Evidences

The energy output of the Sun is due to the fusion of Hydrogen present in the core of the star into heavier elements. These process consists on the pp chain and CNO cycle [Gri08], which obey the baryon, lepton, electric charge and energy conservation laws. Because of this, one can know that the flux of neutrinos is constant and is given by the sum of all processes which have the emission of an electron neutrino in their final products. The pp chain starts with two processes [Gri08]:

$$p + p \rightarrow D + e^{+} + \nu_e \tag{2.4}$$

and

$$p + e^{-} + p \rightarrow D + \nu_e \tag{2.5}$$

which have a probability of 99.76% and 0.24%, respectively. Then follows

$$D + p \rightarrow {}^{3}He + \gamma \tag{2.6}$$

From the production of ${}^{3}He$, three branches emerge. The first (p-p I) is given by

$${}^{3}He + {}^{3}He \rightarrow {}^{4}He + p + p \tag{2.7}$$

, which has a probability of 84.6%. With 15.4% a second reaction given by

$${}^{3}He + {}^{4}He \rightarrow {}^{7}Be + \gamma \tag{2.8}$$

that branches out into two the second (p-p II) and third (p-p III) branches, with a probability of 99.89% and 0.11%, respectively. The p-p II is given by

$${}^{7}Be + e^{+} \rightarrow {}^{7}Li + \nu_e \tag{2.9}$$

followed by

$${}^{7}Li + p \rightarrow {}^{4}He + {}^{4}He \tag{2.10}$$

Finally, the p-p III is given by

$${}^{7}Be + p \rightarrow {}^{8}B + \gamma \tag{2.11}$$

followed by

$${}^{8}B \rightarrow {}^{8}Be + e^{+} + \nu_e \tag{2.12}$$

The Sun, being a type-G star, has only two significant Carbon-Nitrogen-Oxigen (CNO) cycles, I and II. The naming of "cycle" means that reaction happens in a loop feeding itself. The CNO-I cycle is given by

$${}^{12}_{6}C + p \rightarrow {}^{13}_{7}N + \gamma \tag{2.13}$$

$${}^{13}_{7}N \rightarrow {}^{13}_{6}C + e^{+} + \bar{\nu_e} \tag{2.14}$$

$${}^{13}_{6} + p \rightarrow {}^{14}_{7}N + \gamma \tag{2.15}$$

$${}^{14}_{7}N + p \rightarrow {}^{15}_{8}O + \gamma \tag{2.16}$$

$${}^{15}_{8}O \rightarrow {}^{15}_{7}N + e^{+} + \bar{\nu_e} \tag{2.17}$$

$${}^{15}_{7}N + p \rightarrow {}^{12}_{6}C + \alpha \tag{2.18}$$

The CNO-II cycle is a minor branch with a probability of only 0.04%, where ${}^{15}_{7}N$ does not produce ${}^{12}_{6}C$ and an α-particle and alternatively keeps fusing, generating new nuclei. This is

given by

$$^{15}_{7}N + p \rightarrow ^{16}_{8}O + \gamma \tag{2.19}$$

$$^{16}_{8}O + p \rightarrow ^{17}_{9}F + \gamma \tag{2.20}$$

$$^{17}_{9}F \rightarrow ^{17}_{8}O + e^{+} + \bar{\nu}_e \tag{2.21}$$

$$^{17}_{8}O + p \rightarrow ^{14}_{7}N + \alpha \tag{2.22}$$

From this point on, the CNO-II and CNO-I cycles merge, closing the loop. These two cycles can be analogously seen as an electric circuit with two different valued resistances mounted parallel to each other, with one common power source. The multiple processes described here generate a neutrino flux which the theorized values are shown in Figure 2.3.

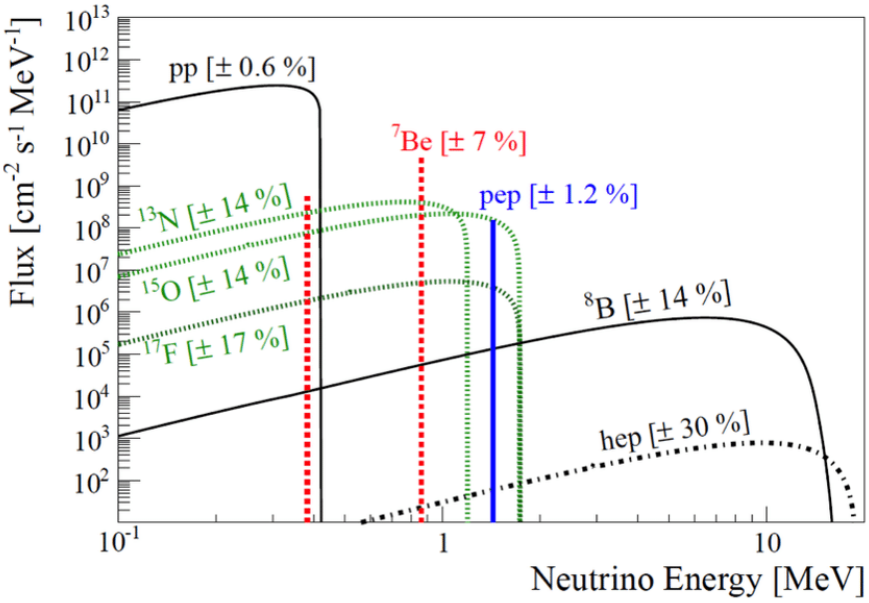

Figure 2.3: Solar neutrino flux from multiple nuclear reactions as a function of the neutrino energy. Image from [D^{+}14].

Although an exact model does not exist, in a good approximation, they are independent of the condition variances of the Sun. Their relative contributions are estimated using standard solar models, which take into account the chemical composition, temperature and density distribution in the Sun's core.

The Ray Davis and John D. Bahcall's Homestake Experiment had the purpose of measuring the neutrino flux from the Sun and consisted on 615 tons of tetrachloroethylene on a tank at a depth of 1480 meters, located at the Homestake gold mine in Lead, South Dakota, USA. The detection mechanism is

$$^{37}Cl + \nu_e \rightarrow ^{37}Ar + e^{-} \tag{2.23}$$

with a threshold energy of 814 keV [DS98]. The ^{37}Ar was then gassed out every couple of weeks by bubbling helium through the tank, and then measuring its β decay rate with a proportional counter, the neutrino capture rate could be inferred. The solar neutrino flux measured by the

Homestake Experiment, between 1970 and 1994, revealed a discrepancy with the theoretical value from the Standard Solar Model (SSM), resulting in only a third of the expected flux being detected [C$^+$98], seen as first evidence for the flavour neutrino changes, also known as neutrino oscillations.

If the electron neutrinos (ν_e) were shown to oscillate, the hypothesis was extended for other neutrino flavours, such as muon neutrinos (ν_μ). These neutrinos are produced by cosmic rays which are constantly bombarding the Earth's atmosphere, being mainly composed of protons, α particles and, more rarely, heavier nuclei. These particles have a very large continuous energy spectrum up to 10^{20} eV and the flux decreases very rapidly as the energy increases. As these cosmic rays enter Earth's atmosphere, they interact with nuclei present in upper atmosphere producing pions, and less frequently, K mesons. Because these products are not stable, they decay into less energetic configurations [KN12]

$$\pi^+ \rightarrow \mu^+ + \nu_\mu \tag{2.24}$$

$$\pi^- \rightarrow \mu^- + \overline{\nu}_\mu \tag{2.25}$$

The muons further decay via

$$\mu^+ \rightarrow e^+ + \nu_e + \overline{\nu}_\mu \tag{2.26}$$

$$\mu^- \rightarrow e^- + \overline{\nu}_e + \nu_\mu \tag{2.27}$$

The production rate of $\bar{\nu_\mu}$ and ν_μ should be approximately the same because the decay chains both produce the muon neutrino and its antiparticle, so any difference in the decay rate is cancelled out. That is no the case for the $\bar{\nu_e}$ and ν_e as they are unique for each decay chain, and therefore their production rate is directly related with the flux of π^+ or π^-. To prevent dependency on the $\pi^\pm$ flux, the sum of the neutrino and antineutrino of each flavour must be used. These make the majority of the processes by which atmospheric neutrinos are created, and so one can see that the fluxes of all neutrinos and their antiparticles counterparts are strictly related as

$$2\Phi(\overline{\nu}_e + \nu_e) \simeq \Phi(\overline{\nu}_\mu + \nu_\mu) \tag{2.28}$$

where Φ represents the neutrino flux. For energies ranges higher than a few GeV, a fraction of muons do not decay before reaching the surface, meaning that the flux rate between the two flavours does not hold the 2 factor as seen in Figure 2.4. However, we can calculate with accuracy the fraction that does decay and correct this effect.

The Super-Kamiokande experiment is a 50 kiloton ultrapure water tank designed to detect Cherenkov radiation. The mechanism to detected neutrinos is given by the interaction mostly between incoming electron or muon neutrino with an atom producing either a electron or a positron that move faster than the speed of light in that medium [F$^+$98].

From both decay chains previously mentioned for the pions, we can also reason that

$$\Phi(\overline{\nu}_\mu) \simeq \Phi(\nu_\mu) \tag{2.29}$$

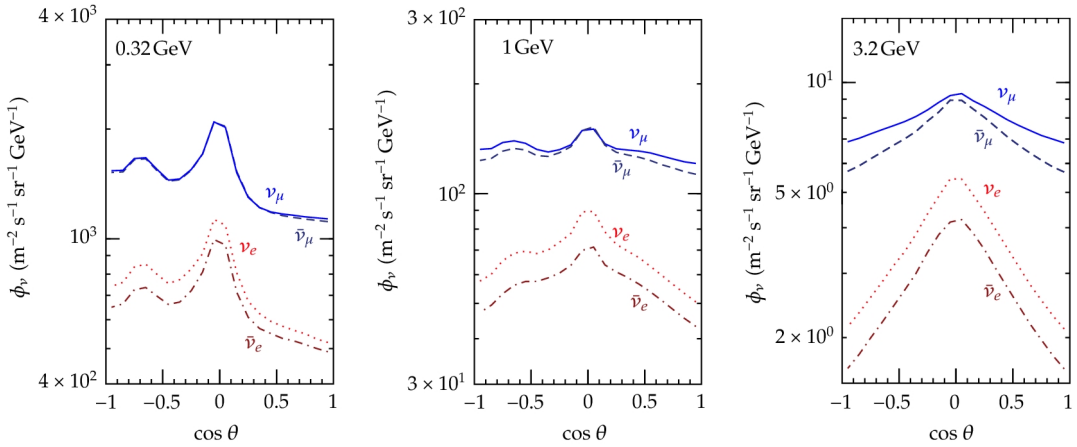

Figure 2.4: Zenith angle dependency on fluxes of atmospheric $\bar{\nu_\mu}$, ν_μ, $\bar{\nu_e}$ and ν_e for different energy ranges at Kamioka Observatory. The asymmetry seen for low energies is due to the geomagnetic field which acts as a cutoff for the cosmic rays. This effect disappears for higher energies meaning that the flux are up and down symmetric. Images from [KN12].

and that

$$\frac{\Phi(\nu_e)}{\Phi(\overline{\nu}_e)} \simeq \frac{\Phi(\pi^+)}{\Phi(\pi^-)} \tag{2.30}$$

The latter can be estimated precisely by measuring the μ^+ and μ^- flux ratio. So the ν_e, $\overline{\nu}_e$, ν_μ, $\overline{\nu}_\mu$ fluxes are known. Within the energy ranges of 0.1 and 10 GeV, the ratio between the muon and electron neutrino is known with an uncertainty of only 5%.

The Super-Kamiokande experiment results showed an agreement with the Monte Carlo simulations assuming the oscillation hypothesis, as is showed on the right hand side of Figure 2.5. This result has an estimated probability of being caused by a statistical fluctuation of less than 0.001% and 1%, for energy scales of sub- and multi-GeV, respectively [F$^+$98]. As the measured ν_e flux has no significant deviation from the expected flux (see left hand side of Figure 2.5), the deficit on the ν_μ flux is in good agreement with the $\nu_\mu \to \nu_\tau$ flavour oscillation scenario [F$^+$98].

SNO wielded similar results [Bah01] to the experiments previously discussed and expanded on it. The SNO experiment was capable of having sensitivity to all neutrino flavours since it could detect ^8B solar neutrinos through multiple reactions: the Neutral Current (NC), elastic scattering (ES) and Charged Current (CC), which are given by [A$^+$02]

$$\nu_x + D \to p + n + \nu_x(NC) \tag{2.31}$$

$$\nu_x + e^- \to \nu_x + e^-(ES) \tag{2.32}$$

$$\nu_e + D \to p + p + e^-(CC) \tag{2.33}$$

where D represents a deuterium atom. The NC and ES reactions are sensitive to all three neutrino flavours, while the CC reaction is only sensitive to the electron neutrino. The measured fluxes are for the three currents are shown in Figure 2.6.

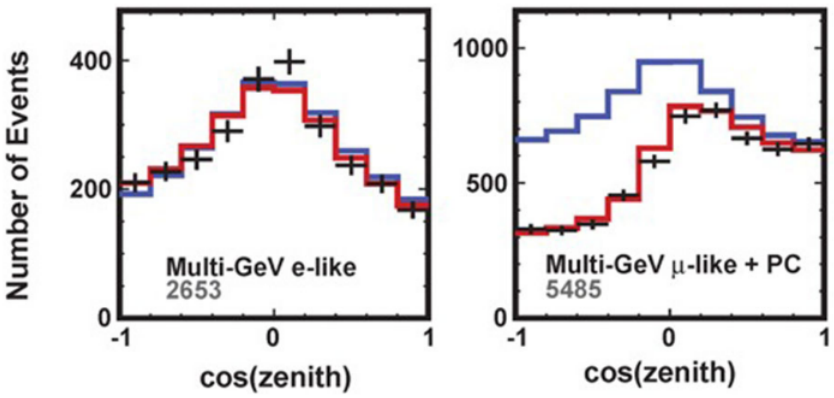

Figure 2.5: Results from the Super Kamiokande experiment, where it is represented the number of events expected for the the non existence (blue line) and existence (red line) of oscillations in muon neutrinos produced in the atmosphere, as a function of the zenith angle. The black points with the correspondent error bars are the experimental results, which are consistent with neutrino oscillations. [Kaj16]

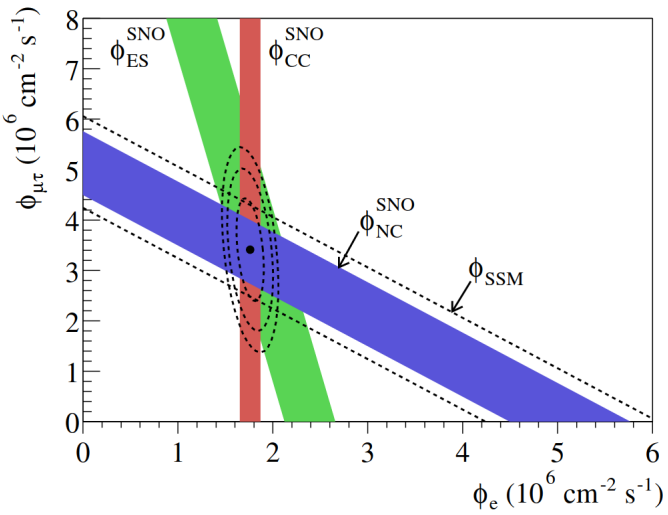

Figure 2.6: Flux of ^8B solar μ and τ neutrinos ($\Phi_{\mu\tau}$) as function of the electron neutrino flux (Φ_e). The diagonal band, delimited by the dashed line, represents the total ^8B flux as predicted by the Standard Solar Model and the solid blue band is the measured in SNO by the Neutral Current. The red and green bands represent the elastic scattering reaction and Charged Current (CC) reactions, respectively. The fluxes are consistent with neutrino flavour oscillation since they intersect at the fit values for $\Phi_{\mu\tau}$ and Φ_e. [A$^+$02]

2.3.2 Mass Induced Neutrino Flavour Oscillation

The charged leptons with flavours $l = e$, μ and τ have an associated neutrino ν_l of the same flavour and each flavour corresponds to a different leptonic number that is independently conserved. If neutrinos have mass and leptons behave similarly to quarks, then each flavour is a superposition of mass eigenstates, related to the flavour eigenstates by [GK07]

$$|\nu_l\rangle = \sum_m^3 U_{lm}^* |\nu_m\rangle \tag{2.34}$$

where the ν_m are the mass eigenstates with $m = 1$, 2 and 3, and U_{lm} is the Neutrino Mixing Matrix, also known as the Pontecorvo-Maki-Nakagawa-Sakata (PMNS) Matrix. Explicitly, Equation (2.34) becomes [GLZ18]:

$$\begin{bmatrix} \nu_e \\ \nu_\mu \\ \nu_\tau \end{bmatrix} = \begin{bmatrix} U_{e1} & U_{e2} & U_{e3} \\ U_{\mu 1} & U_{\mu 2} & U_{\mu 3} \\ U_{\tau 1} & U_{\tau 2} & U_{\tau 3} \end{bmatrix} \begin{bmatrix} \nu_1 \\ \nu_2 \\ \nu_3 \end{bmatrix} \tag{2.35}$$

The unitary nature of the PMNS matrix is only preserved if both mass and flavour states contribute for the mixing. If this condition is satisfied then, for Dirac neutrinos, the PMNS matrix can be expressed by three rotation angles (θ_{ij} with i, j =1, 2, 3) and one single complex charge-parity (CP) violating phase (δ_{CP}), taking the form [GLZ18]

$$\begin{aligned} U &= \begin{bmatrix} 1 & 0 & 0 \\ 0 & c_{23} & s_{23} \\ 0 & -s_{23} & c_{23} \end{bmatrix} \begin{bmatrix} c_{13} & 0 & s_{13}e^{-i\delta_{CP}} \\ 0 & 1 & 0 \\ -s_{13}e^{i\delta_{CP}} & 0 & c_{13} \end{bmatrix} \begin{bmatrix} c_{12} & s_{12} & 0 \\ -s_{12} & c_{12} & 0 \\ 0 & 0 & 1 \end{bmatrix} \\ &= \begin{bmatrix} c_{12}c_{13} & s_{12}c_{13} & s_{13}e^{-i\delta_{CP}} \\ -s_{12}c_{23} - c_{12}s_{23}s_{13}e^{i\delta_{CP}} & c_{12}c_{23} - s_{12}s_{23}s_{13}e^{i\delta_{CP}} & s_{23}c_{13} \\ s_{12}s_{23} - c_{12}c_{23}s_{13}e^{i\delta_{CP}} & -c_{12}s_{23} - s_{12}c_{23}s_{13}e^{i\delta_{CP}} & c_{23}c_{13} \end{bmatrix} \end{aligned} \tag{2.36}$$

where c_{ij} and s_{ij} are $\cos\theta_{ij}$ and $\sin\theta_{ij}$, respectively.

Considering that neutrinos behave as free particles, the mass eigenstates evolve in time as plane waves. In the Heisenberg picture we have the time evolution of a state given by [GK07, GLZ18]

$$|\nu_i(t)\rangle = e^{-iE_i t} |\nu_i(0)\rangle \tag{2.37}$$

where $E_i = \sqrt{\mathbf{p}^2 + m_i^2}$ is the energy of the mass eigenstate of ν_i with mass m_i. The time evolution of the flavour state (α) is then given by

$$|\nu_\alpha(t)\rangle = \sum_i U_{\alpha i}^* e^{-iE_i t} |\nu_i\rangle \tag{2.38}$$

Assuming the unitary nature of the PMNS matrix ($U^\dagger U = \mathbb{1}$) the mass eigenstates can be expressed in terms of flavours eigenstates inverting (Equation 2.34), becoming

$$|\nu_i\rangle = \sum_\alpha U_{\alpha i} |\nu_\alpha\rangle . \tag{2.39}$$

From Equations (2.38) and (2.39), we obtain

$$|\nu_\alpha(t)\rangle = \sum_{\beta=e,\mu,\tau} \left(\sum_{k=1,2,3} U^*_{\alpha k} e^{-iE_i t} U_{\beta k} \right) |\nu_\beta\rangle . \tag{2.40}$$

This tell us that for $t > 0$ the neutrino state $|\nu_\alpha(t)\rangle$, which is a pure flavour state at $t = 0$, becomes a superposition of the three different flavour eigenstates. This behavior is due to the non diagonal structure of the mixing matrix U, otherwise each flavour eigenstate would correspond to a specific mass eigenstate.

From this result we can calculate the time dependent probability of the transition $|\nu_\alpha\rangle \to |\nu_\beta\rangle$ [GLZ18]

$$\begin{aligned} P_{\nu_\alpha \to \nu_\beta} &= \left| \langle \nu_\beta | \nu_\alpha(t) \rangle \right|^2 = \left| \sum_k U^*_{\alpha k} U_{\beta k} e^{-iE_k t} \right|^2 \\ &= \sum_{k,j} U^*_{\alpha k} U_{\beta k} U_{\alpha j} U^*_{\beta j} e^{-(E_k - E_j)t}. \end{aligned} \tag{2.41}$$

The Energy-momentum relation for ultra-relativistic (UR) neutrinos can be approximated by [GK07]

$$E_k \simeq E + \frac{m_k^2}{2E} \tag{2.42}$$

and for the case of two states we get the relation between the energies and the squared masses differences ($\Delta m^2_{kj} = m^2_k - m^2_j$)

$$E_k - E_j \simeq E + \frac{\Delta m^2_{kj}}{2E} \tag{2.43}$$

Also, since we are in the UR regime ($m_0^2 \ll \vec{p}^{\,2}$), $E = |\vec{p}|$ and we can approximate time to the distance L, which is a more convenient way of expressing $P_{|\nu_\alpha\rangle \to |\nu_\beta\rangle}$. Therefore, the transition probability in Equation 2.41 becomes [GK07]

$$P_{\nu_\alpha \to \nu_\beta}(E, L) = \sum_{k,j} U^*_{\alpha k} U_{\beta k} U_{\alpha j} U^*_{\beta j} \exp\left(-i \frac{\Delta m^2_{kj}}{2E} L \right) \tag{2.44}$$

Imposing a non-degenerate behaviour on the mass eigenstates, the wave function of these will propagate differently and the neutrino flavour will oscillate between flavour eigenstates as it propagates.

So far, only the *transition probabilities* were obtained, where $\alpha \neq \beta$. For the case of $\alpha = \beta$

which it is called *survival probabilities* the quadric products of the PMNS matrix on Equation 2.41 became real and equal to [GK07]

$$|U_{\alpha k}|^2 |U_{\beta k}|^2 \tag{2.45}$$

thus resulting in a survival probability given by

$$P_{\nu_\alpha \to \nu_\beta}(E, L) = 1 - 4 \sum_{k>j} |U_{\alpha k}|^2 |U_{\beta k}|^2 \sin^2 \left(\frac{\Delta m^2_{kj}}{4E} L \right) \tag{2.46}$$

The parameters that describe the neutrino oscillations transitions are the elements of the PMNS matrix, which gives the mixing amplitudes between flavour and mass eigenstates, and the squared-mass differences. Of these squared-mass two are independent ($\Delta m^2_{31} = \Delta m^2_{21} + \Delta m^2_{23}$, with $\Delta m^2_{ij} = m^2_i - m^2_j$), meaning that only Δm^2_{21} and Δm^2_{23} need to be experimentally determined. The Solar neutrino oscillations are more sensitive to the Δm^2_{21} and θ_{21} parameter, while atmospheric neutrino oscillations have greater sensitivity to the Δm^2_{23} and θ_{23} parameters, because these are the dominant transitions happening for each case. Because of this Δm^2_{21} and Δm^2_{23} are known as Solar and Atmospheric mass difference, respectively. For the mass difference Δm^2_{31}, nuclear neutrino experiments are used, as the main oscillation channel is the mass eigenstates $1 \leftrightarrow 3$, therefore complementing other measurements [QV15].

The data from Solar neutrino oscillations yields that Δm^2_{21} is positive, meaning that $m_1 < m_2$ in the case that m_1 is the mass eigenstate with the biggest contribution for the electron neutrino. One important consideration to take into account is the varying density of the Sun, also known as the Mikheyev-Smirnov-Wolfenstein (MSW) effect, where the neutrino flavour oscillations are enhanced due to interactions between the propagating neutrinos and the electron cloud of the atoms of the solar medium. Thus the propagation behavior of neutrino oscillations is different whether it propagates through a vacuum or through matter and the oscillations depend on the signal of Δm^2_{21} [Smi03].

For atmospheric neutrino oscillations, the distance neutrinos travel through Earth is not enough to determine the signal of both Δm^2_{23} and Δm^2_{31}, which must have similar magnitudes due to the fact that $\Delta m^2_{21} \ll |\Delta m^2_{31}|$. Because of this uncertainty, two hierarchies arise (as seen in Figure 2.7): the *normal* and the *inverted hierarchy*. In the scenario where $\Delta m^2_{31} > 0$ (*"normal hierarchy"*) we have $m_1 < m_2 < m_3$. By opposition if $\Delta m^2_{31} < 0$ (*"inverted hierarchy"*) ν_3 becomes the mass eigenstate with the lowest mass, and we have $m_3 < m_1 < m_2$. For θ_{12}, θ_{13}, Δm^2_{21} and $|\Delta m^2_{31}|$ the agreement between different experimental results are good, however for the mixing angle θ_{23} and the leptonic CP phase δ_{CP} the uncertainties are currently large.

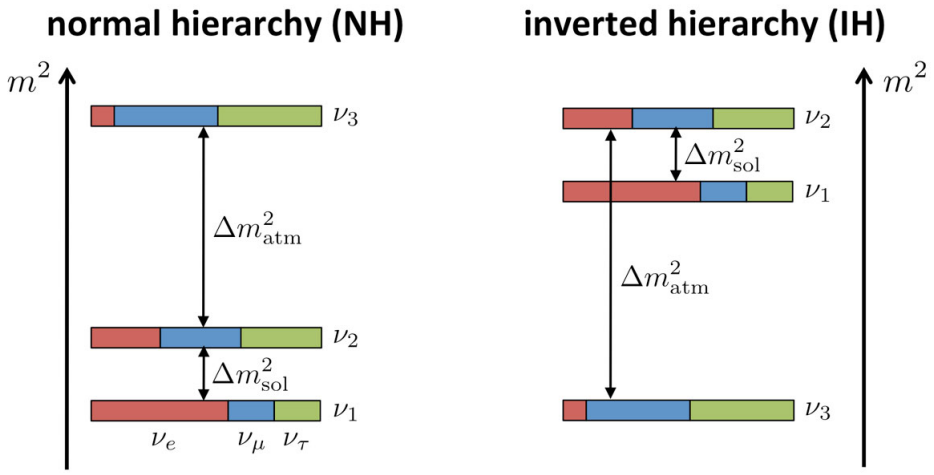

Figure 2.7: Simple representation of the two neutrino mass hierarchies. Image from [Vag19].

2.4 Leptogenesis

From cosmological observations there is the indication that the number of baryons is unequal to the number of antibaryons. All the structures of the Universe (planets, stars, galaxies,...) are dominated by matter, with almost no antimatter present. This contradicts the assumption that the Universe originated from a state with the same number of baryons and antibaryons. It is unlike that the initial conditions in the early Universe were very fine tuned to produce the asymmetry observed today, meaning that the present matter-antimatter asymmetry must have been generated dynamically early on (baryogenesis). Also, if the Universe have been expanding since the Big Bang (as Cosmic Microwave Background observations seem to indicate) any baryonic asymmetry would have been diluted away [DNN08].

Despite the very reduced initial asymmetry between baryons and antibaryons created by the Big Bang, it is now quite obvious since the Universe is matter dominated, being defined as η and is given by the following expression [DNN08]

$$\eta \equiv \frac{n_B - n_{\overline{B}}}{n_\gamma} = (6.21 \pm 0.16) \times 10^{-10} \tag{2.47}$$

where n_B, $n_{\overline{B}}$ and n_γ are the number densities of baryons, antibaryons and photons at present time, respectively [DNN08]. Alternatively, the baryon asymmetry can be written by means of entropy density (s) as

$$Y_{\Delta B} \equiv \frac{n_B - n_{\overline{B}}}{s} = (8.75 \pm 0.23) \times 10^{-11} \tag{2.48}$$

being a convenient way of expressing this asymmetry because s is conserved as the Universe expands. The two definitions expressed in Equations 2.47 and 2.48 can be related as [DNN08]

$$Y_{\Delta B} = \frac{n_{\gamma 0}}{s_0}\eta \simeq \frac{\eta}{7.04} \tag{2.49}$$

where the null index represent the values at $t = 0$.

Another way of of expressing this asymmetry is by the ratio (Ω_B) between the baryonic density and the critical energy density which can be related with η by

$$\eta \equiv 2.74 \times 10^{-8} \Omega_B h^2 \tag{2.50}$$

where h is the Hubble parameter.

The baryon asymmetry is inferred by the relative concentration of light elements in the Universe (nucleosynthesis) which are η dependent and the value of Ω_B can be obtained by the measurement of the cosmic microwave background. The consistency between the two measurements, constraint the value of the asymmetry, meaning that its value can be explained if a consistent baryogenesis theory is determined [DNN08].

There are three considerations required for the baryogenesis hypothesis, known as the Sakharov conditions [DNN08]:

1. Baryon number violation, so that the initial state evolve from $Y_{\Delta B} = 0$ to a final state with $Y_{\Delta B} \neq 0$.

2. C and CP violation, so that processes involving baryons don't evolve at the same rate as C- and CP-conjugate processes involving antibaryons.

3. Out of equilibrium dynamics, since in equilibrium there are no asymmetries in quantum numbers that are not conserved.

All three considerations are present in the Standard Model, but as it stands, no known SM mechanism generates a large enough asymmetry.

In the Standard Model, the contribution of the non conservation of the baryon number and the weak interactions which violates C and violates CP via the Kobayashi-Maskawa mechanism do not justify the observed asymmetry. Also, the departure from thermal equilibrium occurs at the electroweak phase transition, but once again the magnitude of this processes is not enough [DNN08].

One possible mechanism to explain the observed baryon asymmetry is the leptogenesis hypothesis, proposed by Fukugita and Yanagida. It consists on the introductions of singlet neutrinos via the seesaw mechanism [FY86]. In this scenario, the CP violation provided by Yukawa couplings is enough of a source to explain η. The lepton number violation comes from Majorana masses (combination of the neutrino mass eigenstates and the neutrino mixing matrix terms [Ben15]) of these new singlet neutrinos. By Standard Model sphaleron (a process static time-independent solution to the electroweak field equations), the partial conversion from lepton asymmetry to baryon asymmetry is assured [KS88], meaning that the dynamically generated lepton asymmetry is converted into a baryon asymmetry due to B+L violation interactions, which occur in the SM [Rio11].

More than explain baryogenesis, leptogenesis provides a strong argument for the Majorana nature of the neutrino, which in turn allows the neutrinoless double beta decay ($0\nu\beta\beta$), as it is a lepton number violating process. Alongside the CP violation observed in neutrino oscillations, searches for $0\nu\beta\beta$ decays offer a good test for the leptogenesis hypothesis.

2.5 The Two Neutrino Double Beta Decay

The Double Beta decay ($2\nu\beta\beta$) is a SM process with four different modes of decay

$$2\nu\beta^-\beta^- : (A, Z) \rightarrow (A, Z+2) + 2e^- + 2\overline{\nu_e} \tag{2.51}$$

$$2\nu\beta^+\beta^+ : (A, Z) \rightarrow (A, Z-2) + 2e^+ + 2\nu_e \tag{2.52}$$

$$2\nu ECEC : 2e^- + (A, Z) \rightarrow (A, Z-2) + 2\nu_e \tag{2.53}$$

$$2\nu EC\beta^+ : e^- + (A, Z) \rightarrow (A, Z-2) + e^+ + 2\nu_e \tag{2.54}$$

where EC stands for electron capture and β^+ and β^- stands for the emission of a positron or an electron, respectively.

For the purpose of this thesis, the first mode is chosen, where two neutrons decay simultaneously into protons via weak interaction (mediated by W^- bosons) emitting two electrons and two electron antineutrinos (see Figure 2.8). This process was first proposed by Goeppert-Mayer in 1935, giving an estimation for the half life time ($T^{2\nu}_{1/2}$) on the order of 10^{17} years, using the Fermi theory of β-disintegration and assuming that the protons and neutrons in the nucleus are represented as two different states of a heavy particle and the electron and neutrino (assumed to be outside the nucleus) are treated using the method of super-quantization [GM35]. The long life time is due to the fact that it is a second-order process of electroweak interaction, meaning that it is highly suppressed. In 1950 the first observation of the $2\nu\beta\beta$ decay was made in the Inghram and Reynolds experiment, which used ^{130}Te obtaining a half life of $\lesssim 1 \times 10^{21}$ years [IR50]. Since then, 12 have been identified to decay via $2\nu\beta\beta$ with half life times on the order of $\sim 10^{19}$ to 10^{24} years [Saa13].

For this decay to occur, the parent nucleus has to be even-even (denoting the parity of the number of protons and of the number of neutrons) and the single beta decay has to be energetically forbidden, meaning that the even-even nucleus is lighter than the odd-odd isobar counterpart (see Figure 2.9). The binding energy of the nucleus is directly related with its mass. The later is described by the semi-empirical mas formula [Kra88]:

$$M(A, Z) = Nm_n + Zm_p - a_V A + a_S A^{2/3} + a_C \frac{Z^2}{A^{1/3}} + a_A \frac{(N-Z)^2}{A} + \delta(A, Z) \tag{2.55}$$

where the first two terms are simply the masses of neutrons and protons present in the nucleus, respectively, the third term is the volume term, which is proportional to the volume, the fourth term is the surface term, the fifth is the Coulomb term which takes into account the repulsion

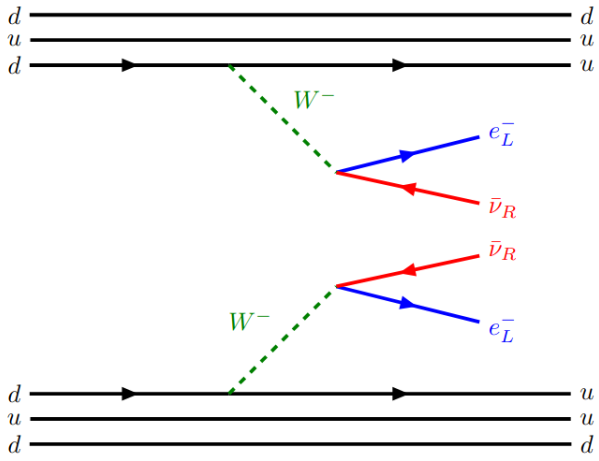

Figure 2.8: Feynman diagram of the first decay mode for the Double Beta Decay. The R and L indexes on the leptons represent the its chirality. The chirality of the electron and the antineutrino was only observed to be left and right, respectively. Image from [D+21].

between the protons, the sixth is the asymmetry term which takes into account the asymmetry between the number of protons and neutrons and finally the last term is the pairing term which captures the effect of spin-coupling. This last term gives the information if the nucleus undergoes a weak decay as it can take negative (even-even), zero(A-odd) or positive (odd-odd) values. Because of this even-even nuclei generally have lower masses than their odd-odd counterparts due to pair binding which lowers the binding state of the nucleus, resulting in an energetically forbidden single beta decay.

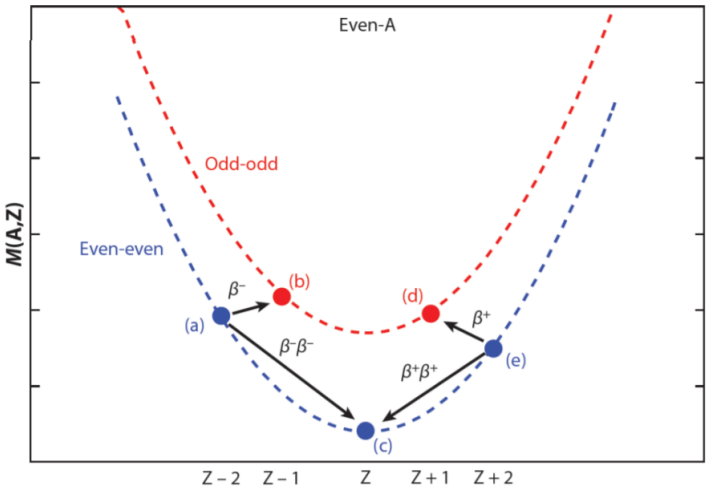

Figure 2.9: Nuclear mass as function of the atomic number Z for a $2\nu\beta\beta$ decay candidate with A even. For the even-even isotope, the $2\nu\beta\beta$ decay is possible when the single beta decay is energetically forbidden.[Saa13]

The energy released is then shared by the leptonic products as the recoil of the nucleus can be

neglected. For the double emission of electrons, the energy released is given as

$$Q_{\beta\beta} = M(A, Z) - M(A, Z + 2) \tag{2.56}$$

and this being the prevalent mode (since the alternative modes have a lower phase space) its therefore the main focus of research.

The importance of the research for $2\nu\beta\beta$ decay fall on the study of the structure of atomic nuclei, where is a fundamental tool to determine the values of nuclear matrix elements (NMEs) which in on themselves can be used to validate or disprove nuclear models. The best case scenario would be the observation of double beta decay in two or more isotopes of the same element, increasing the precision of measurement of the NMEs values .

2.6 The Neutrinoless Double Beta Decay

Similarly as the $2\nu\beta\beta$ process, the $0\nu\beta\beta$ also has 4 modes of decay, being the counterparts of the SM process. They are represented as

$$0\nu\beta^-\beta^- : (A, Z) \rightarrow (A, Z + 2) + 2e^- \tag{2.57}$$

$$0\nu\beta^+\beta^+ : (A, Z) \rightarrow (A, Z - 2) + 2e^+ \tag{2.58}$$

$$0\nu ECEC : 2e^- + (A, Z) \rightarrow (A, Z - 2) \tag{2.59}$$

$$0\nu EC\beta^+ : e^- + (A, Z) \rightarrow (A, Z - 2) + e^+ \tag{2.60}$$

where EC stands for electron capture and β^+ and β^- stands for the emission of a positron or an electron, respectively. As mentioned before, the focus of this thesis is placed on the first mode of decay which is represented in Figure 2.10.

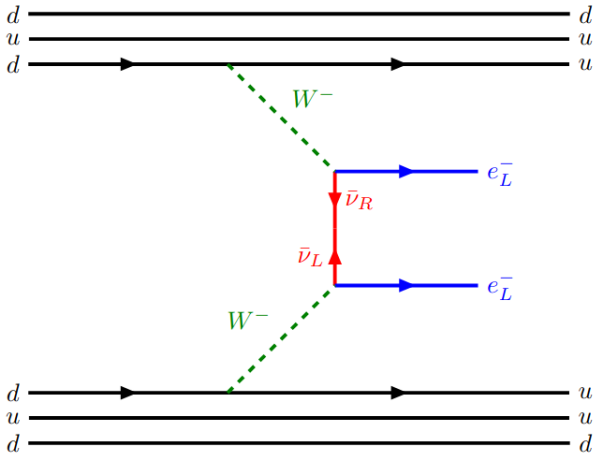

Figure 2.10: Feynman diagram of the first decay mode for the Neutrinoless Double Beta decay under the assumption of a light Majorana neutrino exchange. Image from [D$^+$21].

Provided that neutrinos are Majorana particles (which meas that they are their own antiparticle) and have mass, the simultaneous decay of two neutrons into two protons emitting two electrons and no neutrinos should be possible and is known as Neutrinoless Double Beta Decay ($0\nu\beta\beta$). This is a second-order and a lepton number violating (LNV) process, therefore stands outside of the Standard Model scope. For this reason some new physics must be at play, giving rise to many new theorised mechanisms, the most appealing of them being the light Majorana neutrino exchange model, where the decay is mediated by the exchange of a light massive Majorana neutrino, ν_M [D$^+$16]. Since there are no emission of neutrinos, all the energy released is shared by the electrons (once again the nucleus recoil is neglected). All $2\nu\beta\beta$ decaying isotopes are candidates for $0\nu\beta\beta$ decay, as both decays have the same setup (see Figure 2.9).

The decay rate and subsequently the half life time ($T^{0\nu}_{1/2}$) depends on the "effective Majorana neutrino mass" ($\langle m_{\beta\beta}\rangle$) which is given by [DPR19]

$$\langle m_{\beta\beta}\rangle = \Big|\sum_i m_i U_{ei}^2\Big| \tag{2.61}$$

where m_i represents the three mass eigenstates and U_{ei} is the first row of the PMNS matrix, due to the fact that the two leptonic vertices involve solely the electron flavour. For the neutrinoless double beta decay to occur, the neutrino is required to be a Majorana particle (a particle that is its own antiparticle), so three CP phases (ξ_i) need to be added to the matrix U, these being known as Majorana Phases which cannot be determined as no observable is currently known to be dependent upon them [D$^+$16]. This also restricts the ability of determining the $\langle m_{\beta\beta}\rangle$. The rewritten form of the PMNS matrix is given by $U^D D^M$, where U^D is the original PMNS matrix containing the Dirac phase, and D^M is a diagonal matrix containing all three Majorana Phases, represented by the following expression

$$D^M = \begin{bmatrix} e^{i\xi_1} & & \\ & e^{i\xi_2} & \\ & & e^{i\xi_3} \end{bmatrix} \tag{2.62}$$

Since only the differences between phases are observed, by convention $\xi_1 = 0$. Finally the "effective Majorana mass" can be represented explicitly containing the Majorana Phases as

$$\langle m_{\beta\beta}\rangle = \Big|\sum_i m_i e^{j\xi_i} U_{ei}^2\Big| \tag{2.63}$$

where now U_{ei} is the first row of the $U^D D^M$ matrix.

The decay rate for the neutrinoless double beta decay is given by [D$^+$21]

$$\Gamma^{0\nu} = (T^{0\nu}_{1/2})^{-1} = G^{0\nu}_{(0)} g_A^4 |\mathcal{M}^{0\nu}|^2 \frac{\langle m_{\beta\beta}\rangle^2}{m_e^2} \tag{2.64}$$

where $G^{0\nu}_{(0)}$ is the phase-space factor, g_A is the axial vector coupling, $\mathcal{M}^{0\nu}$ is the Nuclear Matrix Elements (NMEs) for the $0\nu\beta\beta$ process and m_e is the mass of the electron.

2.6.1 Experimental Signature of the $0\nu\beta\beta$ Decay

Similarly to the single beta decay, the $2\nu\beta\beta$ mode presents itself as a continuous spectrum due to the fact the neutrinos also share the energy released in the process. On the other hand, the $0\nu\beta\beta$ has no neutrinos being emitted, and thus the two electrons share almost the entirety of the energy correspondent to the $Q_{\beta\beta}$, because only a small fraction of the energy is transferred to the recoiling nucleus. Because of this, the signature of this decay has a mono-energetic peak at $Q_{\beta\beta}$ as Figure 2.11 shows.

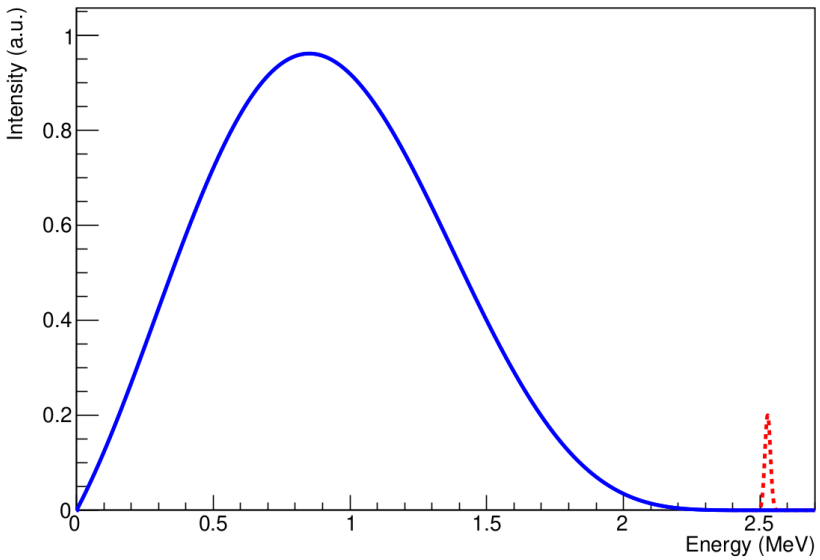

Figure 2.11: Illustration of the spectrum for $2\nu\beta\beta$ (blue) and $0\nu\beta\beta$ (red) decays for the ^{130}Te. On the bottom right corner of the picture is denoted the broadening of the $0\nu\beta\beta$ peak, which is has a theoretical discrete value, to denote the non zero energy resolution of a real detector. Image from [CDF21].

To observe the $0\nu\beta\beta$ decay, a detector must be able to distinguish the peak at the $Q_{\beta\beta}$ from the backgrounds. So a complete understanding of backgrounds is required to distinguish it from the real signal. The detector must also have a good enough energy resolution, in order to be able to observe an excess rate of events in relation to the *gamma* lines near the $Q_{\beta\beta}$.

Since the $0\nu\beta\beta$ decay is characterized by two electrons the topological resolution of the detector has a great impact on the discrimination between single and multiple scatter events, impacting therefore the sensitivity of an experiment, being that the focus of this thesis.

2.6.2 Probing $0\nu\beta\beta$ Mechanisms with Twin Isotopes

The existence of two isotopes from the same element, capable of decaying via $0\nu\beta\beta$ (same as for the $2\nu\beta\beta$ decay mode), constraints the uncertainties associated with the NMEs calculation and with the theoretical models themselves. This constraint is given by the ratio between the half-lives of the two isotopes, which are sensitive to the $0\nu\beta\beta$ decay mechanism. This ratio is given by

$$R_{\mathcal{M}^{0\nu}} = \frac{|\mathcal{M}^{0\nu,A_2}|}{|\mathcal{M}^{0\nu,A_1}|} = \sqrt{\frac{G^{0\nu,A_1}T^{0\nu,A_1}}{G^{0\nu,A_2}T^{0\nu,A_2}}} \tag{2.65}$$

where $\mathcal{M}^{0\nu}$ is the NMEs, $G^{0\nu}$ is the phase-space factor and A_1 and A_2 denotes the two different isotopes. However, $R_{\mathcal{M}^{0\nu}}$ does not depend on the lepton number violating parameters of the model (such as $\langle m_{\beta\beta}\rangle$) as they cancel out.

This possibility occurs with Xenon, in particular with ^{134}Xe and ^{136}Xe. Depending on the nuclear models, $R_{\mathcal{M}^{0\nu}}$ for Xenon takes different values, such as $R_{\mathcal{M}^{0\nu}} = 3.12$ for the renormalized quasiparticle random-phase approximation (QRPA) [SŠF96] if the decay is mediated by a heavy neutrino or $R_{\mathcal{M}^{0\nu}} = 2.00$ for the case of the light neutrino mediated.

2.7 Experimental Techniques for $0\nu\beta\beta$ searches

The predicted half lives for $0\nu\beta\beta$ decays depend on the nuclear models being considered, but are typically far greater than 10^{20} years, and inversely related with the Q-value of each isotope decay. The choice of target isotope for a $0\nu\beta\beta$ decay search experiment has to take into account this important factor, since a longer half life means an increased effort to find such a rare decay. But as in other fields of research, there are various other aspects to be considered. Those are the natural abundance, accessibility of the target isotope (this includes the ease of enrichment or extraction and its price) and the suitability of the technique to be used, since some isotopes properties may be not suitable for certain techniques. Table 2.1 shows some of the isotopes used for $0\nu\beta\beta$ decay search.

Isotope	Q-value [MeV]	Natural Abundance [%]
^{48}Ca	4.263	0.187
^{150}Nd	3.371	5.6
^{96}Zr	3.348	2.8
^{100}Mo	3.035	9.8
^{82}Se	2.998	8.7
^{116}Cd	2.813	7.5
^{130}Te	2.527	34.08
^{136}Xe	2.459	8.86
^{76}Ge	2.039	7.73

Table 2.1: Candidate isotopes for $0\nu\beta\beta$ decay ordered by decreasing Q-value and their respective natural abundance.

Because of the long half life, low background (BG) is a requirement that is strongly related with the technique and isotope used. Here, a high Q-value is a benefit, as most backgrounds are in the low energy region. The origins of this backgrounds are various, as they could be from cosmic

rays ($0\nu\beta\beta$ searches experiments are installed in deep underground laboratories to minimize this background), internal contaminants within the target material itself (such as radon) and from the various contaminants present in the detector components (such as thorium and uranium) and external coming from the rocks of the mines where the detectors are placed. Attenuation layers (such as lead shields or water surrounding tanks) are used for the identification and discrimination of external BGs and rejection veto systems are put in place for both of internal and external BGs.

Throughout the years, multiple techniques and isotopes have been developed and used. We can distinguish five main methods for the search of $0\nu\beta\beta$ decay: Bolometers, External Trackers, Scintillators, Semiconductors and Time Projection Chambers (TPCs). The next sections will be dedicated to briefly explain these techniques and give some examples of $0\nu\beta\beta$ decay experiments which use them.

2.7.1 Semiconductors

Semiconductors detectors are composed by crystal lattices of elements including Germanium (Ge), Selenium (Se) or Tellurium (Te), amongst others. This type of detectors measure the energy of an event by the collection of charges carriers (electrons) set free by an ionizing particle interacting with the semiconductor material. The material ionization creates electron-hole pairs which travel in opposite directions due to an applied electric field. Since the energy required to produce these pairs is known and independent from the incident radiation, a proportional relation between the electron-hole pairs and the energy of the incident radiation can be established.

Semiconductors can be highly purified with very little impurities on the crystal lattice, thus resulting in a very low background environment. Semiconductor detectors have the best energy resolution of all detection techniques, due to the very low statistical variation of the signal, possible by the reduced energy required to create an electron-hole pair. However, the up-scaling remains a challenging task, requiring a complexity increase of the apparatus to be able to accommodate a larger amount of crystals.

The Large Enriched Germanium Experiment for Neutrinoless double-beta Decay (LEGEND) will be installed at the Laboratori Nazionali del Gran Sasso, Italy, being a collaboration formed by the combined efforts of the GERDA (see Figure 2.12b) and the MAJORANA DEMONSTRATOR (MjD) collaborations [CS21]. The first one reached a sensitivity of $T^{0\nu}_{1/2} > 2.1 \times 10^{26} y$ [A^{+}20a] with an energy resolution ranging between 2,7(2) keV FWHM (0.13% FWHM) and 4.3(1) keV FWHM (0.21% FWHM) [A^{+}17a]. LEGEND will have two phases: LEGEND-200 (L-200) seen in Figure 2.12a and LEGEND-1000 (L-1000). The first will have 200 kg of HPGe crystals and the second 1000 kg, with an approximate 92% ^{76}Ge enrichment [LEG21]. The expected half-life sensitivity is $10^{27} y$ and $10^{28} y$ [GLC19] for L-200 and L-1000, respectively. The energy resolution will be at the same level as GERDAs and MjDs, with an upgrade (already tested on GERDA) on the detector crystals to prevent degradation over time. For future additional mass increases there are good prospects, as the energy resolution showed no dependency with the mass employed.

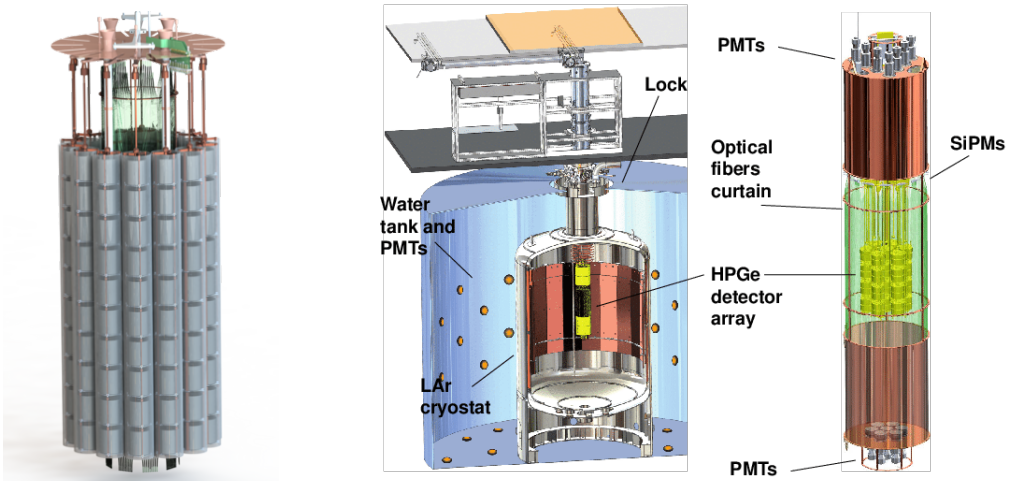

(a) LEGEND-200

(b) GERDA

Figure 2.12: **(a)** Rendering of the germanium crystals used by the LEGEND-200 detector [L20] and **(b)** rendering of GERDA apparatus on the left and on the right the target crystals are illustrated in detail [GER17].

2.7.2 Bolometers

Bolometers use crystals that contain the target isotope in their crystalline structure, such as ^{48}Ca, ^{82}Zn, ^{100}Mo, ^{116}Cd and ^{130}Te, which are connected to a thermal bath at cryogenic temperatures via a weak thermal link (resistance). When an interaction occurs, the deposited energy results in a very small temperature increase, changing the resistivity of the thermal link, that is subsequently measured.

The advantages of this technique are the low background due to the high purity levels of the crystals, made possible by the used crystal growth processes, and a very good energy resolution (similar to Semiconductor detectors), due to the high efficiency on counting statistics of phonons. This last characteristic being translated into the capability of measuring extremely small shifts in temperature (which are typically on the order of 0.1 mK per MeV of deposited energy [DPR19]), which is made possible by the usage of highly sensitive thermometers. Those range from semiconductors as neutron-transmited-doped (NTD) Germanium (Ge) or Silicon (Si) to metallic magnetic calomiters (MMC), between others. As this technique uses cryogenic temperatures, the up scaling for ton scale detectors becomes a challenging task. Three major experiments using this technique are CUORE, CUPID and AMoRE.

The Cryogenic Underground Observatory for Rare Events (CUORE) (Figure 2.13 on the right) is located at the Laboratori Nazionali del Gran Sasso, Italy and uses, as target isotope, ^{130}Te on the form of extremely pure Tellurium Dioxide (TeO_2) crystals, which function both as source and detector. The crystals are arranged in a cylindrical matrix of 19 towers with 13 floors, each one composed of 4 crystals (detector modules) within a copper frame. These towers are then placed inside a custom-made cryostat, keeping the crystals at approximately 10 mK [A$^+$17c]. The total amount of TeO_2 is 988 Kg containing 206 Kg of ^{130}Te [A$^+$21a]. The experiment set

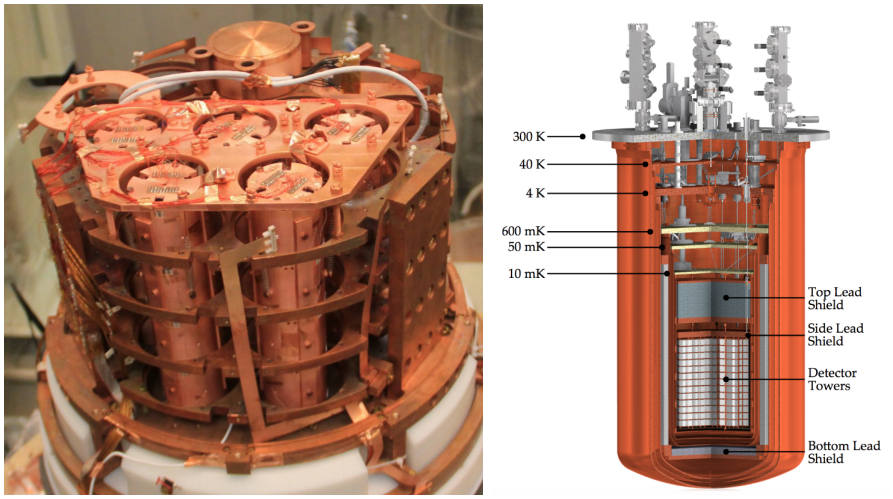

Figure 2.13: (left) Photography of the CUPID-Mo apparatus installed on the EDELWEISS set-up [A$^+$20e] that uses 21 kg of ^{100}Mo. (right) Rendering of the full CUORE apparatus [A$^+$17c] with the various levels of refrigeration and the multiple shields for background reduction.

a lower half life limit of $T^{0\nu}_{1/2} > 2.2 \times 10^{25} y$ (90% $C.I.$), corresponding to an effective Majorana mass of $|m_{\beta\beta}| < 90 - 135$ meV, achieving an energy resolution of 7.8 ± 0.5 keV FWHM or 0.3% at $Q_{\beta\beta}$ [A$^+$21a][A$^+$21b].

The CUORE Upgrade with Particle IDentification with Molybdenum (CUPID-Mo) (Figure 2.13 on the left), as the name implies, is an evolution of CUORE which will use the same cryostat but ^{100}Mo is used instead of ^{130}Te, on the form of Molybdenum-enriched (more than 95%) Di-Lithium Molybdate ($Li_2^{100}MoO_4$) crystals, acting both as source and detector [Gro19]. For CUPID baseline and CUPID-1T, 6 mK temperatures seem to be feasible according to the cryostat commissioning results [Gro19]. CUPID-Mo presented a result for the half life of $T^{0\nu}_{1/2} > 1.5 \times 10^{24} y$ [A$^+$21e], corresponding to an effective Majorana mass of $|m_{\beta\beta}| < 310 - 540$ meV, with an expected energy resolution on the order of less than 1% at 2615 keV [A$^+$21e].

2.7.3 External Trackers

External Trackers, also known as Tracking Calomiters, use thin foils of source isotope between two regions filled with tracking gas at low pressure (the tracking layers) surrounded by calomiters (scintillators) coupled with PMTs. The event reconstruction is made using calomiter information, which identifies and gives the topological information, were the magnetic field present in the tracking layers identifies the charge of the particle.

The advantages of this technique are the very good topological reconstruction, which leads to a large efficiency of background discrimination and can also measure the angle between the two electron paths from a $0\nu\beta\beta$ decay. However, there are also disadvantages as the thin foils used make it difficult to construct a ton scale detector due to the poor size-isotope mass ratio of this type of detectors.

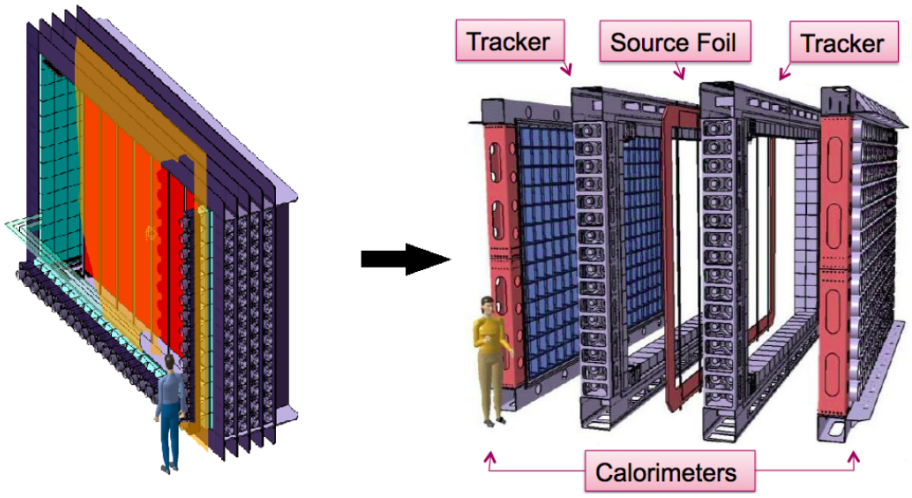

Figure 2.14: Graphical representation (human for reference) of a single SuperNEMO demonstrator module (left) and its exploded-view (right), where the various components are labeled. Image from [Gro].

SuperNEMO (Figure 2.14) is an experiment which uses this technique an is located in the Modane Undergroung Laboratory, France, improving on the work done by NEMO-3 (which set an half life time of $T^{0\nu}_{1/2} > 1.1 \times 10^{24} y$ (90% $C.L.$) for ^{100}Mo [Gó16]). SuperNEMO will use ^{82}Se as source isotope divided into 34 foils with a total mass of 6.3 Kg [Jer20] and has a projected sensitivity of $T^{0\nu}_{1/2} > 10^{26} y$ [Pah08]. The energy resolution is improved from [14-17]% FWHM at 1 MeV [Gó16] for NEMO-3 to $7\%/\sqrt{E}$ (4% at $Q_{\beta\beta}$) [Pah08].

2.7.4 Scintillators

Scintillators rely on the physical property of luminescence, in which a material emits light after an interaction with an incident particle with enough energy to exceed the excitation energy of the target. Scintillators can be divided into two categories: inorganic and organic.

Inorganic scintillators are crystals grown in high temperature furnaces. They usually have high density, high atomic number and a decay time on order of the microsecond. The scintillation arises from the crystalline structure (crystal lattice). The main difficulty of this technique for $0\nu\beta\beta$, which uses ^{48}Ca, is the enrichment of the crystal, given that this source isotope has only 0.187% of natural abundance.

Organic scintillators get their scintillation from transition levels of molecules or atoms. The pulse decay times are 100 times faster than the inorganic counterparts. Organic Scintillators for $0\nu\beta\beta$ searches usually use Liquid Organic Solutions, which are made by dissolving an organic scintillator in a solvent. This technique can be easily scalable to multi tonne experiment, which counteracts the worse energy resolution compared with other techniques.

The Kamioka Liquid ANtinneutrino detector with Xenon (KamLAND-Zen / KLZ) is located at the Kamioka Observatory (Hida), Japan. The first iteration of the experiment (KLZ400) 2.15

used liquid at 37,5% enriched ^{136}Xe diluted in a liquid scintillator. KLZ400 reached a sensitivity of $T^{0\nu}_{1/2} > 1.07 \times 10^{26} y$ with an energy resolution of of 4.7% at $Q_{\beta\beta}$ [SftKZC17].

KLZ800 has the objective of reaching the sensitivity to probe the Inverted Hierarchy region [SftKZC17]. It uses 745 kg of 91% enriched Xenon [Li21] and with $2\nu\beta\beta$ background rejection, is expected to reach approximately an energy resolution of 2% FWHM at $Q_{\beta\beta}$ [SftKZC17]. As of now, KLZ800 has provided a first result for the half life of $T^{0\nu}_{1/2} > 2.3 \times 10^{26} y$ [Zen22].

The Sudbury Neutrino Observatory Plus (SNO+) (see Figure 2.15 on the right) experiment is located in the SNOLAB (Vale's Creighton Mine), Canada. It uses 780 tonnes of ^{nat}Te-loaded liquid scintillator (Te-LS) (1300 Kg of ^{130}Te as the source isotope) inside an Acrylic Vessel (AV).

For the half life, the expected sensitivity after 5 years is $T^{0\nu}_{1/2} > 2.1 \times 10^{26} y$ [A$^+$16a]. This result is for a 0.5% ^{nat}Te loading (by mass), corresponding to a total mass of Te of 3,9 tonnes. For larger loading of Te, the sensitivity may reach the $T^{0\nu}_{1/2} > 10^{27}$, being therefore able to probe the inverted hierarchy region [A$^+$16a]. The expected energy resolution is set for a few hundreds of keV (about 4 to 10% FWHM [A$^+$16b]).

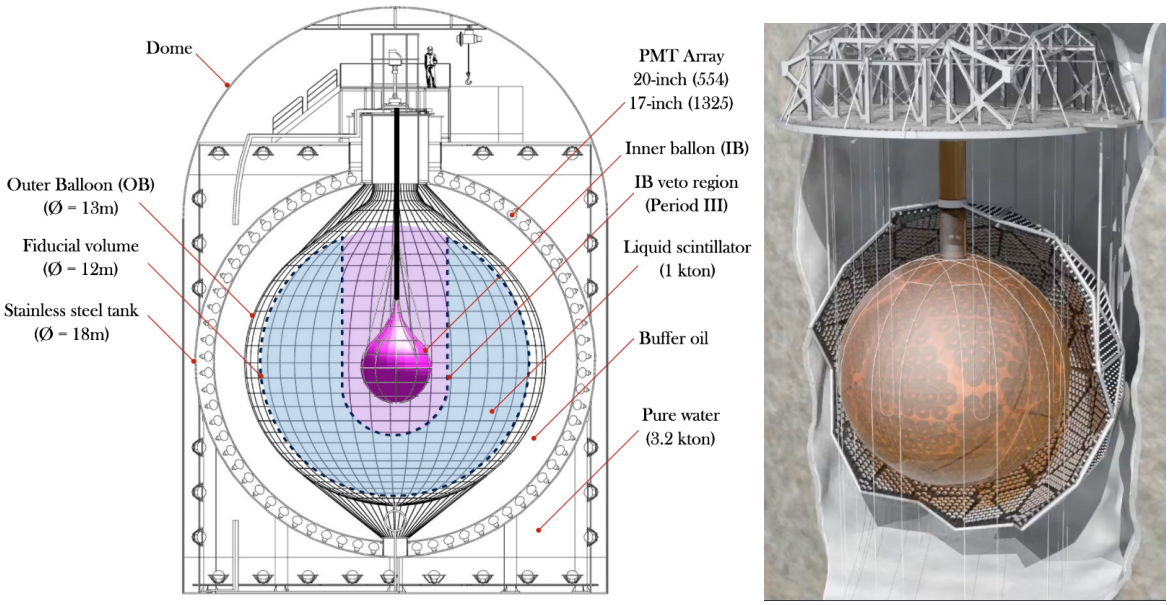

Figure 2.15: Schematic of the KamLAND-Zen 400 apparatus (left). The Inner Balloon (IB) contains the $^{enr}Xe + LS$ solution, surrounded by the Outer Balloon (OB) filled with liquid scintillator to detect $\bar{\nu_e}$. The outer most layer is filled with mineral oil (buffet oil) used to reduce γ radiation from internal and external radioactive contaminants. Surrounding all this are the PMTs which detect the scintillation light [A$^+$22d]. Rendering of the SNO+ (right) apparatus where the AV (orange sphere) contains the Te-LS and has 12 m of diameter, surrounded by a constellation of 9362 PMTs submersed in 7000 tones of ultra-pure water, providing passive shielding from radioactive contaminants from the cavern walls [A$^+$16a].

2.7.5 Time Projection Chambers

A Time Projection Chamber (TPC) consists in a volume filled with a medium in a parallel and uniform electric (and possibly also a magnetic) field, capable of measuring the position and energy of an ionizing interaction. The medium can be in different states, either gas, liquid, both (dual-phase) or even solid [CA13]. These detectors can use two energy channels: scintillation, ionization or both. These signals are used to reconstruct the topology, position and energy of the event. If both scintillation and ionization signals are used, the commonly denomination given to them is S1 and S2 signals, respectively. The S1 signal sets the initial event detection and ionized electrons drift to produce the S2 signal. The time delay between the S1 and the S2 (electron or light collection) signals gives the position in relation with the anode and cathode.

For $0\nu\beta\beta$ decay searches xenon has been the *status quo* choice due to its high density and the fact that contain isotopes that may decay via $0\nu\beta\beta$ decay. The single-phase gaseous TPCs, which use high-pressure Xe gas (about 15 Bar) offer the best energy resolution (less than 0.5% FWHM at $Q_{\beta\beta}$) and the possibility to reconstruct the tracks of the emitted electrons, but the single-phase liquid TPCs offer the greatest source density. The dual-phase TPCs try to achieve both high source density and good energy resolution. This is done by keeping the liquid close to its boiling point, as a mean to create a liquid-gas interface. The importance of the coexisting gas phase stands on the multiplication factor between the ionized electrons and the light production in the gas-phase (electroluminescence). Moreover, the self-shielding and high density of Xe, and the single-electron detection using electroluminescence makes the dual-phase TPCs one of the best techniques for the research of rare events, such as the $0\nu\beta\beta$ [DPR19].

All the different approaches for xenon TPCs are used for $0\nu\beta\beta$ searches. The Enriched Xenon Observatory (EXO) uses 80,6% of ^{136}Xe enriched liquid with a total mass of 161 kg. The sensitivity obtained for the half time life was $> 3.5 \times 10^{25} y$, corresponding to an effective Majorana mass of $|m_{\beta\beta}| < 93-286$ meV [A^{+}19]. The neutrinoless EXO (nEXO) experiment will be built in SNOLAB, Canada, being filled with 90% enriched liquid Xe (about 4600 Kg of ^{136}Xe) [nEX18]. The projected sensitivity for the half life $T^{0\nu}_{1/2} > 9.2 \times 10^{27} y$, corresponding to an effective Majorana mass of $|m_{\beta\beta}| < 21 - 69$ meV [nEX18]. Reaching an energy resolution of approximately 1% FWHM [nEX18]. Also, the Neutrino Experiment with a Xenon TPC (NEXT) will use 91% of ^{136}Xe enriched gas with a total mass of 100 kg. The projected sensitivity for the half life is $> 6.0 \times 10^{25} y$, corresponding to an effective Majorana mass of $|m_{\beta\beta}| < 80 - 160$ meV, achieving an energy resolution close to 0,5% FWHM near the $Q_{\beta\beta}$ [MA^{+}15]. The dual-phase approach is the main focus of the thesis and it will be discussed in detail in the next Chapter, which is centered around the LUX-ZEPLIN experiment and a future third generation (G3) detector.

Chapter 3

The LUX-ZEPLIN Experiment

LUX-ZEPLIN (LZ) is an experiment searching for dark matter (DM) in the form of weakly interactive massive paricles (WIMPs) and other rare events, located at the Sanford Underground Research Facility (SURF) in Lead, South Dakota, USA. The LZ detector is assembled in the Davis cavern at a depth of 1478 meters (4850 feet), which is equivalent to 4300 m of water depth. Because of the DM search focus, LZ has the ability of observing low energy nuclear recoils (NR), which are the characteristic signature of WIMPs. The LZ collaboration results from the merging of the LUX and ZEPLIN collaborations, with its design being highly influenced by its parent detectors (LUX and ZEPLIN) [A$^+$20d].

LZ is a dual-phase xenon time projection chamber (TPC), meaning that inside of the detector exists a liquid and a gas phase, with a total active mass of 7 tonnes. After 1000 live days it is projected to exclude at 90% confidence level the spin-independent WIMP-nucleon interaction cross Section above 1.4×10^{-48} cm^2 for a 40 GeV/c^2 mass WIMP [A$^+$20c]. For the $0\nu\beta\beta$ decay of the ^{136}Xe it is expected to have a sensitivity half life of 1.06×10^{26} years [A$^+$20d]. The detection of an event is done by measuring two light signals, S1 and S2, which correspond to prompt scintillation light and to electroluminescence light, respectively. From the relative magnitudes of those signals, the nature of the interaction is inferred, whether it is a nuclear recoil (NR) or an electron recoil (ER) resulting from interactions with the atomic electrons. Also the position of the event can be determined from the drift time delay between the S1 and S2 signals (z coordinate) and from the spatial distribution of the S2 signal (xy plane).

As visible in Figure 3.1 the LZ TPC is placed in the center of the full apparatus, being radially surrounded by the Skin veto region that also contains LXe, which acts as an electrical standoff and as a veto to gamma rays and neutron interactions. The TPC and the Skin are housed inside the inner cryostat vessel (ICV), which is operated at 174.1K and 1.791 bar [A$^+$22b], that is suspended inside the outer cryostat vessel (OCV), completing the inner detector (ID). Between

the ICV and OCV there is a vaccum region acting as a thermal insulator. The Outer Detector (OD) is composed of 9 acrylic vessels filled with Gadolinium loaded liquid scintillator (GaLS) which is enclosed by the water tank, where an array of 120 PMTs is mounted looking inwards on a wall between the water tank wall and the acrylic vessels (see Figure 3.1).

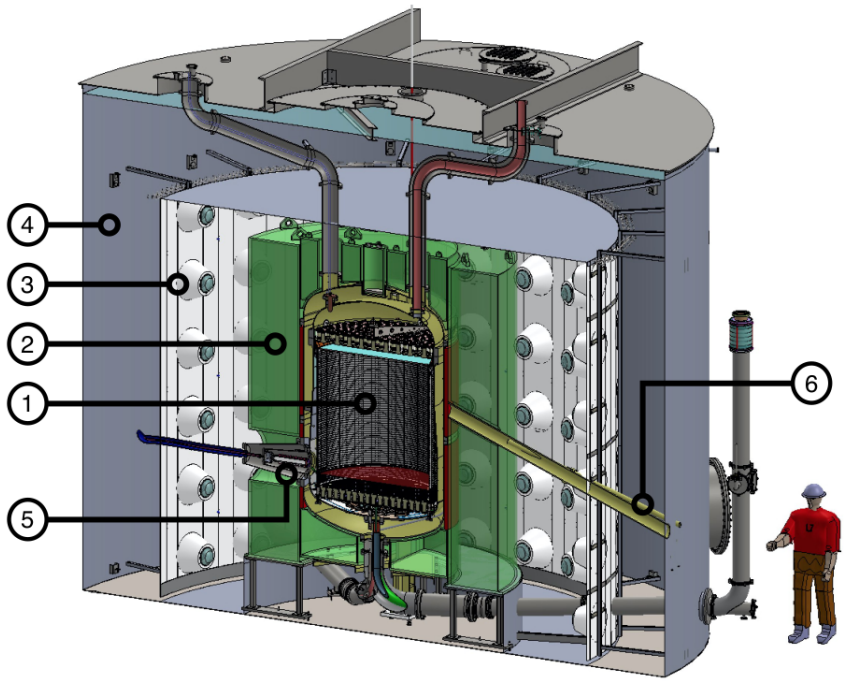

Figure 3.1: Rendering of the LZ detector apparatus with the TPC placed in the middle **(1)**, surrounded by the acrylic vessels filled with GdLS **(2)**, which in itself is inside a water tank **(4)** where an array of PMTs looking inwards is mounted **(3)**. Are also visible the cathode high voltage feed through **(5)** and the external neutron source tube **(6)** for calibrations. Image from [A$^+$20d].

3.1 The Time Projection Chamber

The drift region of the TPC has 145.6 cm of inner diameter and height. In the TPC there are four grids which establish the electric fields. In an ascending order, are found the bottom and cathode grids which sit near the bottom of the TPC and near the top sit the gate and anode grids (see Figure 3.2). Below the cathode, the reverse field region has 13.78 cm, bordered below by the bottom grid which shields the array of 241 PMTs arranged in a close package hexagonal pattern (Bottom array). Above the gate grid (which along with the cathode, establishes a drift field in the liquid phase) sits the anode grid. The liquid-gas interface is between the gate and the anode grids, 5 mm above the former and 8 mm below the latter [M$^+$17]. The top PMT array is 5 cm above the anode grid and is composed of 253 PMTs, which are arranged on an hexagonal pattern in the center which changes to a circular pattern at the perimeter. This layout was chosen to optimize the xy position reconstruction of the S2 signal near the TPC walls. Both arrays are composed of Hamamatsu R11410-22 PMTs, a variant tuned particularly for LZ [A$^+$20d]. The walls of the TPC (field cage) are composed of 58 rings of Polytetrafluoroethylene

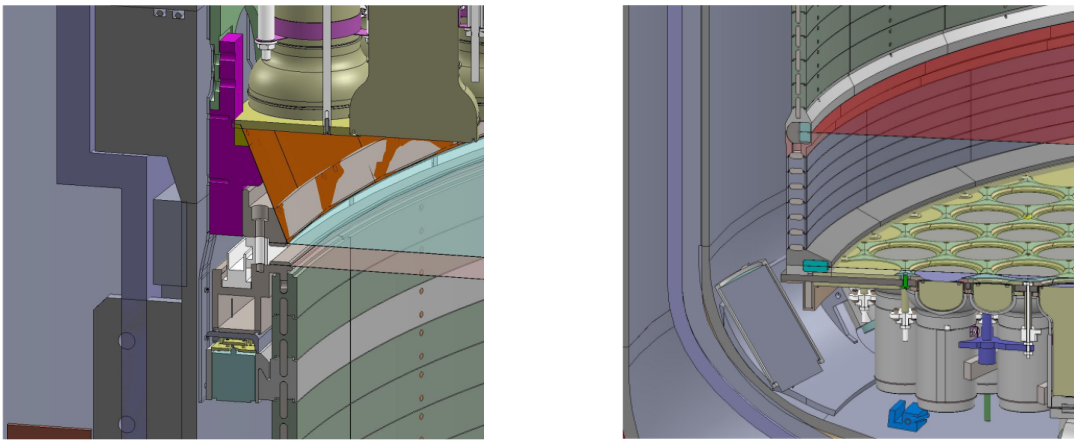

(a) **(b)**

Figure 3.2: Rendering of **(a)** the top of the TPC where the Anode (blue) and Gate (grey) grid meshes can be found, with part of the top PMTs array above it and **(b)** the bottom where the Cathode (red) and Bottom (translucent) grid meshes are placed. The bottom PMTs are mounted just below the Bottom grid and the PTFE panels (green for the ones above the cathode and grey below it) coat the lateral wall of the TPC. Set between the PTFE panels are the titanium shaping rings (grey). Image from [M$^+$17].

(PTFE), each one composed of 24 segments 25 mm tall, for electrical insulation and for its high reflectivity ($\geq 97\%$) [N$^+$17] to maximize light collection of the scintillation signal. The S1 signal consists of the primary collection of scontillation photons, produced by an interaction in the LXe phase. The segmented field cage prevents excessive charge accumulation observed in larger PTFE panels [A$^+$17b] and also reduces the stress caused by thermal contraction as the material is subject to large temperature variations. It is important to maximize the photon collection, as this determines the detector's threshold. This is done by the use of high quantum efficiency PMTs optimized for the wavelength of vacuum ultraviolet (VUV) photons.

As was previously mentioned, an electric filed is applied in the LXe, called drift field, that conducts the electrons from the event position to the Gas phase. This field has nominal magnitude of 193 V/cm in the active region. The extraction field which accelerates the electrons in the gas-phase has a magnitude of 7.3 kV/cm at the radial center of the TPC [A$^+$22b]. To establish these fields a set of grids are mounted, being made of stainless steel in a cross mesh design with a 90^{o} angle between the wires. The choice of this design was done to reduce the load on the support ring, as the tensions are more evenly distributed comparatively to a parallel wire setup. To ensure that the field remains uniform, a set of 57 titanium shaping rings are mounted between the PTFE panels (see Figure 3.2). Since the wires support each other, the mesh is also more robust, making the fields more stable as the wire distortions are minimized. The specifications of the grids are summarized in Table 3.1.

Electrode	Diam. [μm]	Pitch [mm]	Number
Anode	100	2.5	1169
Gate	75	5.0	583
Cathode	100	5.0	579
Bottom	75	5.0	565

Table 3.1: Parameters of all TPC grids where the pitch is the distance between the centers of the wires. Values taken from [M$^+$17].

The S2 signal is generated by ionization electrons when they enter into the gas phase (electroluminescence region), where they are accelerated by an electrical field (see Figure 3.3). This acceleration gives the electrons enough energy to collide with xenon atoms to produce Xe_2^* excimers (see Section 3.3 for a detailed discussion on the excimers production), which in turn decay and produce photons with a characteristic wavelength, in the vacuum ultraviolet (VUV) region. The number of VUV photons produced is proportional to the path length of the electron. As the electric field is established by two grids, the electrons will have different paths because some will be directly under a wire and others may have to bend their trajectory to reach it, travelling therefore a longer path and thus will produce more light [CA13]. The effect of the different paths of the electrons in the gas phase does not significant impact the shape of the waveforms, as the different path directions will even out. The operating pressure of the gas phase for the first *science run* (SR1) was 1.791 bar [A$^+$22b]. Each electron produces an average of 635 VUV photons each, which are mostly detected by the top array PMTs with a detection efficiency for SR1 of 0.0921 photons detected per photon produced.

3.2 Veto Systems

The veto systems provide the LZ experiment with a powerful discrimination mechanism for internal and external radioactive backgrounds. Rare events, such as WIMP interactions or rare decays, are only expected to generate signal in the TPC, while gammas and neutrons have a high probability of also interact with the vetoes, allowing their exclusion. These are the Skin Detector (Section 3.2.1) and the Outer Detector (Section 3.2.2), which help in the event discrimination of gammas and neutrons from radioactive contaminants in the detector building materials and high energy γ-rays originated from the cavern walls.

3.2.1 The Xenon Skin Detector

The Skin detector sits between the ICV and the PTFE light reflector cage, containing around 2 tonnes of LXe acting as a dielectric insulator and as a scintillation-only veto detector (primarily for gamma rays). This reduces the amount of background, as light from particle interactions or electrical breakdown in this region could be interpreted as a signal in the TPC.

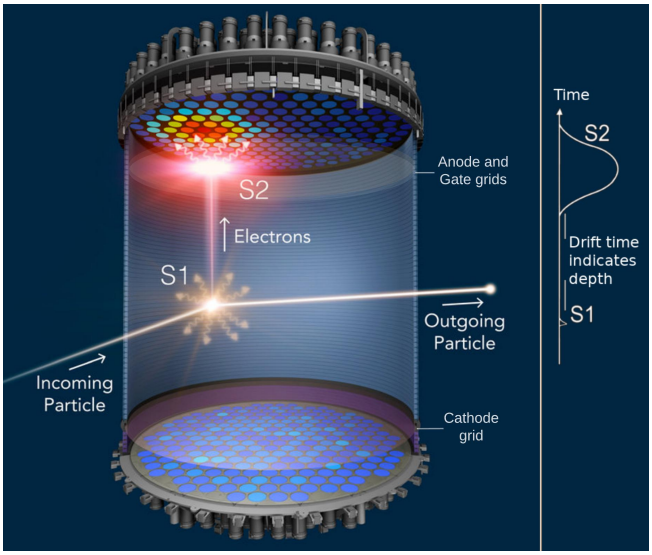

Figure 3.3: Illustration of an event in a dual-phase xenon TPC, where the interaction first produces primary scintillation light (the S1 signal) and the extracted electrons produce secondary scintillation when reaching the gas phase via electroluminescence (the S2 signal). From the difference between the S1 and S2 signal the vertical position can be inferred as the drift velocity is constant in the active volume due to the uniformity of the the electric field, and from the light distribution of the S2 signal in the top PMT array the XY position can be reconstructed. Image from [M$^+$17].

The ICV has a 4 cm radial separation from the PTFE light reflector cage at the top, widening to 8 cm at the cathode level to increase the standoff distance (because the voltage applied on the bottom of the TPC is higher). This side Skin region is instrumented on the top with 93 1-inch Hamamatsu R8520-406 PMTs and at the bottom with 20 2-inch Hamamatsu R8778 PMTs [M$^+$17]. The Skin is not only present on the sides of the TPC, but also on the ICV bottom dome (which is located below the TPC), where 18 additional R8778 PMTs are mounted horizontally with a radial disposition (12 looking outward and 6 inwards as seen in Figure 3.4). These PMTs are covered by PTFE, as well as the ICV and other structures in the same region, to improve light collection. Because of the coating of the PMTs and the reflectivity of the walls, it is possible to observe in 95% of the Skin volume energy depositions superior to 100 keV.

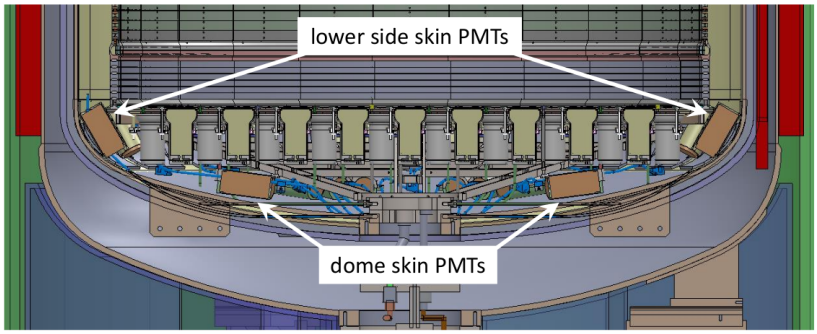

Figure 3.4: Rendering of the bottom dome of the LZ detector Skin. The bottom PMTs (brown) are divided in two groups: 20 lower side Skin PMTs facing upwards and 18 dome Skin PMTs (6 looking inwards and 12 outwards). The shells of the ICV and OCV are also visible (grey). Image from [M$^+$17].

3.2.2 Outer Detector

The Outer Detector (OD) surrounds the cryostat and its composed of 4 acrylic vessels on the side, 3 on the bottom, 2 on top and one plug (which can be removed to deploy $^{205}BiBe$ or ^{88}YBe photoneutron sources) as seen in Figure 3.5. Theses acrylic vessels are all contained inside a water tank, with 20 equally spaced ladders of 6 8-inch Hamamatsu R5912 PMTs looking inwards to the acrylic vessels.

The energy threshold is set at 200 keV (minimal detection of 37.6 photoelectrons with approximately 7% of detection efficiency [A$^+$20d]) to avoid the ^{14}C decay with an energy of 156,5 keV that is present in the liquid scintillator. The main purpose of the OD is to moderate and capture neutrons originated from the radioactive impurities in the materials used outside the TPC. This is done by filling the acrylic vessels with 17.3 tonnes of Gadolinium doped liquid scintillator (GaLS), as the Gd has a high neutron capture cross Section [M$^+$17]. The neutrons are detected mainly by the capture on ^{155}Gd and ^{157}Gd, emitting a photo-cascade (on average 4,7 gamma rays) with an energy of 7.9 MeV and 8.5 MeV, respectively. Hydrogen neutron capture also occurs with a frequency of 10%, producing a single photon of 2.2 MeV. To enhance light collection, curtains of Tyvek (a synthetic high density polyethylene fiber which is water proof for the liquid water phase) cover most of the surfaces within the OD [M$^+$17].

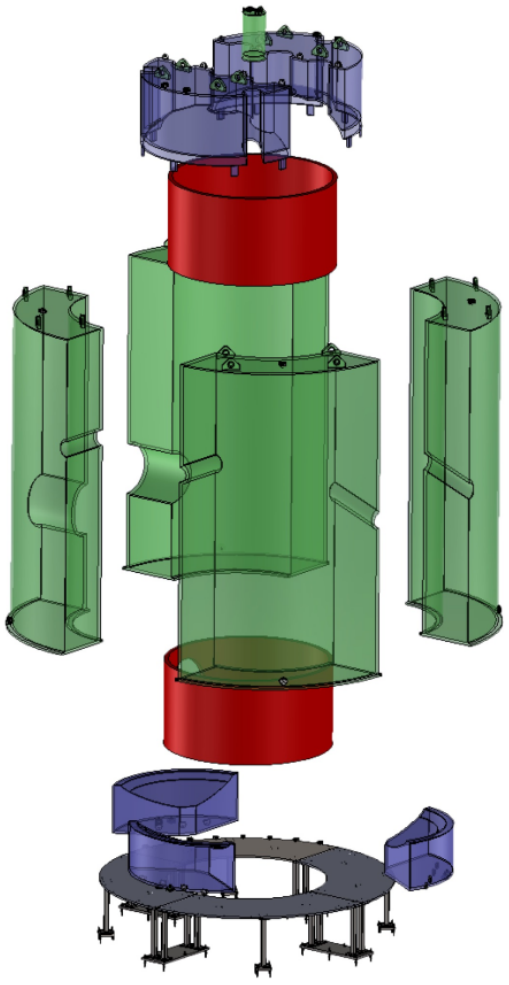

Figure 3.5: Exploded view of the lateral (green), top and bottom (blue) acrylic vessels surrounding the OCV, plus the top plug (green on top) where the Calibration Source Delivery system is mounted. Also the water displacements (red) and the base support system (grey) are shown. Image from [A$^+$20d].

Another important aspect of the OD is the presence of a water displacement (WD) layer between the OCV and the lateral acrylic vessels, which is composed by a foam (because of its low density) to prevent neutron moderation in the water, and therefore not lose the neutron capture signature of 2.2 MeV (Hydrogen capture). This signature would be lost without the WD since the water does not scintillate. Also, for time-coincidence purposes, it is needed that neutrons that interacted in the TPC volume are not thermalized before the OD.

To maximize neutron capture efficiency, the Gd concentration of 0.1% was chosen to make the hydrogen capture channel sub-dominant (10% as was previously mentioned). Another consequence of the

Gd doping level used is justified by the reduction of the average capture time of thermal neutrons in the LS from 200 μs to 30 μs. As this is an average, some neutrons may have longer survival time until they are captured, thus the use of a time window of 500 μs allows a detection efficiency of 96.5% for a 200 keV threshold [M$^+$17]. The OD, combined with the Skin veto (using Monte Carlo simulations) is expected to allow a reduction efficiency on NR backgrounds in 1000 live-days of about 90% [A$^+$20d].

3.3 Xenon Physics

Liquid noble elements, compared with other detector mediums, offer a distinctive response to incident radiation where both scintillation photons and ionizing electrons are produced. This results in a better characterization of interactions in the detector. Compared to other noble elements such as argon, xenon has a higher and narrower temperature range (from about 162 K to 165 K at 1 atm) where it remains in the liquid phase, meaning that electronegative contaminants are harder to remove since they do not freeze out [AD10]. However, the development of xenon purification systems led to the required level of purity, even for multi ton detectors.

Liquid xenon has a density around 2.942 g/cm^3. This high density makes it very efficient at stopping penetrating radiation. It has 9 natural occurring isotopes none of which are short-lived, with 2 of them being candidates for $0\nu\beta\beta$ decay (^{134}Xe [A$^+$21c] and ^{136}Xe [A$^+$20b]).

The emission of luminescence (scintillation) in rare gases is due to the decay of excited excimers to the ground state (short lived molecules formed by two species where at least one of them has a complete valence shell). For LXe, the scintillation light has a wavelength centered at 171 nm (VUV photons), which is the characteristic decay energy of the excited excimer Xe_2^*. This excimer is created by two different processes, one involving excited atoms (Xe^*) and the other ions (Xe^+), shown in Equations 3.1 and 3.2, respectively [AD10].

$$\begin{aligned} Xe^* + Xe + Xe &\longrightarrow Xe_2^* + Xe \\ Xe_2^* &\longrightarrow 2Xe + \gamma \end{aligned} \tag{3.1}$$

$$\begin{aligned} Xe^+ + Xe &\longrightarrow Xe_2^+ \\ Xe_2^+ + e^- &\longrightarrow Xe^{**} + Xe \\ Xe^{**} &\longrightarrow Xe^* + heat \end{aligned} \tag{3.2}$$

The scintillation yield is the number of photons produced by an incident ionizing radiation of energy E, which is E/W_{ph}, where W_{ph} is the average energy required to produce a single photon assuming that there is no photon reduction processes, given by [AD10]

$$W_{ph} = \frac{W}{1 + N_{ex}/N_i} \tag{3.3}$$

where W is the average energy required to produce an electron-ion pair and N_{ex} and N_i are the number of excitons and electron-ion pairs produced, respectively. The density of electron-ion pairs produced along the path of a particle, called linear energy transfer (LET), directly influences the scintillation yield. This is due to the recombination probability between electrons and ions having a dependency with the density of electron-ion pairs. The excimer Xe_2^* decay has two time components, since it can be in a singlet or triplet state. The observed singlet decay time may give information about the type of interaction, since the production fraction of each excimer depends on the recoil type (ER or NR) and $^{dE}/_{dx}$. This distinction only occurs when no electric field is applied. But for LXe, when an electric field is applied the discrimination over ER/NR is more effectively done by measuring the relation between the S1 and S2 magnitudes, which is the case for the LZ experiment.

For NRs, the excitation density is higher than the one for ERs [AD10]. The ratio between the scintillation yields for these two process types, dubbed relative scintillation efficiency ($\mathcal{L}_{eff}$) is of importance for LXe detectors, as a mean of inferring the detectors sensitivity to dark matter WIMPs. Compared to ER events, NR events have substantially less scintillation due to quenching (energy lost to heat, which is not detected) for the same energy deposited.

When an incident particle interacts with the LXe, the energy deposited (E) generates electron-ion pairs in proportion to its magnitude. This relation can be expressed by [AD10]

$$E_0 = N_i E_i + N_{ex} E_{ex} + N_i \epsilon \tag{3.4}$$

where N_i is the number of electron-ions pairs produced, E_i is the average expenditure of energy for electron-ion pair production, N_{ex} is the number of excited atoms produce, E_{ex} is the average expenditure of energy for excited atom production and ϵ is the average kinetic energy of the sub-exciton electrons. The W value is defined as

$$W = {}^{E_0}/_{N_i} = E_i + E_{ex}\left(\frac{N_{ex}}{N_i}\right) + \epsilon \tag{3.5}$$

This value has very little dependence on the type and energy of the incident radiation, being considered constant. For this reason the number of electron-ion pairs created is proportionally related with the deposited energy. However, for the correct measure of the energy, it is essential to have a high purity level to minimize the capture and subsequent loss of charge carriers.

The electron-ion pair production has a uncertainty (for an incident ionizing particle that deposited all of its energy in the medium) given by [AD10]

$$\delta^2 = \left\langle (N - N_i)^2 \right\rangle = F \times N_i \tag{3.6}$$

where F is the Fano factor, which is less than 1 and depends on the medium. The Poisson distribution is the limit case when F=1. So the final energy resolution (ΔE) limit for LXe

detector takes the form

$$\Delta E(keV) = 2.355\sqrt{F \cdot W(eV) \cdot E(MeV)} \tag{3.7}$$

where $W(keV)$ is the W-value in keV and $E(MeV)$ is the energy of the incident particle in MeV. The best energy resolution, to date, has been from the LZ experiment with $\Delta E = 0.67 \pm 0.01\%$ at 2614 keV [Per22] (theoretical limit in the LXe $\Delta E = 0.14\%$ FWHM using the F and W values from [AD10]).

The excess of ionizing electrons can be efficiently extracted from the liquid to the gas phase by the application of an electric field, which will suppress the recombination of electron-ion pairs. For low fields, the drift velocity (v_d) of electrons can be considered proportional to the electric field together with a proportionality constant defined as the electron mobility, μ_e. For higher fields, the the drift velocity becomes electric field independent. In the presence of an electric filed, the dispersion of charges (i.e. diffusion) is no longer isotropic, so two components arise: the transversal diffusion (D_T) and the longitudinal (D_L). From the drift time, it is possible to calculate the transversal diffusion spread (σ_{D_T}) of the free electron cloud using the equation from [AD10] given by

$$\sigma_{D_T} = \sqrt{D_T t_d} \tag{3.8}$$

where t_d is the drift time, which is defined as

$$t_d \simeq {}^{d}/_{v_d} \tag{3.9}$$

where d is the path distance of the charge carriers. For the longitudinal diffusion the spread (σ_{D_L}) is given by [Sor11]

$$\sigma_{D_L} = \sqrt{\frac{2D_L t_d}{v_d^2} + \sigma_0^2} \tag{3.10}$$

where σ_0 is a free parameter.

The longitudinal component of the diffusion is smaller than the transversal component and the ratio ${}^{D_L}/_{D_T}$ will tend to 1 for zero electric field [CA13].

Electro-negative impurities can reduce the number of electrons as they drift to the surface. This process is described by the following expression

$$X + e^- \longrightarrow X^- \tag{3.11}$$

where X and X^- represent an electro-negative impurity and its respective ion and e^- represents an electron. The temporal variance of the electron concentration is given by

$$\frac{d[e]}{dt} = -k_X[e^-][X] \tag{3.12}$$

where the square brackets denote the concentration of a substance and k_X is the attachment rate constant in the units of $dm^3 mol^{-1} s^{-1}$. The Equation 3.12 leads to

$$[e(t)] = e(0)e^{-k_X[e^-][X]} \tag{3.13}$$

with the characteristic time, known as the electron lifetime, given by

$$\tau = (k_X[X])^{-1} \tag{3.14}$$

To minimize this effect, the experiments use noble elements purification systems to extract as much impurities as possible. With the purification systems implemented in LZ it was reached an attenuation length of at least 100 meters.

The energy reconstructions of an event in a dual-phase TPC detector is made using the primary scintillation, which occurs as some electron-ion pairs recombine and the secondary scintillation, which correspond to when the drifted electrons reach the gas-phase of xenon and produce scintillation. These two signals, given in units of *photons detected*, are dubbed S1 and S2, respectively. The energy of an event is then given by

$$E = W\left(\frac{S1}{g_1} + \frac{S2}{g_2}\right) \tag{3.15}$$

where the W uses a mean value and g_1 and g_2 are the detector dependent gain factors.

3.4 Backgrounds

The LZ experiment has the requirement of having a very small background count, especially in the central region of the TPC. As was previously mentioned, several means of background rejection and anti-coincidence techniques were implemented to this goal. Despite the deep underground placement of the detector (4300 m.w.e.), passive shielding, veto detectors and the self shielding nature of the xenon, there are still background sources that have an influence in the LZ sensitivity that must be taken into account. The xenon itself will produce BG as some of its isotopes decay (although with very long half lives), such as the case of ^{136}Xe that decays via $2\nu\beta\beta$ decay and ^{124}Xe that decays via $2\nu 2EC$. Figure 3.6 shows the energy spectrum of LZ background where is noticeable the gradual decrease for higher energies.

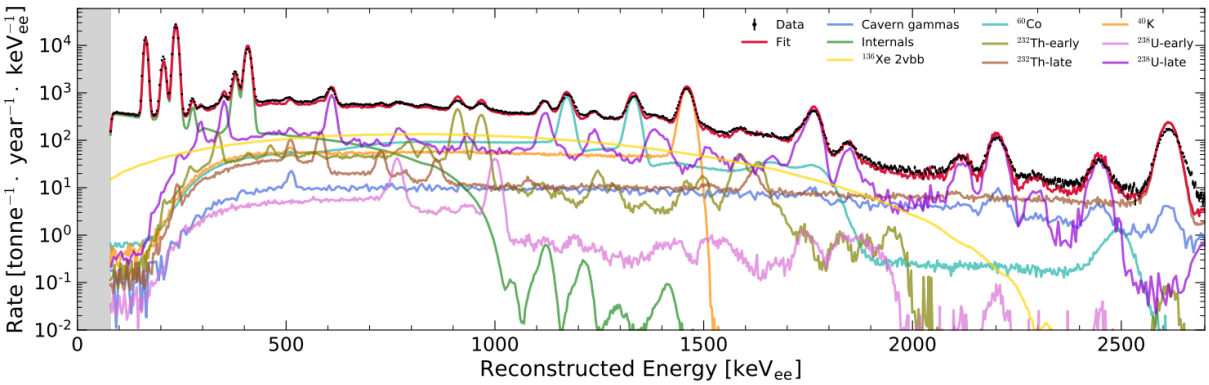

Figure 3.6: Energy spectrum of LZ backgrounds event rate from first science run (SR1) data compared to the expected event rate from the background model. Image from [A$^+$22a].

3.4.1 Material Radioactivity and Davis Cavern Walls

All materials contain traces of long lived radioactive contaminants (mainly from the decay chains of ^{238}U and ^{232}Th), and for that reason all materials used in LZ have very restrict constraints on the maximum radioactive activity allowed [A$^+$20b]. The most notorious sources are the PMTs themselves and their bases, the ICV and OCV (despite of the reduced radioactive content of titanium, their very large mass makes them non negligible). The challenging nature of these background sources stand on the close proximity with the active volume of the detector.

The PMTs chosen for the LZ TPC are low radioactivity, made possible by the combined development done together with the manufacturer [M$^+$17]. The PTFE used in the cryostat and in other internal components may also be a source of neutrons, even though the contamination level is smaller that of the PMTs, it is in direct contact with the LXe, which introduces an NR contamination affecting the WIMP search [M$^+$17]. For the $0\nu\beta\beta$ decay, the ^{214}Bi decay to ^{214}Po and the ^{208}Tl decay to ^{208}Pb (which decay via β emission) could represent a problematic background sources, as these gamma lines (with a probability of 2.76% and 35.93% of occurring, respectively) may be not identifiable by the β coincidence. This happens because the emitted electron is trapped in the materials and only the gamma-ray is detected.

The rock of the Davis Cavern also contains radioactive contaminants from the ^{238}U and ^{232}Th chains. However these events can be tagged by the Skin and OD anti-coincidence vetoes [A$^+$20b].

3.4.2 Radon Progeny

One of the daughters of ^{222}Rn is the ^{214}Bi which has a 2448 keV gamma line which can be easily tagged by the β coincidence, with a rejection efficiency of at least 99.97% [A$^+$20b]. The problem however, occurs when ^{214}Bi decay via a "naked-β" (no gamma emission because the ^{214}Po goes directly to the ground state) with a branch ratio of 19% [A$^+$20b] but this can also be vetoed by the ^{214}Po α decay due to the 164.3 μs half life. The final rejection of internal ^{214}Bi is more than 99.99% [A$^+$20b].

Another problematic background are the positively charged daughters of the ^{222}Rn which can be captured by the PTFE walls or drift to the cathode where they decay, producing background events which cannot be vetoed using coincidence decay [A$^+$20b].

3.4.3 Cosmogenic Backgrounds

Being located deep underground, the muon flux from the cosmic rays interacting with the atmosphere is reduced by a factor of 3×10^6 compared with the surface flux [M$^+$17]. However, some muons survive and can be detected in the TPC and via Cherenkov radiation in the water tank and/or scintillation light in the GdLS. Neutrons produced via muon-induced electromagnetic and hadronic showers (especially in high-Z materials) may not be easily identified and therefore generate background events. The neutron flux originated through water interactions or the cavern walls is low, where the neutron flux from the rock walls is $0.5 \times 10^{-9}\ n\,cm^{-2}s^{-1}$ and a production rate in water is $10^{-9}\ n\,Kg^{-1}s^{-1}$ [M$^+$17].

Cosmogenic activation of ^{137}Xe, which is produced by the muon-induced neutron interaction with ^{136}Xe, can raise the amount of radioisotopes present in the LXe. The ^{137}Xe decays via naked-β with as branching ratio of 67%. Two sources of γ-rays are ^{46}Sc emitting 889 keV and 1120 keV γ-rays and ^{60}Co (present in copper components) which are produced via neutron capture and produce 1173 keV and 1332 keV γ-rays, respectively [M$^+$17]. Also, xenon can be activated during storage and transport. This results in the presence of ^{127}Xe, ^{129m}Xe and ^{131m}Xe, which cannot be mitigated by self-shielding or purification. Once the xenon is moved underground, these are no longer a concern as the activation is stalled and the radioisotopes decay away.

3.4.4 Xenon Self-Shielding and Fiducialization

The backgrounds from the external sources of the TPC diminish exponentially as we move deeper into the LXe due to the xenon self shielding nature (see Figure 3.7). To take advantage of the self-shielding of LXe, a fiducial volume is selected to optimize the signal to BG ratio, since both for WIMP and $0\nu\beta\beta$ decay searches the signal is expected to be uniformly distributed in the full active volume of the LXe.

The LZ fiducial volume for the SR1 is defined as the region starting 12.8 cm above the cathode up to 2.2 cm below the gate grid, expanding radially from the center until 4 cm from the PTFE field cage. This volumes encloses 5,2 tonnes of xenon [A$^+$22b]. The fiducial volume was projected to contain 5.6 tonne of LXe with an estimated background count (NR + ER) from 1000 live days of 6.38, after ER discrimination and NR efficiency being taken into account [M$^+$17].

The lateral limit is defined thanks to the neutron tagging efficiency of the Skin, which helps the present level of reduction required closer to the levels for γ-rays (about 2 cm), otherwise a limit of 6 cm would have been necessary for the fiducial radial limit. However, due to the poorer xy-plane spacial resolution of S2s near the TPC wall, the fiducial volume radius has to

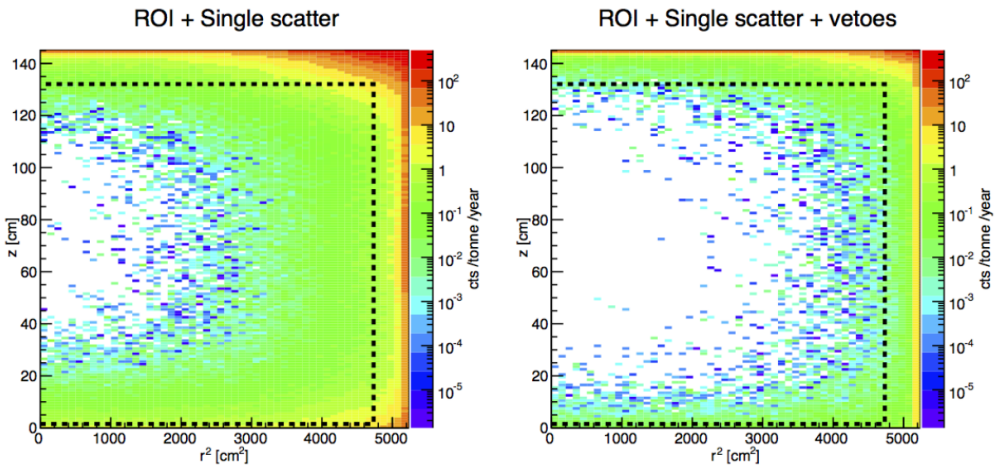

Figure 3.7: Single scatter events in the region of interest (ROI) of WIMP search from total NR background and ER leakage (99.5% discrimination efficiency). On the *right* is clear to note that the anti-coincidence veto has a great impact on the rejection efficiency, comparing with the image on the *left* where no vetoing was made. The dashed line represents the fiducial volume, which encloses 5.6 tonnes of LXe. Image from [M$^+$17].

be reduced as to prevent background "leakage" from this events. For the vertical limits, only the shelf shielding of xenon has to be considered. Thus, the bottom fiducial limit is much closer to the lower limit of the drift region (compared with the upper fiducial limit distance from the top of the drift region) since it has a bigger layer of LXe (about 14 cm), corresponding to the reverse field region. For $0\nu\beta\beta$ decay is also defined a fiducial volume containing about 967 kg of LXe, being defined as being between 26 and 96 cm from the cathode with a radius of 39 cm [A$^+$20b]. This volume was optimized using a cut-and-count analysis and is shown in Figure 3.8. This volume is much smaller than the fiducial volume for WIMP search due to the high penetration potential of γ-rays.

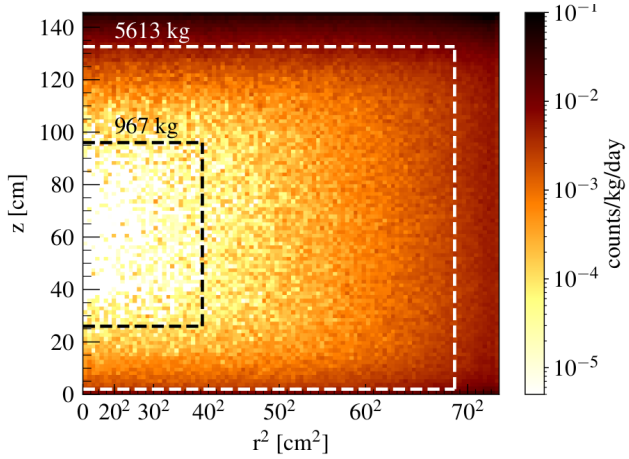

Figure 3.8: Background event rate of ERs in the active region as a function of the TPC height (z) and squared radius (r^2). The dashed white line represents the projected fiducial volume for WIMP search and the black dashed line represents the fidutial volume for $0\nu\beta\beta$ decay searches. Image from [A$^+$20b]

3.5 Simulations

Background simulations are an integral part of an experiment, giving information about the expected BGs and estimation of the rejection efficiency of the BG mitigation techniques. These simulations thus need a good understanding of all radioactive sources (internal and external to the detector) present and an accurate description of the detector layout [M$^+$17]. These simulations gave good estimates as can be seen in Figure 3.9 in comparison with the SR1 data.

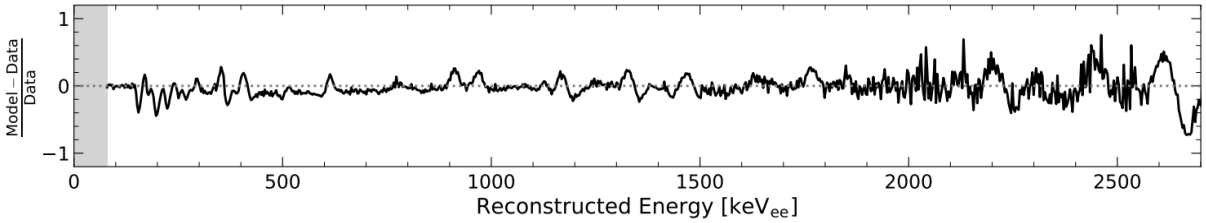

Figure 3.9: Relative difference of background counts between the background model and the SR1 data as a function of the energy. The energy range is the same as in Figure 3.6. Image from [A$^+$22a].

In the particular case of LZ, all possible contamination sources described previously are taken into account, being normalized a posteriori for each component and source. Together with background events, also calibration sources are simulated. The software used was BACCARAT, which is an in-house software, tracks particles using the underlying GEANT4 famework [A$^+$21d].

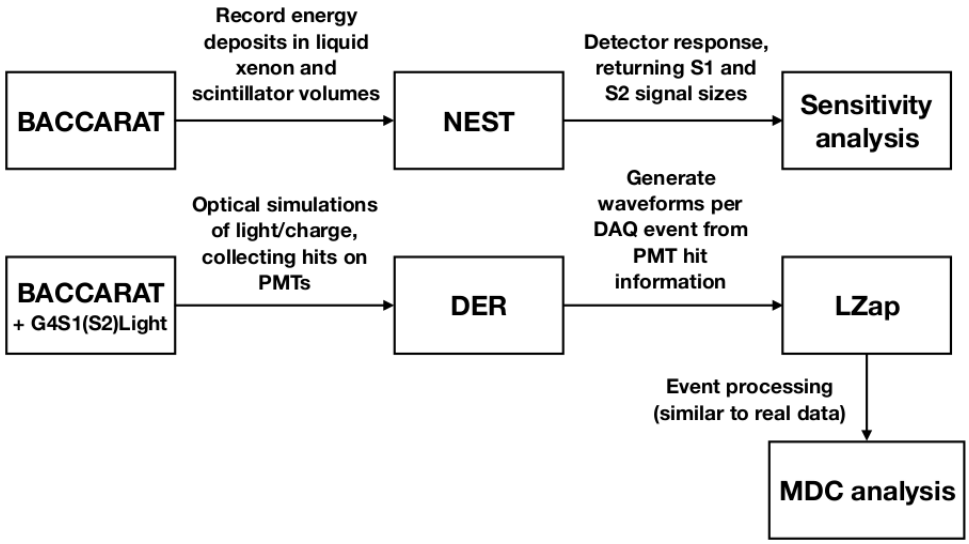

Figure 3.10: Simulation chains used by the LZ collaboration to generate data for sensitivity analyses. Image from [A$^+$21d].

LZ simulations have two chains for different purposes, output and utility (see Figure 3.10). The first fast chain enables large data sets to be generated as it only records the energy deposited, generating both S1 and S2 signals using Noble Element Simulation Technique (NEST) [A$^+$21d]. The large data samples generated can be used to estimate BG rates and the sensitivity of the detector. The second chain is a much more detailed description of an event, as the ionization electrons and the VUV photons interactions on xenon and the scintillation light produced in

the GdLS are simulated. These light collection interactions were not well-modelled in GEANT4 [A$^+$21d], so BACCARAT had to be updated with the required models to get an accurate view of the events in the detector. NEST simulates all the interactions that may occur within the xenon volume, taking into account several conditions of the xenon and interaction, returning the modeling of the time dependent S1 and S2 shape profiles. After BACCARAT+G4S1(S2)Light generate the PMTs counts and times, these are translated into waveforms by the Detector Electronics Response (DER), which simulates the various electronic stages. Finally, the data simulated is passed through the LZ analysis framework, performing pulse and event reconstruction setting the data in a format similar to the real data.

3.6 Calibrations

To fully understand the response of the various detectors in the LZ experiment, a wide range calibration strategy was developed, where different types of radioactive sources are used throughout the detector. These sources are deployed separately to study particular and relevant interactions similar to those LZ intends to search or reject. There are 4 deployment strategies:

- Internal Source Delivery which consists of the introduction of a source mixed into the LXe (ER response only);
- External Source Delivery where the source is placed in one of 3 equally spaced spots between the ICV and the OCV with adjustable heights, called Calibration Source Delivery (CSD) (gamma sources to the ER response and neutron sources for NR).
- Photoneutron Source Delivery that is located on the top of the cryostat in the place of the top acrylic plug (see Figure 3.5) (NR response only);
- Deuterium-Deuterium Neutron Source to calibrate nuclear recoils (NR response only).

3.6.1 Internal Source Delivery

LZ uses 4 gaseous radioisotopes which are mixed with the LXe to make low energy ER calibrations, as the self shielding of xenon prevents the use of external low energy sources [M$^+$17]. These radioactive sources have unique properties which make each one of them suitable for distinct tasks. For spatially-varying efficiency effects calibration ^{83m}Kr is used because it has a mono-energetic peak at $Q = 41$ keV with an half life of $T_{1/2} = 1.8$ hours (a low half life means that there are no long lasting effects of the calibration, therefore not influencing the sensitivity of future data).

To calibrate, for example, the pulse width over the drift time the used isotope is ^{131m}Xe, since it has a longer half life of $T^{1/2} = 11$ days, allowing a greater homogeneity inside the LXe. The deployment system is very much the same one as for ^{83m}Kr, but now using ^{131}I, having a probability of 0.39% of transitioning to ^{131m}Xe. The calibration signature is a mono-energetic

peak at $Q = 164$ keV, having also the capacity of being used in the calibration of the Skin region.

Finally for very low energy ERs, Tritium-labelled Methane (CH_3T) is used, since the Tritium decay emits β-electrons with an energy endpoint of $Q = 18.6$ keV. The longer half-life of Tritium ($T_{1/2} = 12.3$ years) will contribute for the background after the calibration. This means that it has to be removed, which is achieved with the LZ getter (xenon circulation system) with a good efficiency, method demonstrated by the LUX experiment, with characteristic half lives of the order of a couple of days [M$^+$17].

3.6.2 External Source Delivery

The Calibration Source Deployment (CSD) system consists on a stepper motor to move 3 nylon filaments, which hold the calibration sources. These are capable of placing a source as high as the top of the water tank and down beyond the cathode level, covering the 6 m lenght of the calibration tubes [M$^+$17].

For the NR calibrations, 2 neutron sources are used the CSD: $AmBe$ and $AmLi$, which consist on a source of α-particles (Am) that interacts with a light target emitting a neutron, known as an (α, n) reaction. For $AmBe$ the emitted neutron can reach an energy up to 11 MeV and for up to 1,5 MeV for the $AmLi$ source. The advantage of using $AmLi$ over $AmBe$ stands on the fact that the maximum energy transferred to the recoil nucleus (40 keV) is much lower and closer to the range of energies expected for NRs of lighter WIMPs.

Gamma sources are also deployed in the CSD and used to calibrate all three detectors of LZ (TPC, Skin and OD). The use of ^{22}Na as a timing synchronicity calibration is fundamental, since it produces two back to back 511 keV gammas. These two gammas can be then detected simultaneously in the OD, Skin and the TPC to possibly detect any timing difference.

3.6.3 Photoneutron Source Deployment

Photoneutron Sources exploit (γ,n) reactions on nuclei to produce neutrons. In LZ, these sources are deployed on the top of the OCV in the middle of the top acrylic vessels.

The photoneutron sources deployed are $^{205}BiBe$ and ^{88}YBe, which produce neutrons with discrete energy of 88.5 keV and 152 keV, which are capable of inducing NRs with endpoints of 2.7 keV and 4.6 keV, respectively. The S1 versus S2 spectra for these events are similar to the spectra from coherent nucleus scattering ^8B solar neutrinos, that pose a potential BG for WIMP research for the light mass regime [M$^+$17].

3.6.4 Deuterium-Deuterium Neutron Source

A deuterium-deuterium (DD) neutron source is deployed outside the water tank and the conduits seen in Figure 3.1 labelled with the number 6 are used to create a collimated beam of neutrons. The DD neutron source is shown in Figure 3.1 (labeled with the number 6) for nuclear recoil calibrations. This source exploits the fusion of two deuterium atoms from which are produced one ^3He atom and one neutron. The neutrons produced are mono-energetic with an energy of 2.45 MeV and the flux can be set between 4×10^6 and 10^9. These neutrons can be converted into a quasi-mono-energetic neutron beam with 274 keV of minimum energy by the usage of a Deuterium-based Neutron reflector to direct the neutrons to the conduit. To prevent that high energy neutrons coming directly from the DD source mix with the reflected neutrons, the source is shifted from the conduit opening. To study the 2.45 MeV neutrons, a narrower conduit is used to ensure that the beam is highly collimated. For this setup, the DD source is in front of the narrower conduit.

3.7 Next Generation Detectors

A next generation low background xenon detector is already being planned, also known as G3 detector. This is the objective of the XLZD consortium, which is composed by the LUX-ZEPLIN, Darwin and XENONnT collaborations, with the intent of building a xenon dual-phase TPC detector with up to 100 tonnes of xenon. Despite this increase of the order of $\times 10$ in detector mass, the cylindrical geometry results in only a factor of $\times 2$ increase in detector dimensions (approximately 3 meters both in height and diameter) [A$^+$22c], corresponding to about 2000 μs of drift time assuming the drift velocity of LZ.

The main goal of this detector is to explore the remaining WIMP parameter space down to the so-called "neutrino fog" [A$^+$22e]. But given its size and extremely low background (achieved thanks to xenon self-shielding and veto systems similar to the LZ Skin and OD), the XLZD detector can also be very competitive in other rare searches, in particular 0vbb decay in ^{136}Xe [A$^+$22c].

Chapter 4

LZap Framework and Pulse Discrimination Algorithm

An indispensable component of any experiment is the processing and interpretation of the raw data acquired. Therefore, a data analysis framework must be implemented, aimed to characterize different particle interactions given their distinct event signatures. To achieve this, several computational algorithms are deployed in order to process the raw data and extract useful information in the form of reduced quantities (RQs). In the case of LZ, this tool is particularly important since it is a rare event experiment, where the distinguishability between events of interest and the dominant background has a direct impact on its scientific performance.

As of July 2022, LZ is the most sensitive dark matter experiment looking for WIMP dark matter. Besides that, it is also sensitive to a wide range of physical processes at several energy ranges, such as the double electron capture on ^{124}Xe or the neutrinoless double beta decay of ^{136}Xe. The data acquisition (DAQ) system records the response of each individual PMT channel present either in the TPC, Skin or OD within a time window typically on the range of 5 ms, provided that the PMT readout exceeds a certain voltage threshold. To allow a wide range of energy events to be studied, the PMT signals for the TPC and OD are recorded in two separate gain stages: high-gain (HG) and low-gain (LG) for low and high energy ranges, respectively, being separated by an order of magnitude. The timeline is defined as the raw data, which is the input of the analysis framework. Together with the raw data, additional information, such as the field strength, PMT gains, light collection maps, just to name a few, is stored and accessed by the analysis framework to further complement the state of the detector during the data acquisition. The amount of information gathered by LZ is enormous (on the order of Petabytes per year), so the analysis framework needs as much speed as efficiency, since it has to be able to return usable information in a reasonable time scale.

This chapter is divided in three sections, where in section 4.1 it will be discussed the analysis framework of LZ (named LZ analysis programme or LZap), in more detail, followed by the tools used to generate mock data on the form of S2 like waveforms (section 4.2) and the algorithm developed during this work to analyse such waveforms (section 4.3), which is the work presented in this thesis.

4.1 LZap Framework

LZap is built using the GAUDI framework, which was developed by the LHCb Collaboration to facilitate the development of data processing applications for high energy physics [A^+21d]. It follows an architecture-centric approach to construct a resilient software framework able to withstand long lasting experiments, where the requirements and technology changes are expected to occur. This approach uses algorithm objects (modules) that can be initiated and run in a set sequence, known as processing chain, over data objects. These modules, as intended, can be updated or created by collaborators to keep LZap always updated.

The LZap structure is segmented by detector and gain, meaning that 5 substructures arise: TPC high gain (TPC-HG), TPC low gain (TPC-LG), Skin, OD high gain (OD-HG) and OD low gain (OD-LG), where the RQs for each of the physical detectors are contained. The TPC-HG and TPC-LG structures are also afterwards merged into a "mixed" gain structure, where the saturation of the high gain data is taken into account by selecting the corresponding low gain data, together with pulse shaping corrections to adjust for the two different electronic samplings.

The readout of the PMTs is not continuous, in fact, for each triggered event, the waveforms have a digitization rate of 100 million samples per second (10 ns sample size). The data is only recorded for each individual PMT readout that meets a certain voltage response threshold , called pulse-only digitization (POD). The sum of all triggered PODs according to the correct acquisition time gives the raw waveform of the event. Multiple structures (pulses) can be found in a POD, which may indicate distinct physical processes within the same event. These structures can be distinguishable and their boundaries identified by LZap.

4.1.1 Photon Detection Processing Chain

The Photon Detection processing chain is responsible for the pulse-level processing. The modules within this chain identify, parameterize and classify the individual pulses generated by the detector. This processing chain starts with the PodCalibrator module, which converts the raw waveforms from ADC counts to photons detected (phd) units. This modules returns a CalibratedEvent data object, on which the single photon electron gain is scaled to 1 phd for all detectors.

After, the *PodSummer* returns the sum of all the PODs into a single waveform and the start and end times of the each individual pulse are identified by the *DoGPulseFinder*. The pulse parameters (RQs) are calculated by the *ChannelPulseParametrizer* and *PulseParametrizer* which

feed the *PulseClassifierHADES* to classify the event into six possible classifications: Primary Scintillation (S1); Electroluminescence (S2); Single Electron (SE); Multiple Photon Electron (MPE); an Undetermined (Other). For the OD events a similar data processing structure also exists.

4.1.2 Interaction Detection Processing Chain

The Interaction Detection processing chain is responsible for the event level processing. Using the information collected by the Photon Detection processing chain, it characterizes the event by pairing the S1 and S2 pulses to reconstruct its vertices and classifying each event into Single Scatter (SS), Multiple Scatter (MS), Pileup event (pileup), Krypton event (Kr) or "other" if the event does not fit in the criteria of any other category. This is done by the *Interaction Finder* module. Using RQs from two modules of the TPC-HG and TPC-LG detectors, the *xy* position reconstruction of an interaction is done by the *S2PositionReconstructionMercury* module, resorting to the light pattern created by an S2 type signal and using the light response functions (LRFs) of the PMTs in the top array.

Several other modules applied to each event in this chain. These include the *XYZPositionCorrector* and *PulseAreaCorrector* to execute corrections, the *VetoInteractionFinder* to find coincidences between the Skin and the TPC for veto possible events which may lead to increased background and the *EnergyReconstructor* which reconstruct the event energy.

4.2 S2 Pulse Generator

To generate mock data for testing the algorithm developed during this work, a simple S2 pulse generator (*S2Generator*) was used, taking the detector condition from Science Run 1 (SR1) of LZ as a reference. The sample time is set at 10 ns, which corresponds to the 100 MHz acquisition rate of LZ. The *Single Electron* (SE) size, which is the median number of photons detected for each electron extracted into the gas phase and its respective uncertainty due to statistical fluctuations. The drift velocity of the electrons given by the electrical field of 193 V/cm in the LXe [A^+22b] and the parameterization of the FWHM of S2 pulses over the drift time, using data from the decay of Xe^{131m} (see Figure 4.1). This decay was used because it is characterized by a mono-energetic SS events of low energy (164 keV), which produces non-saturated waveforms and a low probability of photoionization of impurities and of the grids. From this decay it is also possible to determine the diffusion coefficients using the Equation 3.10. As Equation 3.10 shows, the time at which the electrons are extracted is not the same, following in fact a normal distribution, with the mean of photon times corresponding to the mean of the peak and its standard deviation is dependent on diffusion coefficient and the drift time [Sor11].

The waveform generation itself can be dived into two parts: a Gaussian component resulting of the diffusion effect on the electron cloud, and the characteristic tail that is prevalent in pulses from high energy events. Figure 4.2a shows the effect of the tail in a SS pulse. The tail shape

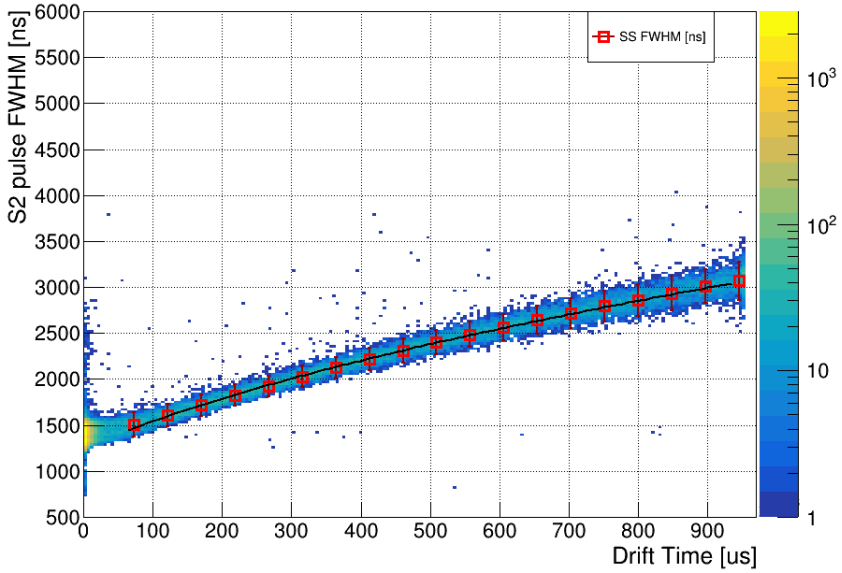

Figure 4.1: 2D histogram of the distribution of the FWHM of LZap SS S2 pulses over the entire LZ drift time of SS events from the Xe^{131m} decay with 164 keV, where the red squares represent the means of the pulse width distribution of the slices of drift time. The black curve is the fit to the means according to Equation 3.10. This population is considered to have well behaved S2 pulses due to its low energy where some effects such as charge trapping or light ionization are not as prevalent.

is given by a *Gamma* distribution, which is an approximation of the exponential distribution of the delayed emission of SEs (detailed explanation below) taking also into account the normal distribution of the S2 electron cloud [SK18]. For the Gaussian component, the *S2Generator* first calculates the number of expected electrons based on the desired S2 area, taking into account the average SE size in number of photon detected (phd), being a fraction of photons produced which are dependent on the extraction field as seen in Figure 4.3. The waveform of each SE is computed as a semi-uniform distribution of photon times, with characteristic length dictated by known values of extraction field and width of the gas gap [M$^+$17]. Secondly, the generator samples the SE extraction times and combines the photon detection times. These extraction times follow a normal distribution dictated by the shape of the electron cloud, as explained previously. The average number of photons detected per electron extracted (SE size) of the *S2Generator* is set at 52.8 ± 10.8 photons detected (fitted to experimental data from SR1) and these photons also have different arrival times within a time window defined by the extraction field strength [M$^+$17]. All photons are summed with their respective detection times to generate the Gaussian distribution of the S2 signal.

Each waveform generated is composed of two S2s that are merged to produce the final waveform. The separation in time between these two S2 pulses is a key parameter that will be used to study and develop the algorithm presented in section 4.3. A null separation represents the case of an SS interaction. The two S2 pulses can have different areas, an the area asymmetry is defined as the difference between the two pulse areas divided by the total area of the waveform (see Figure 4.2b), which was implemented to prevent the creation of a bias on the SS/MS discrimination algorithm.

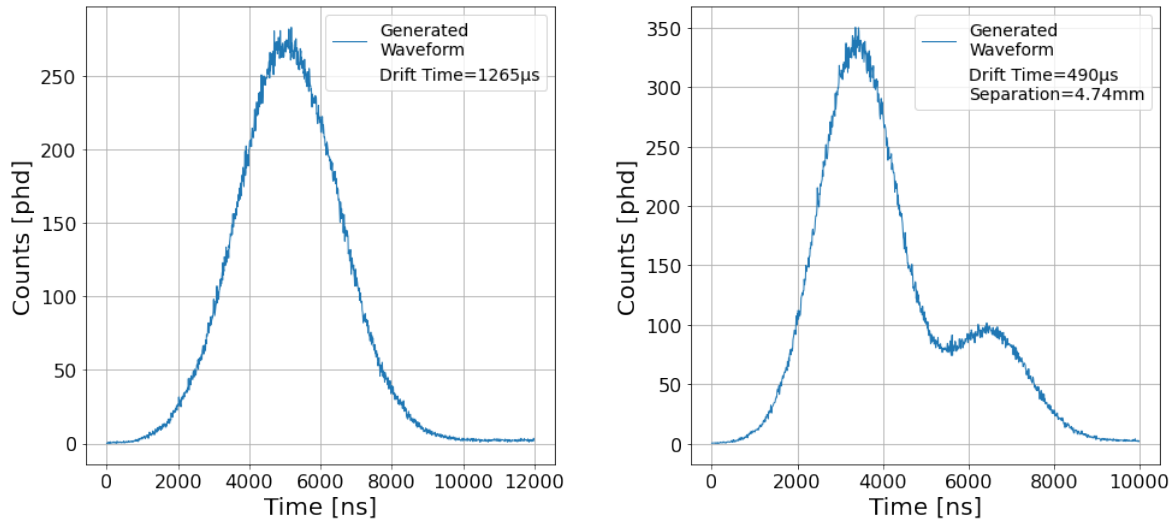

(a) SS S2 signal

(b) MS S2 signal

Figure 4.2: Examples of two pulses generated using the *S2Generator*. On both pulses the tail can be observed by the small elevation over the baseline after the main pulse. The SS S2 signal was generated by the sum of two pulses with zero separation. The MS pulse shows an example of asymmetry on the pulse areas.

The S2 tail is an effect that is more prevalent in high energy events, but its presence is inherent to all events energies. The difference stands on the fact that for high energies, the emitted photons form a continuous distribution which cannot be separated from the S2 pulse, while for low energy events the rate of photon emission is much lower and therefore a discrete distribution of SEs occurs that can be more easily discriminated in relation to the main S2 pulse. This phenomenon is caused by three effects: delayed emission of trapped SEs, ionization of impurities in LXe and photoionization of the grids. The delayed emission is caused by the trapping of electrons on liquid-gas inter-phase. By the thermo-electron emission model, only the electrons with an orthogonal (to the liquid-gas inter-phase) projection of the linear momentum higher than the electrical threshold can be emitted. The emission time is given by an exponential decay law with characteristic times from μs up to ms [Bol99]. The ionization of impurities occurs when photons from the main S2 signal extract additional electrons that will drift and reach the gas phase and cause further VUV photon emission. As the impurities are evenly distributed in the LXe, the arrival times to the xenon liquid-gas inter-phase will have a maximum time window corresponding to the entire length of the TPC (approximately 950 μs). The photoionization of the grids occurs when photons from the main S2 pulse produce photoelectric effect in the metallic grids. This phenomenon is characterized by a pulse like structure at the end of the S2 signal for the photo ionization in the gate grid [B^+21], being more noticeable for pulses near the top of the grid. This effect also happens for the cathode, but since the electrons are delayed by the drift time of the TPC [B^+21], it is not relevant for this study.

Only the first two effects were considered in the *S2Generator* used in this work, and represent up to 5% of the total area of the progenitor S2 pulse. This value overestimates this effect in relation to the tails observed in SR1 data. The low tail contribution for the total pulse area in

SR1 S2 signals is indicative of the high electrical field and high levels of xenon purity [A$^+$22b].

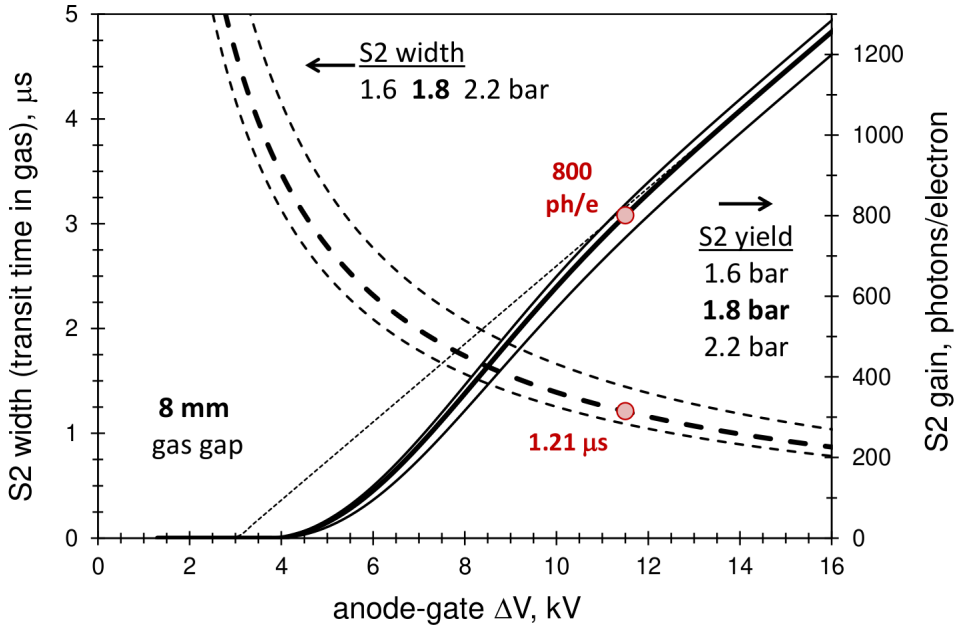

Figure 4.3: Dependency of the photon yield (S2 gain) and the mean of the pulse width (S2 width) ignoring the longitudinal diffusion on the voltage between the anode and the gate. The red circles correspond to the expected levels of S2 photon yield and mean width for the expected field that was projected for LZ in [M$^+$17] from which this plot was taken from. For SR1 the ΔV are not the same, as well the models which have some deviations from the model shown in the figure.

4.3 SS/MS Discrimination Algorithm

The sensitivity for the half life time of the neutrinoless double beta decay in ^{136}Xe is highly dependent on the ability to vertically separate S2 pulses [A$^+$20b], and has a maximum at 1.5 mm of separation as seen in Figure 4.4. The sensitivity study for the LZ experiment assumes this to be 3 mm, but LZap in its current version only reaches 3.7 mm for small S2 asymmetries. In order to maximize the sensitivity of the experiment a new tool must be developed. The objective of the algorithm developed for this thesis is the reduction of the minimum separation to which two S2 pulses can be discriminated. It was developed using *Python3* and it does a regression for two different models to S2 pulses, which are compared to discriminate between single and multiple scatter. The function used was *curve_fit* from the *Scipy.optimize* library, which uses a non linear squares (NLS) regression model [com].

Every model has three main constituents: the observable (y), the signal model ($f(\vec{x};\vec{\beta})$) and the random fluctuations (ϵ). The general form of a model can therefore be represented by

$$y = f(\vec{x};\vec{\beta}) + \epsilon \tag{4.1}$$

The observable is the data to which it is intended to fit the signal model that contains the data

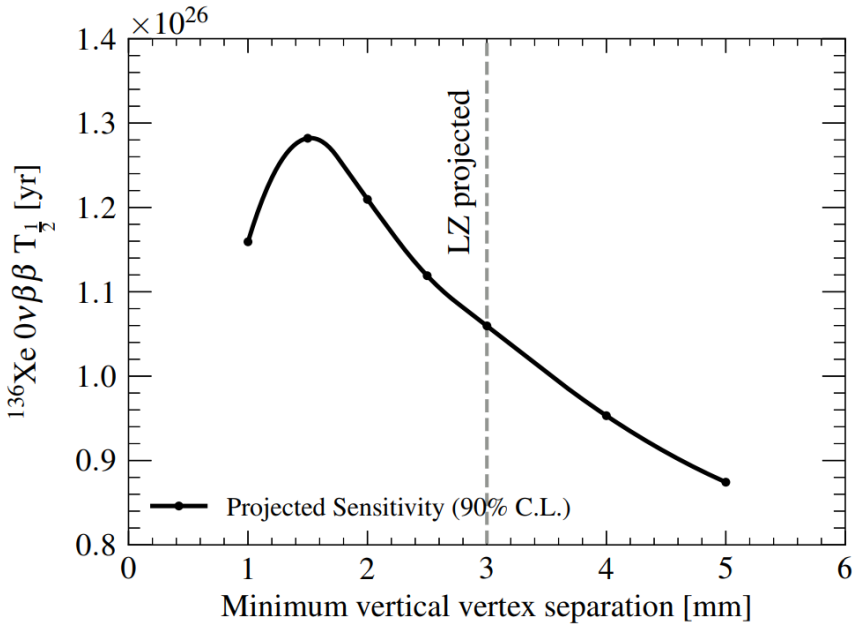

Figure 4.4: Neutrinoless Double Beta decay half life time sensitivity for ^{136}Xe (90% Confidence Level) dependence with the minimum vertical separation. The dashed line represents the assumed separation for the LZ experiment. Image from [A^{+}20b].

variables ($\vec{x}$) and the parameters ($\vec{\beta}$) to be fitted that can be arranged between them to form the model for the regression. In this work three models will be in use:

$$f_1(t_d; p_0, p_1) = \sqrt{p_1 \cdot t_d + p_0} \tag{4.2}$$

$$f_2(x; \bar{x}, \sigma, A) = A \cdot \exp\left\{-\frac{(x-\bar{x})^2}{2\sigma^2}\right\} \tag{4.3}$$

$$f_3(x; \bar{x_1}, \bar{x_2}, \sigma, A_1, A_2) = A_1 \cdot \exp\left\{-\frac{(x-\bar{x_1})^2}{2\sigma^2}\right\} + A_2 \cdot \exp\left\{-\frac{(x-\bar{x_2})^2}{2\sigma^2}\right\} \tag{4.4}$$

The first one is only used to calibrate the algorithm and the last two are used to perform the regression over the waveforms. On all models there is only one predictable variable denominated as x. The usage of these three models in specific have different justifications, as in the case of the model given by Equation 4.2 it follows the expression for the electron cloud diffusion over the drift time (Equation 3.10) and the models given by Equation 4.3 and 4.4 are the related to the normal distribution of the S2 light [Sor11]. The NLS regression is an extension on the Linear Squares (LS) regression, but is conceptually the same, in which the parameters are the numerical values that minimize the sum of the squared deviations between the response variables and the mathematical function of the model. Mathematically, this can be expressed by [Lu21]

$$Q_{min} = \min\left\{\sum_{i=1}^{N}[y_i - f(\vec{x_i}; \vec{\beta})]^2\right\} \tag{4.5}$$

where N is the total number of data points of the pulse.

The NLS regression has several advantages such as: the wide range of functions that can be fitted; the good estimates of the unknown parameters (even for relatively small datasets); and because it is a well known and developed method, it can provide with good confidence intervals predictions on the regression parameters according to the data and therefore be used for precise analysis and calibrations. However, when moving from linear to non linear processes, the use of iterative optimization processes to compute the parameters estimations becomes necessary. This means that the algorithm needs initial values for its parameters before beginning the optimization, with the additional constraint that they need to be reasonably close to the correct values for the parameters fits, since the optimization may diverge completely or converge for a local minimum. Being related with the LS regression, it shares some of its disadvantages, such as sensitivity to outliers that may affect the final values of the parameters. This is accentuated in the non linear case where fewer model validation tools exist for the detection of outliers [NIS].

On Figure 4.5 a graphical representation of the algorithm that is now going to be discussed in detail is shown. The waveforms and their known parameters (for real LZ data these are drift time and area of the pulse and for generated data are also included real separation and asymmetry) are in two different files, so the first step is to load both files into memory. After the loading process is completed, a cycle is done over all waveforms as the following steps have to be executed taking into account each individual waveform. The first step is setting limits to which data points of the waveform will be used to perform the regressions to the two different signal models described by Equations 4.3 and 4.4, which from now on will be respectively referred as *Gaussian* and *Bimodal* fit. This is done by establishing an amplitude threshold which is defined as $1/30$ of the waveform maximum. The value was chosen in order to include the maximum data points to ensure that the regression has enough statistical data and at the same time that it is above the tail baseline (see Figure 4.2 from section 4.2), as it does not contribute for the overall shape of the pulse. This value can be adjusted according to the S2 tail baseline of the dataset to be analysed. A fortunate and intentional consequence of this step is the optimization of the regression run time, as the number of degrees of freedom is vastly reduced.

The next step is setting the initialization values of the parameters for the *Gaussian* fit, as the NLS regression imposes it since it uses iterative procedures, with the additional condition that they are good estimations of the real values. Otherwise, the regression may diverge completely or converge to a local minimum different from the true global one [NIS]. For this model, the initial values are set at the mean point of the limits set by the amplitude threshold discussed before, the mean between the highest and lowest widths of SS pulses (which can differ for different ranges of drift time) as observed in the data being analysed (sigma) and the maximum amplitude of the waveform (amplitude). To ensure that there are no divergences, parameters boundaries were also implemented. For the mean and width, these are the limits from which the initialization parameters values were obtained and for the amplitude boundaries these are set at 50 and 110% of the maximum amplitude of the waveform. The boundaries for this model regression are made for maximum fit freedom without obtaining nonsensical parameters values. Finally the *Gaussian* fit is done and the three parameters obtained are stored.

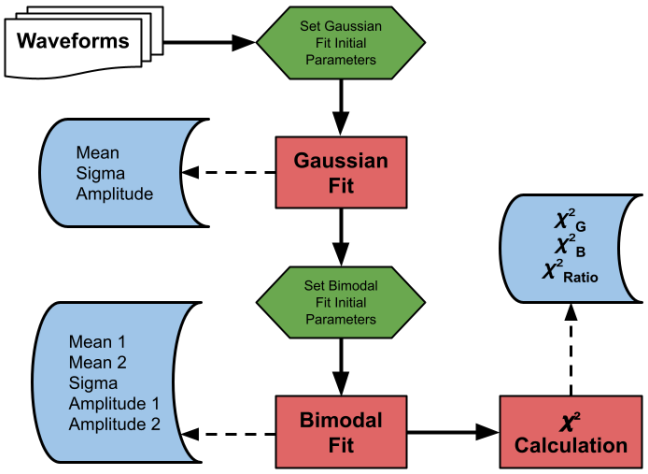

Figure 4.5: Flow chart of the Discrimination Algorithm. The green hexagons represent the preparation steps before the fits, the red rectangles represent the execution of a computational process and the blue boxes are the data stored for the analysis.

For the *Bimodal* Fit the procedure is similar, with the difference standing on the more stringent boundaries to the model parameters. This model has only two additional parameters, the mean and amplitude of a second Gaussian distribution, as the sigma was set to be exactly the same for both pulses. This choice falls on the reasoning that if two pulses are merged, the width variance arising from the two different pulse drift times, can be approximated to be zero. The initialization value for the two means are chosen to be at 45% and 55% of the limits set by the amplitude threshold, instead of being both on the median point (as the mean for the *Gaussian* fit) to avoid a bias towards pulse reconstructions for zero separation. The opposite argument is made for the initialization values near the extremes. Several different combinations were tested and the values chosen were considered to be as unbiased as possible. The boundaries remain the same as for the *Gaussian* fit. The width initialization value over the drift time is given by a parameterization and the boundaries are a very reduced offset either for higher or lower values from that same starting point. To conclude the setup, the amplitude initialization values and boundaries are set at 15%, 110% and 50% of the maximum amplitude of the waveform, respectively. The 15% lower boundary for the amplitude is chosen to be the minimum amplitude from which a pulse can be reconstructed with high level of confidence. Smaller structures could be reconstructed but their physical meaning would not be significant, as it would be within the range of statistical uncertainty. Finally, the *Bimodal* fit is calculated and the five parameters are stored.

With both regressions done, the final step is to calculate the goodness of the fit for both models, for which were considered the same data points used for the regressions. This ensures that the tail baselines do not inflate the χ^2.

Chapter 5

Performance of the Discrimination Algorithm

The objective of this work was to build a tool to discriminate *Single Scatter* (SS) and *Multiple Scatter* (MS) pulses to increase the sensitivity of the LZ experiment, with the focus on the $0\nu\beta\beta$ decay of ^{136}Xe. This chapter will focus on the performance of the algorithm described in the previous chapter.

The vertical separation (Δz), which is defined as a time difference, can be expressed as a distance by multiplying the pulses time difference with the constant drift velocity. Even though LZap has the ability to distinguish close S2 pulses, it is limited by design in distinguish merged S2 pulses, because the *DoGPulseFinder* module is not tuned to do so. Since there is no trivial way of splitting the waveform such that the individual S2 areas are conserved and well reconstructed, this reconstruction must be performed in post-processing (this work). Because of this, a significant fraction of MS pulses will be wrongfully identified as SS by LZap, especially pulses with large area asymmetry. For the present framework of LZ were determined minimum separations for which it could separate (minimal vertical vertex separation) efficiently, assuming different scenarios. This sets the bar for this work at 3.7 mm for pulses with maximum area asymmetry of 0.33 (corresponding to the smaller pulse being 50% of the largest) and 4.4 mm for all pulse asymmetries, within the high energy region which includes the ^{136}Xe $0\nu\beta\beta$ decay.

As was explained in Section 3.3 the width of S2 pulses is drift time dependent and given as an approximation by Equation 3.10. A useful metric used to describe the pulse width is to define it as the full width at half maximum (FWHM). The reason to define it this way, and not between the pulse start and end times, is due to possible artifacts present either at the beginning or at the end of the pulse that would lead to nonsensical pulse widths. This is a reasonable approximation, since the ditched tails do not contribute considerably for the overall Gaussian

shape of the pulse.

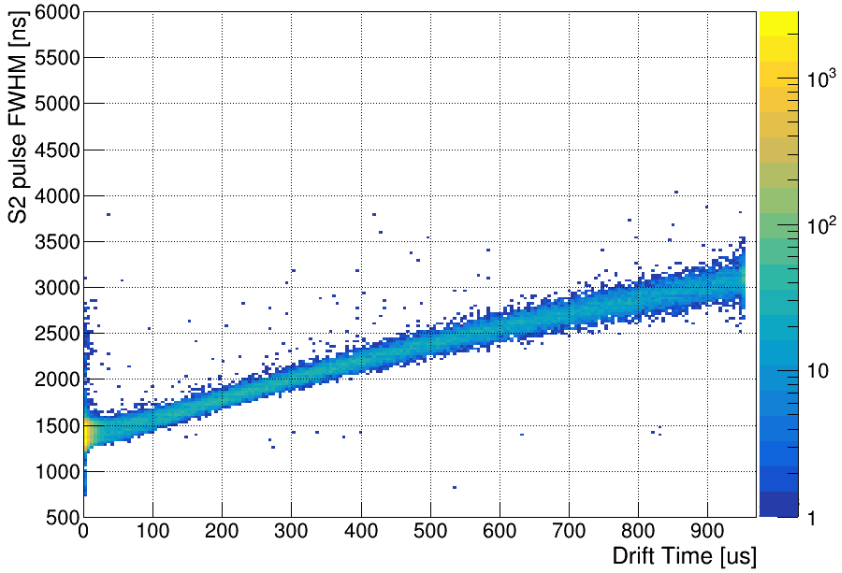

Figure 5.1: 2D histogram of the distribution of the FWHM of LZap SS S2 pulses over the entire LZ drift time of SS events from the Xe^{131m} decay with 164 keV. This population is considered to have well behaved S2 pulses due to its low energy where some effects such as charge trapping or light ionization are not as prevalent.

This Chapter is subdivided in three main sections where first the tools to analyse the performance of the algorithm are discussed and then the last two are directed to the presentation of the analysis results for the mock and the LZ experimental data.

5.1 Analysis of Generated Data

Before this tool can be used, it is necessary calibrate the algorithm. This step is done by parameterizing the pulse width over the drift time, since the algorithm needs to have a small band of widths on which it has freedom to execute the fits, as this minimizes the convergence of the regression to local minimums which is not a desirable effect. This calibration follows Equation 3.10, taking the form of Equation 4.2:

$$Width = \sqrt{p_0 + p_1 \times t_d} \tag{5.1}$$

where p_0 and p_1 represent σ_0^2 and ${}^{2D_L}/_{v_d^2}$,respectively, and t_d the drift time. It is also possible to describe this dependence in units of length but some changes in the longitudinal diffusion equation (Equation 3.10) need to be made using the relation given by Equation 3.9. In the next sections, a deeper look is taken for the parameterization due to the inherent differences between generated and real data.

Before taking a close look to the analysis, it is important to consider some aspects of the generated data. As it was discussed in section 4.3, the *S2Generator* creates S2 pulses similar

to those present in real LZ data, but in reality some second order effects that occur in the light detection processes are not considered in this generator. This will result in more favourable results than it would have been expected for real data. Nevertheless, this data is a valid proxy to real data and was a crucial tool to develop and understand the behavior of the algorithm. The interval of drift time used for this analysis includes depths up to 3 meters (~2000 μs) that are not present in the LZ experiment. Even though this work has as its main focus the previous mentioned experiment, it is also involved with the XLZD Consortium which has the objective to develop and construct a larger third generation (G3) LXe detector, where the tools presented here may be utilised (see section 3.7).

The first step of the analysis of the generated data is to perform a pulse width calibration as a function of drift time. This is done to establish the range of widths to which the Bimodal fit deviation parameter σ will be restricted to (see Equation 3.10). In order to achieve this parameterization, *"slices"* of drift time from a dataset of pulses with a separation of zero (SS pulses) are chosen. Then a Gaussian fit is done to retrieve the mean width as seen in the inset of Figure 5.2, which is used as the median width for that specific drift time middle point. This is done for several slices of drift time, especially for events near the top of the detector, as here the variation of the width over the drift time is greater for larger drift times [Sor11]. These Gaussian means are then fitted to a square root model given by Equation 4.2, following the Diffusion equation (Equation 3.10) behavior. The parameterization done for the generated data can be seen in Figure 5.2.

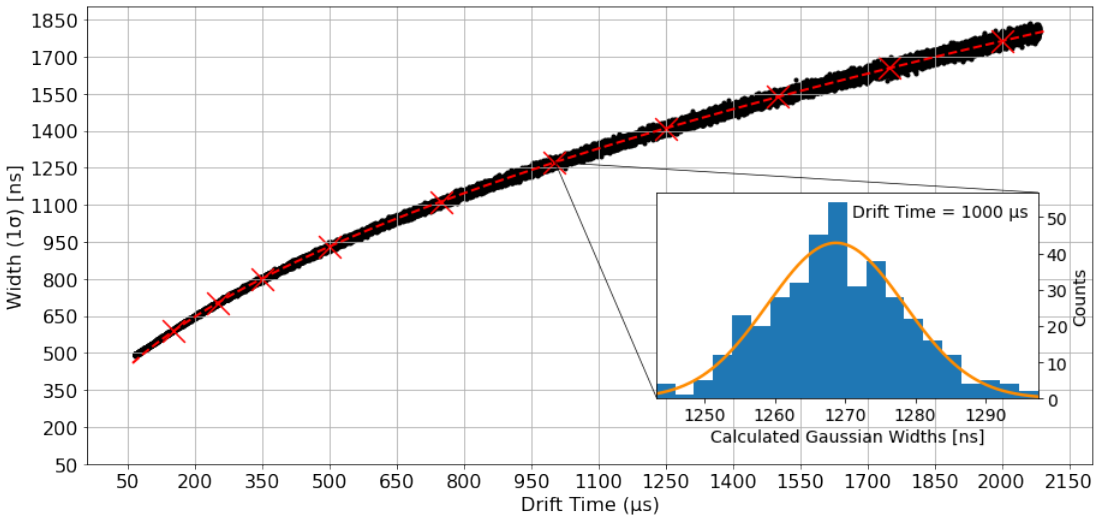

Figure 5.2: Parameterization of the median pulse width as a function of drift time. The fitted parameters correspond to $p_0 = 1206.71 \pm 2.35 \times 10^3\ ns^2$ and $p_1 = 1.4937 \pm 0.0032\ ns$. The smaller plot is a histogram of the calculated widths from the a slice of drift time with the middle point at 1000 μs for SS S2 generated pulses. The orange line is the Gaussian fit obtained from the histogram bin counts.

5.1.1 Measurement of the SS Threshold for Generated S2 Data

Following [K$^+$22] was used a methodology which involves the determination of a threshold by the calculation of a percentile of reconstructed separations from a true SS population. The percentiles used were 90%, 95% and 98%, meaning that 10%, 5% and 2% of the SS signal would be considered MS, respectively. There is a trade-off between higher loss in SS signal i.e. the probability to which a SS pulse is misrepresented as a MS with the higher range of possible separations where MS pulses can be probed. After the determination of a threshold, which is drift time dependent, it is possible to characterize a leakage that is defined as the percentage of reconstructed MS separations which fall below the threshold, providing therefore a quantitative value for the efficiency of the algorithm at separating MS pulses.

With the S2 width parameterization implemented into the algorithm, and using the generated SS (separation of zero) the threshold was determined. Part of the pulses of this population will not have the separation reconstructed at zero as the regression will find strategies to minimize the fit, due to the fact that some of the pulses will be wider (because of statistical fluctuations) than the parameterized width. This leads the algorithm to a local minimum where it will try to separate the two pulses of the Bimodal fit. The reconstructed separations have a typical distribution as seen in Figure 5.3 and from here a threshold, defined as a percentile of separations within a *slice* of drift time, can be determined.

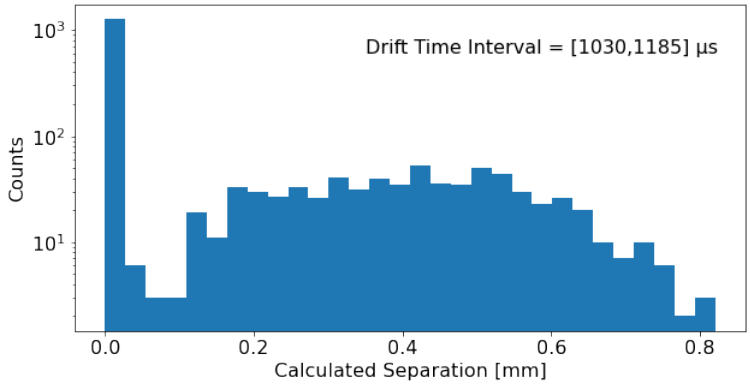

Figure 5.3: Histogram of the distribution of the reconstructed separations of generated SS S2s for the slice of drift time between 1030 and 1185 μs.

Similarly to the width of the pulses, this threshold also has a dependency with the drift time as shown in Figure 5.4 where it is overlaid with the distribution of reconstructed separations as a function of drift time. For the drift time dependence study of the threshold were considered several stacked intervals of drift time instead of the thinner *slices* used for the width parameterization. On the already mentioned Figure 5.3, one example of the bins used to determine the threshold is shown.

From this point the leakage events can be described, being defined as the percentage of pulses of a certain separation that have their reconstructed separations below one of thresholds considered, according to the SS signal loss that is considered acceptable. For a separation of 2 mm no

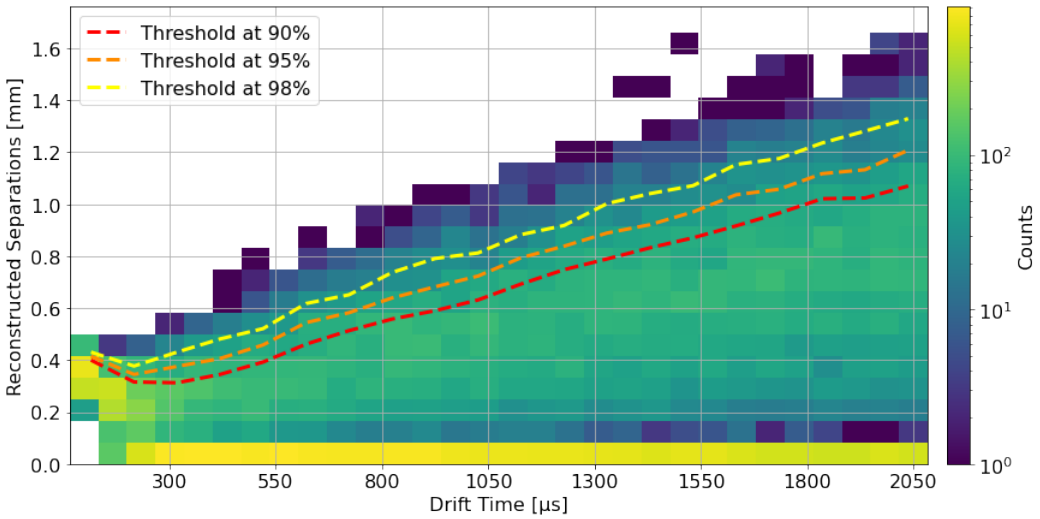

Figure 5.4: 2D Histogram of the density of reconstructed separations as a function of the drift time. The dashed lines represent three different thresholds considered corresponding to the fraction of SS S2 pulses bellow each line. The threshold increases with the drift time except for events with very low drift time. This behavior is explained by the deviation from a Gaussian distribution in this region to a square waveform.

leakage was found, meaning that the algorithm was able to reconstruct all the tested pulses above the threshold. Once more, the simplistic nature of the *S2Generator* influenced this result. For higher drift times the spread of reconstructed separations increases (see Figure 5.5) as is expected due to higher pulse width for that region [Sor11], which facilitates the existence of local minima to which the regression model can tend to. The choice of 2 mm stands on the fact that this is the minimum separation to which it is required to separate S2 pulses to increase the sensibility of $0\nu\beta\beta$ in ^{136}Xe. If smaller separations are considered, the trade off between background rejection would efficiency and loss of signal is disadvantageous for the sensitivity for the $0\nu\beta\beta$ decay (see Figure 4.4).

The simplicity of the generated pulses has a great influence in the determination of the threshold, as the lack of some effects considered originates the almost perfect Gaussian curves of the pulses. This will facilitate the reconstruction of the separations and therefore lower the value obtained for the threshold. Other contributory factor for the reduction of the calculated threshold is the population which was considered as SS. The fact that only zero separation pulses were considered may have created a bias towards lower values, since for some non null separations near zero the efficient separation reconstruction will not be possible. This subsequently will increase the threshold as there is no reliable method to distinguish these pulses from true zero separation ones. This region should be at separations lower than one standard deviation (1σ) where the summed pulse, even though it may be wider, falls within the statistical fluctuations region for the widths of SS pulses.

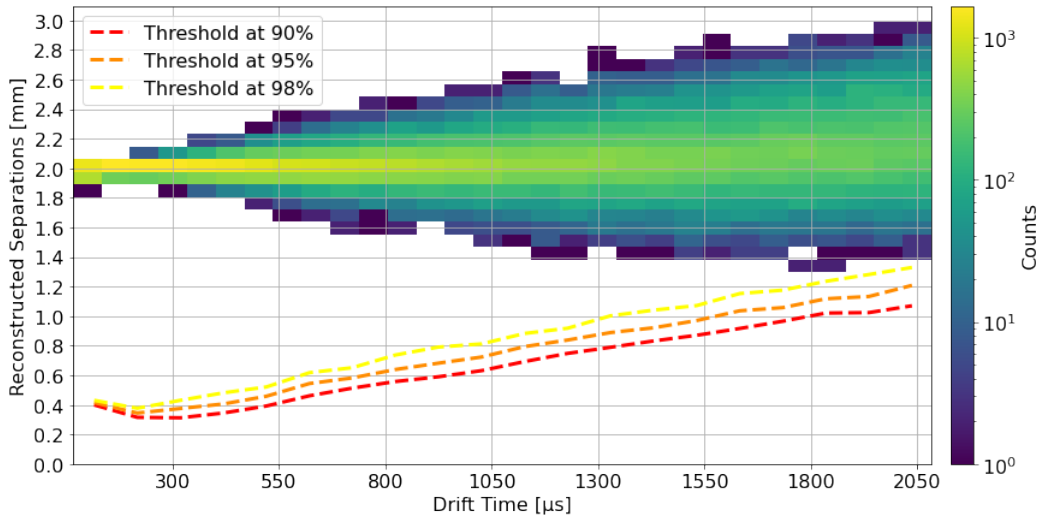

Figure 5.5: 2D Histogram of the density of reconstructed separations over the drift time for a MS population of pulses with 2 mm of separation. The leakage for every drift time bin is zero, meaning that no pulse was reconstructed to a separation below the thresholds.

5.1.2 Goodness of Fit Analysis as a SS/MS discriminant

The χ^2 test is used in statistics as a hypothesis test to examine if one categorical variable is significantly different from an expected behavior (in our case, the Gaussian shape of the SS pulses). This test examines the difference between the waveform and the fits using the expression

$$\chi^2 = \frac{1}{n}\sum_{i=1}^{n}\frac{(f(x,\vec{\beta})-y)^2}{y} \tag{5.2}$$

where the sum is done over all data and fit points. It was observed that χ^2_G (from the Gaussian fit) diverged much faster than χ^2_B (from the Bimodal) as the separation between pulses is increased which presented potential to be a good SS/MS pulse discrimination tool.

The use of a threshold can only go so far to discriminate SS and MS pulses, so an additional technique is used to identify the possible nature of the pulses. This is done by studying the χ^2 goodness of fit test for both Gaussian and Bimodal fits (represented as χ^2_G and χ^2_B respectively), by either comparing the two directly or by relating their ratio (defined as χ^2_B/χ^2_G) to the reconstructed separation. The zero separation pulses (or SS pulses) are recognizable by the similar magnitudes of both χ^2 resulting in a χ^2 Ratio near unity as is shown in Figure 5.6. Theoretically the ratio of χ^2 for zero separation pulses should be equal to one, but due to the conditions set for the fit boundaries, this might not be always the case. This happens because of the restricted nature of the width boundaries for the pulses in the Bimodal fit, that contrast with the relaxed boundaries set for the Gaussian fit. The pulse width could be smaller than the parameterized width for the Bimodal pulses, meaning that the Bimodal fit is comparatively worse. In these cases the Bimodal fit still converges to a separation of zero, as this minimizes the fit. The outcome of this difference results on a χ^2 ratio which may have deviated values from the unit as

seen in Figure 5.6, where the vertical distribution at zero reconstructed separation has a wide range of χ^2 ratio values. On the other hand, the fact that the Bimodal fit has the freedom to position the pulse means, for wider pulses, it can minimize the fit to a further extend compared with Gaussian fit. The result of this is the separation of the two means by a small amount.

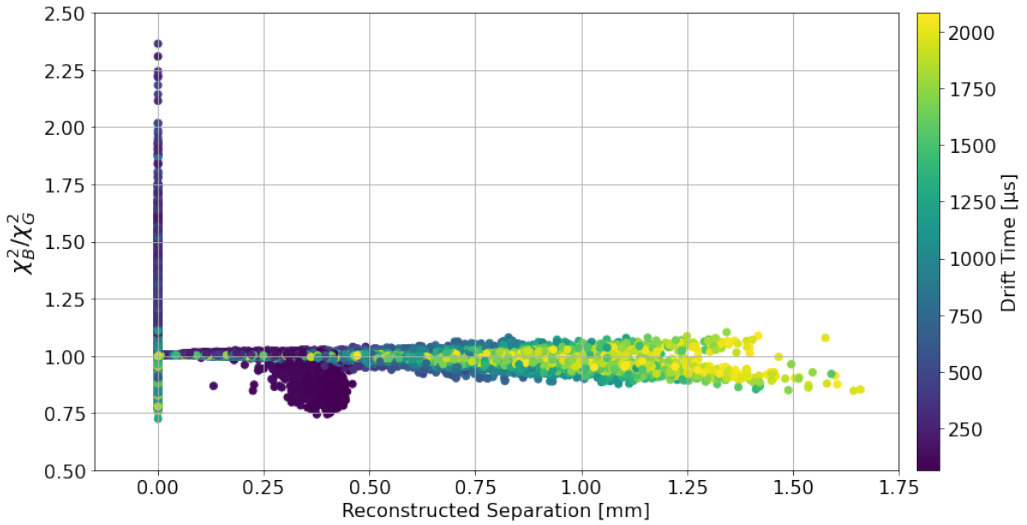

Figure 5.6: Scatter plot of the χ^2 ratio versus the bimodal Reconstructed Separation for SS events, where the color spectrum represents the drift time labeled by the color bar on the right side.

A dual behavior can be observed in Figure 5.6 for high drift time (yellow dots), where a bifurcation is identifiable resulting from the minimization effort of the algorithm, but now a subtle distinction arises. In both cases the width of the pulse is larger than the parametrization (otherwise the reconstructed separation would have been zero). The distinction stands of the fact that in some cases the separation maximization minimizes the χ^2_B to a great extend (lower bifurcation) while on others it brings no benefit compared with the minimization done by the Gaussian fit (upper bifurcation), suggesting that exists an instability point around the unit for the ratio of χ^2. In these scenarios the χ^2_G remains stable.

For low drift times, the scenario when the parameterized widths are lower than the distribution of the pulse widths happens, being identifiable in Figure 5.6 by the concentration of very low drift times (dark blue) centered around a value of reconstructed separation and lower χ^2 ratio value. In this region of drift time the width of the S2 pulse begins to reach the width of the light signal of a SE (which has a fixed value given by the model in Figure 4.3) resulting in a departure from a Gaussian curve to a more square waveform. Therefore, both fits will have a worse minimization, but favouring the bimodal fit due to its flexibility in rearranging the pulse positions. It was found that the Bimodal fit minimizes the regression by leaning the Bimodal distributions on either side of the S2 pulse. The ratio between the parameterized and real widths gives the value to which the reconstructed separations are centered on.

The wide range of χ^2 ratios for pulses with the reconstructed separation equal to zero is explained by the fact that they are almost exclusively placed below the parameterization curve, meaning that the χ^2_G is smaller than the Bimodal counter part, except for some cases where the bimodal

fit converges to a null separation despite having the liberty to separate the individual pulses. These cases lay near the parameterization curve, where the local minimum for the non zero reconstruction still presents some instability.

For non null separations (MS pulses), the χ^2_G starts to diverge as the waveforms no longer follow a Gaussian distribution. However, the χ^2_B remains relatively constant. The ratio between the two will therefore tend to zero as the separation of the pulses increases. The rate to which the χ^2_G diverges varies with the drift time because of the different pulse timing resolutions. So, for different drift times and a fixed separation the χ^2 ratio will vary as observed in Figure 5.7 for a set of generated pulses with 2 mm of true separation.

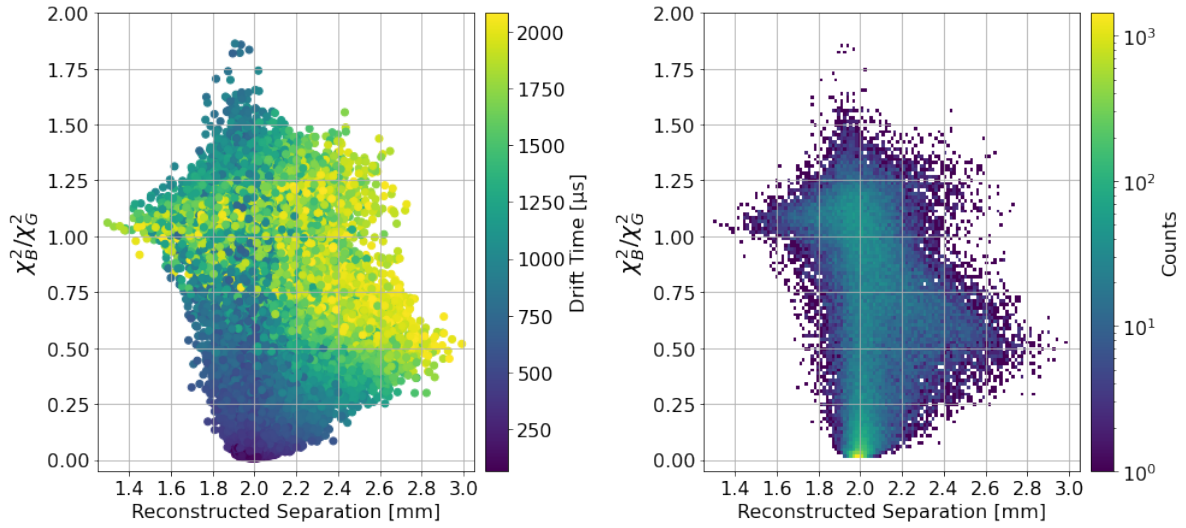

Figure 5.7: Scatter plot of the χ^2 ratio as a function of the reconstructed separation for a set of generated pulses with 2 *mm* of separation, color representing the drift time of the pulse (*left*) and the 2D Histogram of the same distribution which shows that the reconstruction is centered on the true separation of the pulses (right).

For high drift times, the bifurcation is still visible as 2 *mm* corresponds to 0.74σ of the pulse width at 2000 μs of drift time, which means that the waveform still closely resembles a Gaussian distribution. For low drift times the χ^2 ratio value is close to zero and increases with the depth of the events. Even though the χ^2 ratio for 2 *mm* takes values that may be thought or interpreted as SS pulses, the reconstructed separation axis show that the separations obtained are above the thresholds calculated previously. This means that it is possible to define a region within the two dimensional phase-space, of reconstructed separation and χ^2 ratio where SS pulses may be identified with high accuracy. If bigger separations are used, the χ^2 ratio for higher drift times will tend to decrease and will lead to a smaller spread of reconstructed separations.

5.1.3 Homogeneous Separation

The analysis presented in the previous section can also be performed wit a dataset with pulses with a uniform distribution of separations and drift times. Figure 5.8 shows how the recon-

structed separations compare with the true separations set in the *S2Generator*. As previously discussed, the dispersion of the reconstructed separations is dependent on the relation between the separation of both S2 pulses and their width. This effect is noticeable in Figure 5.8, where the biggest spread of reconstructed and true separations occurs for higher drift times.

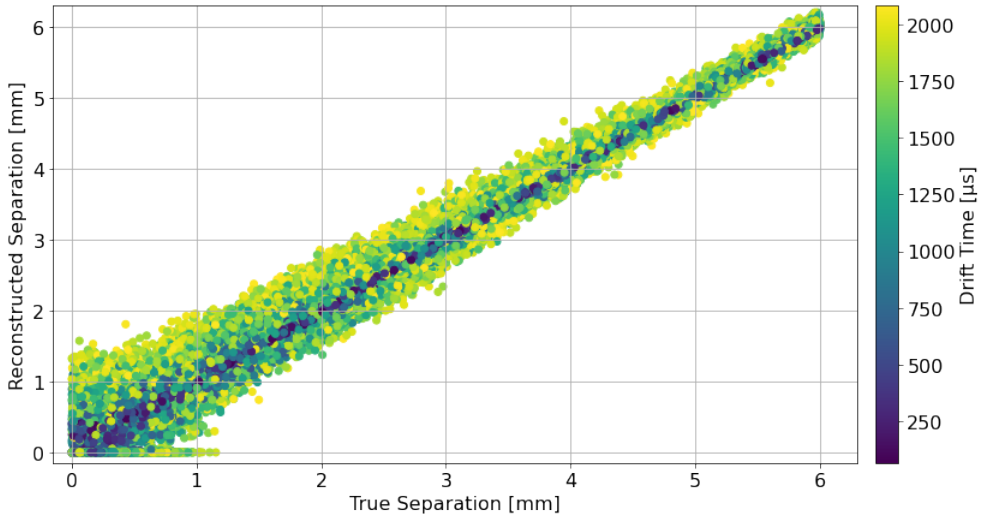

Figure 5.8: Scatter plot of the reconstructed separations versus the separations set in the *S2Generator*, where the color spectrum represents the drift time of the pulses.

As expected, for higher depths and separations close to zero the result is a larger spread of reconstructed separations. This occurs due to the wider nature of the pulses at higher drift times and to the inefficient reconstruction for separations near zero. The spread seen in Figure 5.8 is the result of the two effects. Nevertheless, the algorithm is able to reconstruct the separations efficiently, as the majority of the pulses match the separation set in the *S2Generator*. From Figure 5.8 is also noticeable the region of true separations where the algorithm no longer reconstructs pulse separations equal to zero, which are lower than the threshold for each correspondent drift time.

One phenomenon made clear in this data (which explains the distribution of reconstructed separations in Figure 5.3) was a tendency for the algorithm to reconstruct pulses with true separations close to zero as having either reconstructed separation equal to zero or tending to a non-zero distribution of values (see Figure 5.9). The former occurs when the pulses are narrower than what the algorithm expects thus forcing the Bimodal fit to overlap both distributions, while the latter occurs for wider than expected pulses, as explained in section 5.1.2. For very low drift time pulses the SE light signal width also plays an important role, resulting in the convergence to non-zero reconstructed separations observed if Figure 5.9a. For higher drift times the convergence to non-zero reconstructed separations still exists as Figure 5.9b shows, but it only depends on the local minima found by the algorithm itself. This tendency increase the value of the threshold (see section 5.1.1) resulting in a larger range of reconstructed separations which the algorithm can not reconstruct efficiently. However this effect should not be problematic if these very low drift times are excluded (see section 3.4.4).

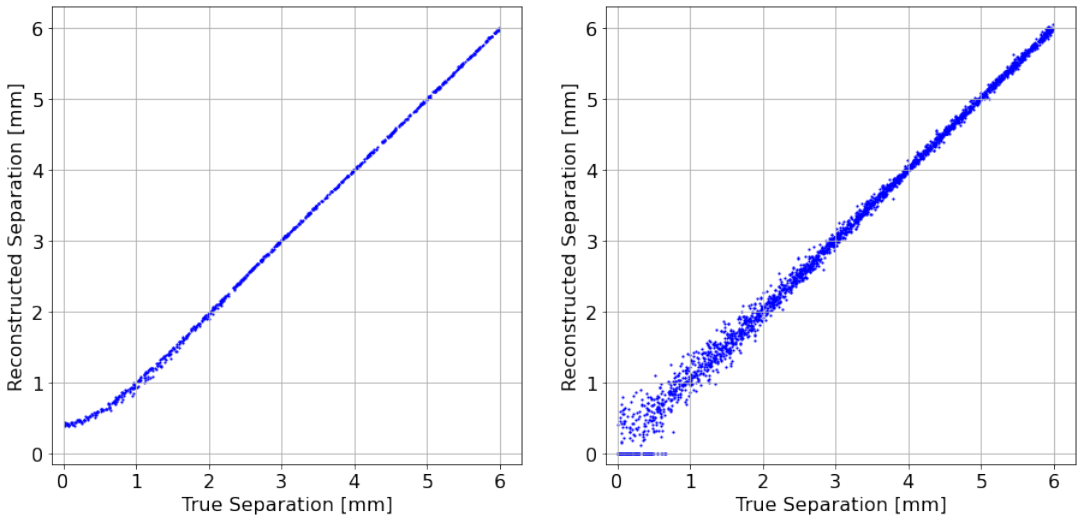

(a) Drift time $< 80\mu s$ **(b)** Drift time $= 825 \pm 25\mu s$

Figure 5.9: Scatter plot of the reconstructed separations versus the true separations set in the *S2Generator* for two intervals of drift time corresponding to near the minimum (**a**) and maximum (**b**) drift times of LZ.

Combining the knowledge that was presented so far and using the threshold determined in section 5.1.1, it is easy to identify which pulses were reconstructed below and above it, subsequently isolating them from one another to understand how each set can be identifiable within the reconstructed separation and χ^2 ratio phase-space mentioned before.

For simplicity and readability, only two slices of drift time are presented in this chapter, corresponding to the middle of both the TPC of the LZ experiment and the XLZD Consortium. Nevertheless, a complete description of the reconstruction efficiency of the algorithm is done for all drift time intervals. The intervals of drift time used are compressed between 720 and 875 mm for LZ and between 1495 and 1650 mm for XLZD.

To fully describe the contamination of pulses reconstructed at separations on either side of the threshold comparatively to their true generated separation, it is necessary to introduce a terminology to keep track of each population based on a classification system. SS pulses will be considered as the *positive* (P) class and the MS as a *negative* (N) class, where SS are defined as having a reconstructed separation below the threshold and the MS as being reconstructed above. If both reconstructed and true separations are below or above the threshold the event is considered as *true* (T), but if one is below and the other above it is considered as *false* (F). This classification system is summarized on Figure 5.10.

Some of the events are not going to be reconstructed correctly and will leak into a different population, resulting in a contamination of the SS or MS populations. It is important to distinguish the use of the term contamination and the term leakage. In this work the term leakage is used to describe the percentage of events with a fixed true separation that are reconstructed to separations below the threshold. The term contamination represents the percentage of events of a continuous distribution of true separations larger than the threshold that are reconstructed

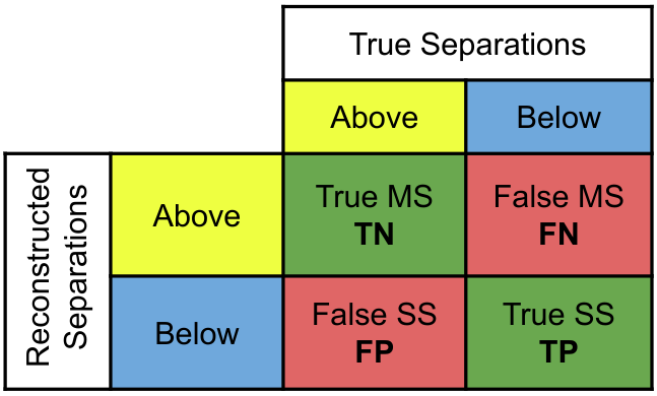

Figure 5.10: Classification parameters for reconstructed waveforms, where *Above* and *Below* represent if the the reconstructed or true separations are above or below the threshold. The text in bold combine the meaning of the different classification classes.

below that same threshold. This contamination, also known as *False discovery rate* (FDR) is defined as

$$C = \frac{FP}{FP + TP} \tag{5.3}$$

The contamination increases inversely with the threshold, which is explained by the greater reconstruction error at lower true separations. The contamination for LZ mid depth was 15.3% for the threshold at 90% and 8.9% at 98%. For longer drift times, the contamination is reduced to 5.8% and 3.8% for the threshold at 90 and 98%, respectively. The χ^2 ratio distribution for both intervals is similar, but for shallower depths the convergence to zero is faster, as seen in Figure 5.11. This behavior is explained by the better width resolution compared with pulses originated from greater depths, explained previously.

As seen in Figure 5.11, the way the threshold is defined excludes a considerable number of pulses which may be SS, since their χ^2 ratio is very close to unity. Remembering that the threshold may be under valued as it was explained before, it may be necessary for real data (in future iterations) to define a non linear threshold. Possibly being defined by a linear term (the threshold described so far in this work) plus a term with a dependence with the distribution expected for the χ^2 ratio for SS pulses, in order to increase the classification efficiency.

The particular analysis presented here for these two drift time intervals may be helpful to explain some specific aspects of the algorithm's behavior, but a more generic approach is necessary. Expanding the contamination calculation to all drift times, two behaviors are clear in Figure 5.12. For low drift times there is a clear rise on the contamination level caused by the fact that the threshold is smaller and the spread seen in Figure 5.8 for small separations becomes more prevalent. This tendency is broken for the lowest drift times due to the poor parameterization in this region, which causes the reconstructed separations to have a bias towards bigger separations for pulses close to zero separation (as explained for Figure 5.9a). This results in the reconstructed separation being overestimated for any pulse separation higher than zero, so every pulse with a

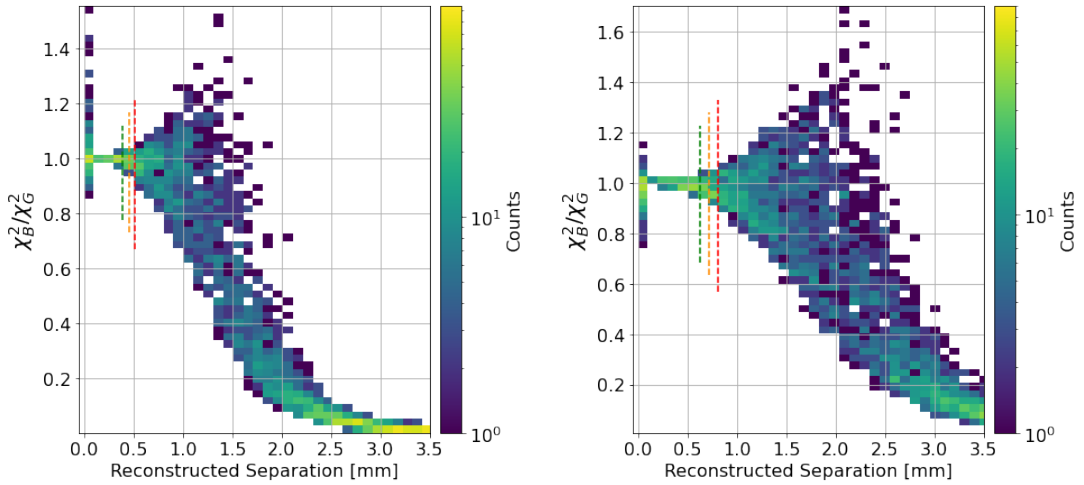

(a) Drift time Interval = [720;875] mm **(b)** Drift time Interval = [1030;1185] mm

Figure 5.11: 2D Histogram of the densities of waveforms, where the dashed lines represent the different threshold, green at 90%, orange at 95% and red at 98%.

true separation greater than this minimum will be reconstructed very easily above the threshold. The down side are the possible SS pulses reconstructed as MS. As this effect becomes less prevalent, the contamination level rises, reaching its maximum at around 400 μs of drift time.

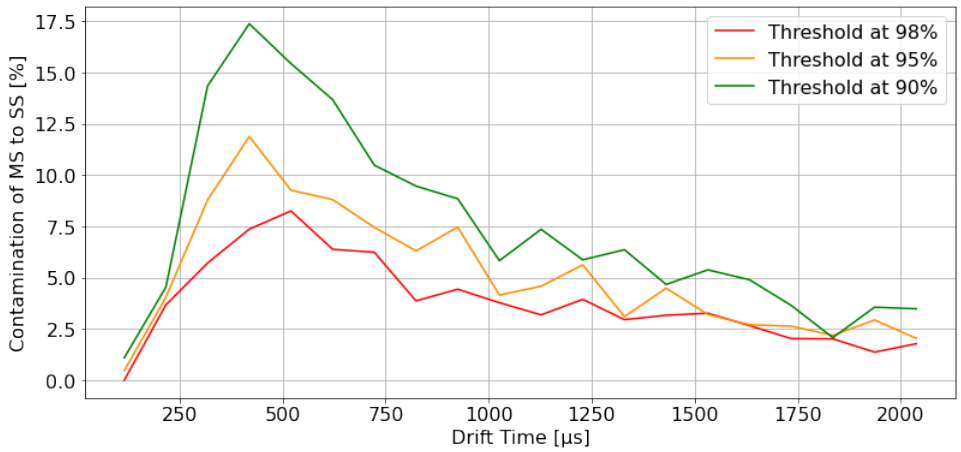

Figure 5.12: Contamination dependence with the drift time for the three thresholds considered from a data set of uniformly distribution drift times from 65 to 2050 μs and separations from 0 to 6 mm.

From the generated data it is possible to conclude that the algorithm performed well in discriminating SS and MS pulses, reconstructing the pulse separations better than expected considering that drift times of the order of milliseconds were considered. The threshold and χ^2 ratio test proved to be reliable mechanisms of classification which gives confidence to use them with real LZ data and the values for contamination obtained were very good: using the 90% threshold the contamination does not reach 10%.

5.2 Analysis of LZ data from SR1

One of the main objectives of the work plan for this thesis was to analyse real data, as the algorithm developed is intended to be implemented within the framework of LZap or as a posterior analysis module with the objective of increasing the sensitivity of the LZ experiment, with special focus in the $0\nu\beta\beta$ decay. For this purpose, events from SR1 of LZ with reconstructed energy greater than 1 MeV and classified as SS by LZap were selected. Some of these events contain S2 pulses whose width does not follow the expected distribution. It is possible to observe from Figure 5.13 that a considerable amount of S2 pulses in this energy range have widths that are larger than expected for their respective drift time, deviating from the main distribution. These S2 pulse are potential MS candidates that the LZap framework could not resolve.

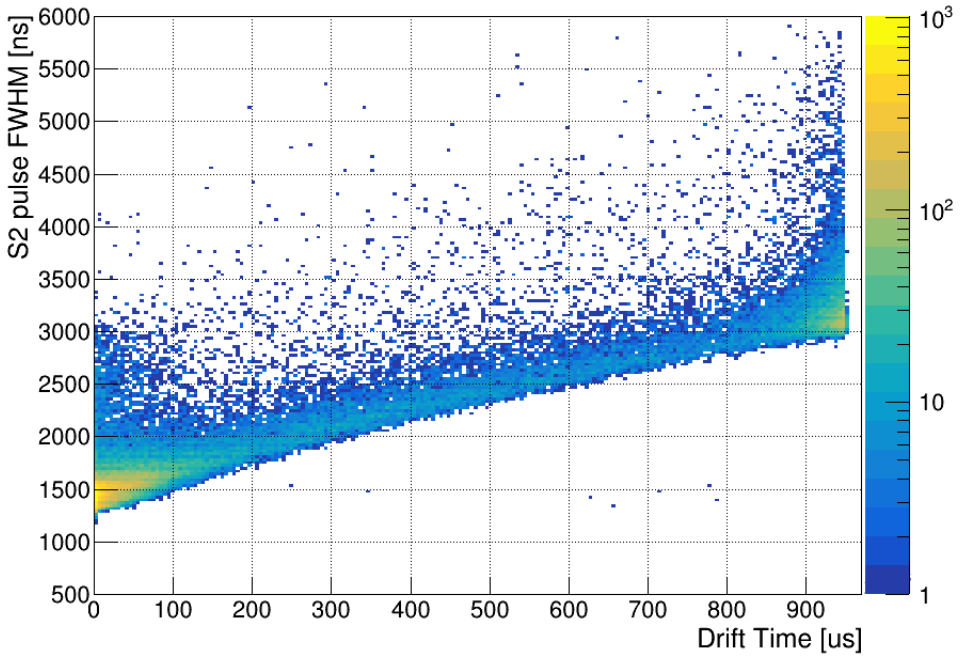

Figure 5.13: Events classified as SS by the LZap for energies higher than 1 MeV.

First, it is necessary to identify which pulses are consistent with SS in order to parameterize the fits performed by the algorithm and produce estimates for the SS thresholds described in section 5.1.1. A hard cut was made, following the estimated curve taken from the distribution of widths from the population of ^{131m}Xe plus an offset to include a similar band width seen in Figure 5.1. The pulses beneath the cut are considered to be SS consistent pulses and above it are the MS candidates. As this is a simple cut, a bias has definitely been introduced, so further studies must include slightly different cuts to study the effect on the results. Cuts on the drift time were also included as the pulses near both ends of the TPC behave in a non standard way, as well as a fiducial cut on the radius to exclude pulses near the walls as these events are not well reconstructed due to charge trapping in the PTFE and reduced number of PMTs directly measuring electroluminescence light.

The SS population considered was chosen to be within a certain region and from now on any

mentioned of it is done by using the term *"regular S2s"*, as there is no certainty that these are in fact all the SSs or that no MS pulses are present. In reality, a perfect cut doesn't exist as there will always exist some level of contamination for both sides.

The parameterization must be done and as was the case for the generated pulses, the median width over the drift time was determined by taking slices and fitting the distributions with Gaussian functions. Figure 5.14 shows the distribution of the events selected below the cut, to which the points were fitted to the model described by Equation 4.2, resulting in the dashed red curve.

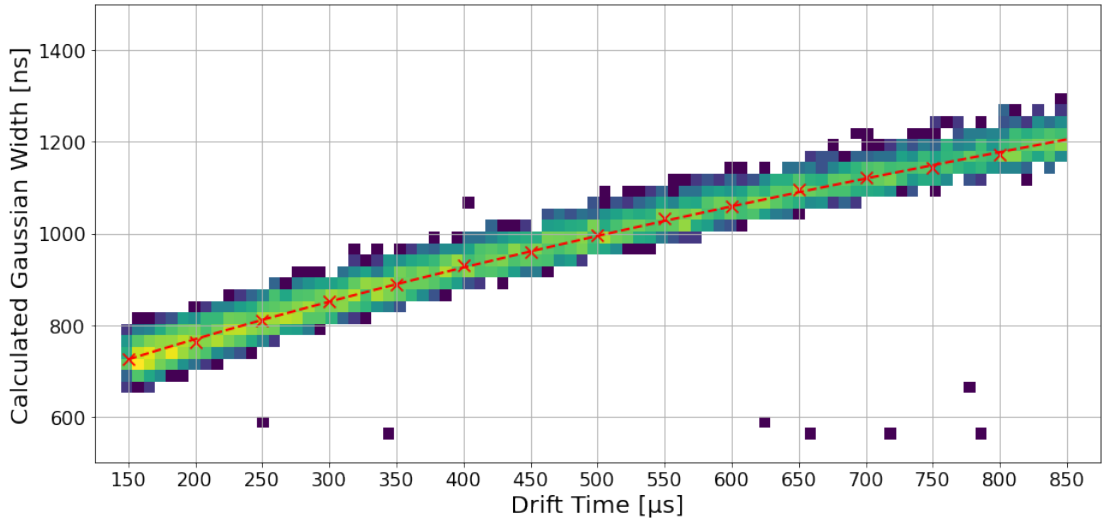

Figure 5.14: Parameterization of the median pulse width over the drift time for the SS events selected by the hard cut, where fitted parameters correspond to $p_0 = 326103.96 \pm 4420.19\ ns^2$ and $p_1 = 1.3257 \pm 0.0096\ ns$.

Some considerations must be taken into account about the parameterization. The width of the pulses for high energy pulses is slightly larger than the widths for lower energies due to to the existence of some effects such as S2 tails caused by the photo-ionization of the grids, retarded emission of electrons and the possible saturation of the PMTs. Other effects such as Bremsstrahlung or delta particles emission can also play a role, but as the charge density of the electron cloud is larger their effect is negligible. Here, the parameterization was done using the high energy pulses selected before since these are the subject of study, otherwise the reconstructed separation could have been overestimated. However there could be an argument for the use of low energy pulse parameterization, as these pulses present fewer artifacts that may change the pulse shape. This means that these pulses have almost a perfect normal distribution of light collected. If used, these would introduce a bias towards the zero separation as these pulse have smaller widths compared with high energy pulses.

5.2.1 Measurement of the LZ SS Threshold from SR1 Data

The SS thresholds are determined using the same method that was used for the generated waveforms. However, the number of pulses is much more reduced in the SR1 data and the drift time range only extends to that of LZ. For those reasons the number of bins of drift time is reduced to have enough statistics in each bin. Figure 5.15 shows a histogram of the reconstructed separation as a function of drift time for the *regular S2* pulses, with the calculated thresholds of 90%, 95% and 98% overlaid. A dependence of the thresholds on the the drift time is clearly observed.

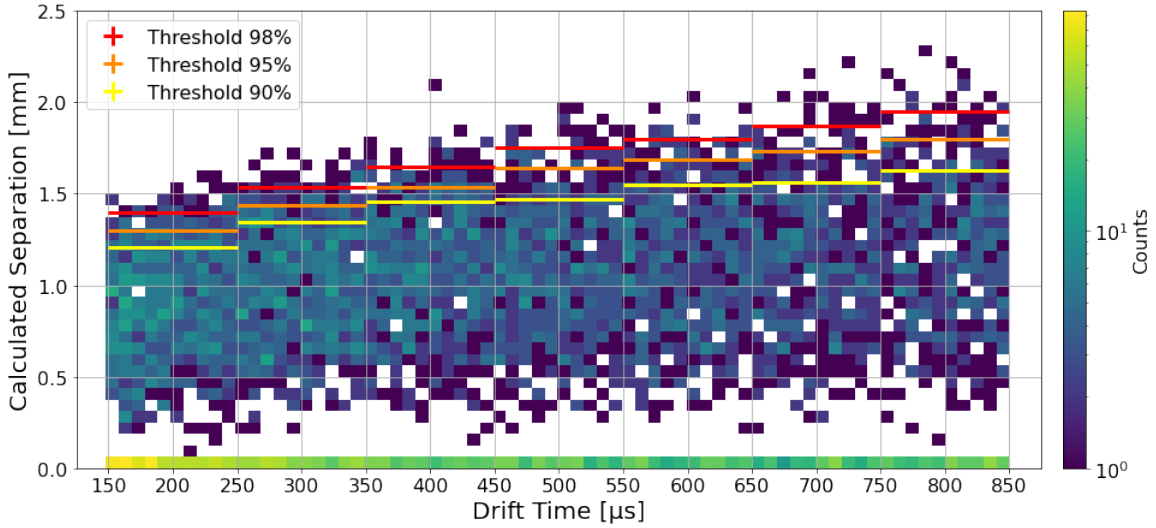

Figure 5.15: 2D Histogram of the density of reconstructed separations over the drift time. The horizontal lines represent three different thresholds (90%, 95% and 98%), where their widths are the size of the bins which they correspond to.

One important aspect that should be mentioned is that the threshold does not follow the same dependency with the drift times as the widths. This can be evidenced by the ratio between these two quantities for both ends of the drift time ranges, where the width for the highest drift time is about 1.7 times higher than for the lowest but for the threshold this ratio is only 1.3, meaning that the threshold has a more complex dependency. It is not clear if the hard cut done for this population of regular S2s has any effect on this dependency, but this was not investigated in this work.

5.2.2 Reconstruction of S2 Pulses with Expected Width Distribution

The determination of the distribution of the χ^2 ratio of the pulses is done to check if the they are consistent with the expected distribution for SS pulses (as seen in Figure 5.6), which should be around the unit value. Figure 5.16 shows the 2D histogram of the reconstructed separations for the *regularS2* pulses across all LZ drift times. It is possible to see that the majority of the pulses have the expected χ^2 ratio distribution. Even though some have a lower ratio that

may be indicative of a possible contamination from actual MS pulses, the overall distribution provides some level of confidence that the cut used was effective at separating potential SS S2 candidates. But only when comparing this analysis with the equivalent for the MS candidates pulses can some more definite conclusion be extracted.

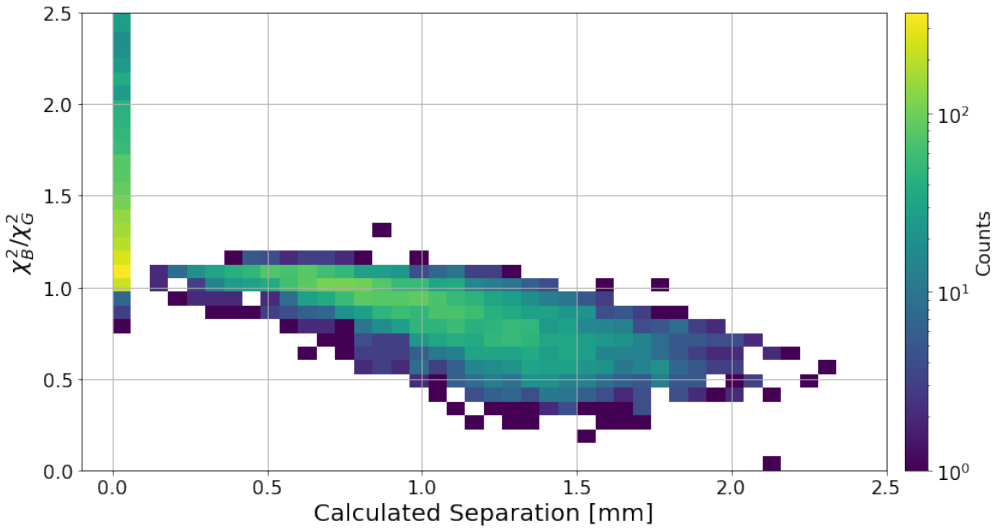

Figure 5.16: 2D Histogram of χ^2 ratio versus the reconstructed separations for the selected SS pulses.

Figure 5.17 presents some examples of waveforms that were reconstructed with zero separation, where the effects previously mentioned in section 4.2 that cause the pulse to deviate from the Gaussian shape are now noticeable. Despite these effects, the algorithm was able to reconstruct the original waveform with success. When the Bimodal fit converges to the minimum separation (both means take similar values), the asymmetry also converges to the minimum, where both bimodal distributions have similar amplitudes. This happens in all the cases when the reconstructed separation is zero, since the minimum pulse height of the fits stands at 15% of the maximum of the the waveform and therefore not enabling one of the pulses to have a null amplitude.

Some events were identified as *accidentals* where LZap defined an event with mismatched S1 and S2 signals. An example of this can be found in Figure 5.17d where the event was identified as having a much higher drift time than the S2 pulse width would indicate. In this case, the true S1 signal of the event was not identified as a separate pulse, and was actually merged in the S2 pulse by the *DoGPulseFinder*. This S2 was then matched with an isolated S1 that occurred several hundreds of μs before. This only happens for pulses near the surface of xenon. Some of the pulses which were reconstructed with higher separations had some artifacts near the maximum of the waveform as the example in Figure 5.17c shows, which may have influenced the reconstruction to higher separations. These type of pulse were found mainly for events occurring at higher depths in the TPC of LZ. Thise effect was caused probably by the saturation of some of the PMTs that may cause the shape of the pulse to be deviated from the expected pattern.

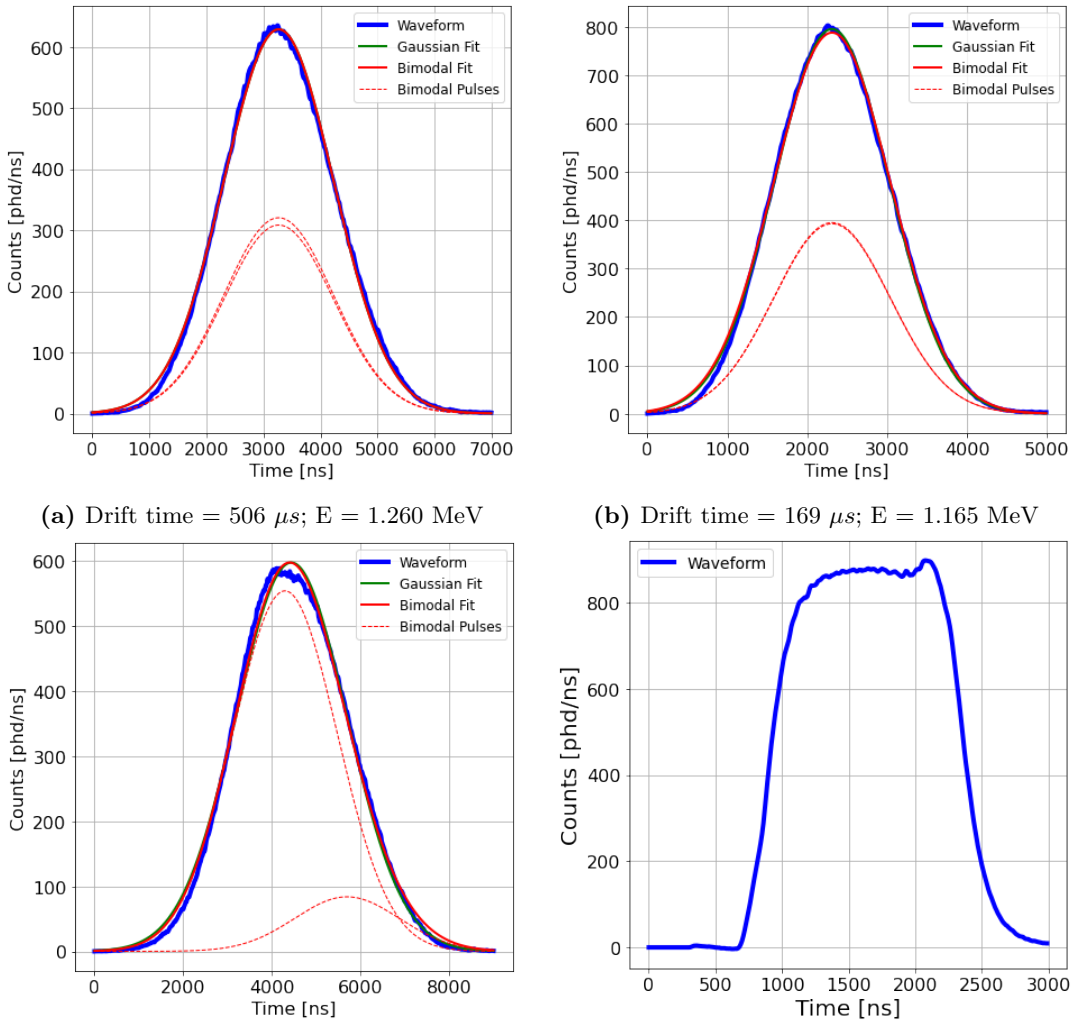

(a) Drift time = 506 μs; E = 1.260 MeV

(b) Drift time = 169 μs; E = 1.165 MeV

(c) Drift time = 815 μs; E = 1.340 MeV

(d) S2 pulse from a accidental coincidence event.

Figure 5.17: Examples of reconstructed waveforms in the *regularS2* population. For **(a)** and **(b)** the reconstruction converged to zero and the both Bimodal pulse heights assumed similar values. For **(c)** the separation reconstructed separation value is similar to the threshold for the corresponding drift time and **(d)** shows a S2 pulse from an accidental coincidence event which in fact includes the true S1 (visible as a small *"bump"* in the pre-pulse baseline) as this event happened very close to the gate grid.

5.2.3 Reconstruction of S2 Pulses with Wider Width Distribution

Using the threshold calculations from section 5.2.1, it is possible to determine how many MS candidates were reconstructed below them. As seen in Figure 5.18, the majority of the pulses were reconstructed above the thresholds. The worst case scenario, corresponding to the threshold at 98%, was 21.50% contamination for the drift time interval between 450 and 550 μs. This value should not be interpreted too harshly as the density of events near the threshold is higher and thus increasing this leakage.

The contamination for these pulses is relatively constant with the threshold as seen in Figure

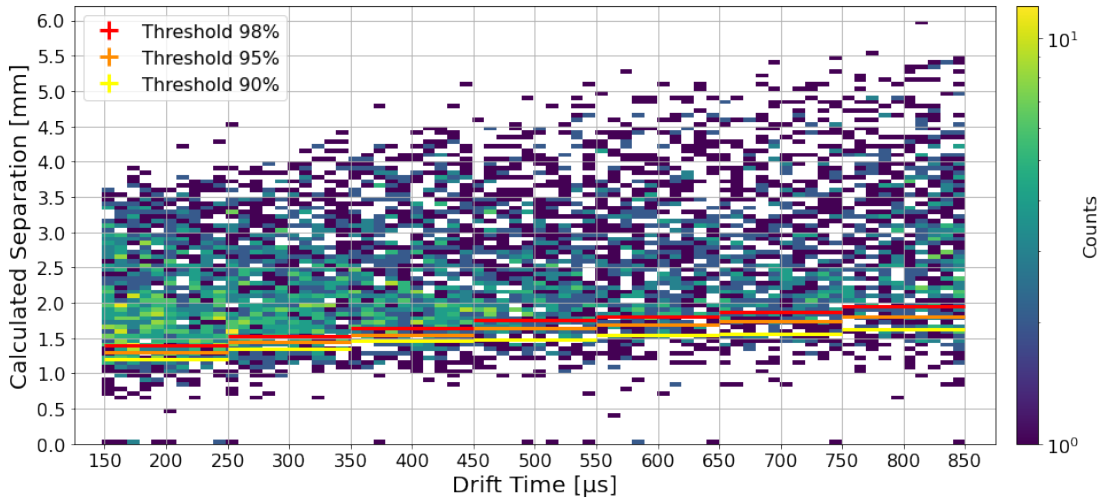

Figure 5.18: 2D Histogram of the density of reconstructed separations of candidate MS pulses over the LZ drift time.

5.19, for all levels of threshold considered, so a mean contamination can be calculated as a quantitative measure for each drift time, being 19.56%, 13.83% and 9.00%, for the thresholds at 98%, 95% and 90%, respectively.

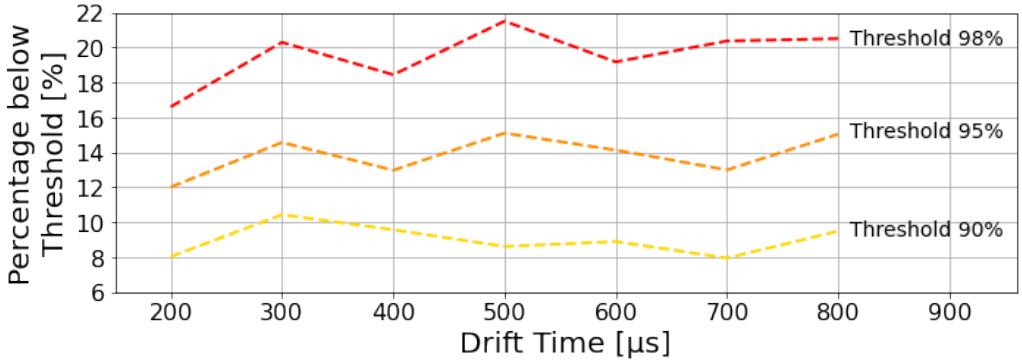

Figure 5.19: Contamination as a percentage of reconstructed separations below the threshold for all three thresholds considered.

The choice for the minimum pulse height of the Bimodal as 15% of the total height of the waveform has some effects on the efficiency of the Bimodal fit. With the restriction level utilized some waveforms cannot be fitted perfectly, as some of the structures of the S2 pulse might have a smaller height than the allowed limits of the fit. This constitute a limitation to the algorithm as they may represent a significant percentage of the pulses considered. If this minimum is lowered, other problems arise, such as the increase of the threshold due to some *regular S2* pulses having their reconstructed separations artificially increased. For MS candidate pulses, the contamination could also increase since the threshold would be higher. The performance of the algorithm is therefore very dependent on the limits imposed on the parameters of the bimodal fit, and the values used in this work were optimized to produce the smallest contamination possible for this particular selection of datasets. In the future, an exhaustive study of these choices of

limits will be performed to further improve the performance of the algorithm.

The χ^2 Ratio distribution for MS candidates is presented in Figure 5.20. It clearly shows that the Bimodal fit is reaching a better result for most of the pulses, as the highest density is near the value of zero as Figure 5.20 shows. Some of the pulses are consistent with being a SS, but this is expected to occur as the hard cut done to differentiate between the two populations of *regular S2* and possible MS candidates inevitably includes contamination. This results in the possible contamination of MS pulses on the selected SS population and of SS pulses within the region of MS candidates. Some outliers are identifiable by the large values of χ^2 ratio. These represent poorer fit results for the Gaussian and bimodal fits, with the latter having much worse minimization to the fit than the former. These waveforms will be discussed in section 5.2.4.

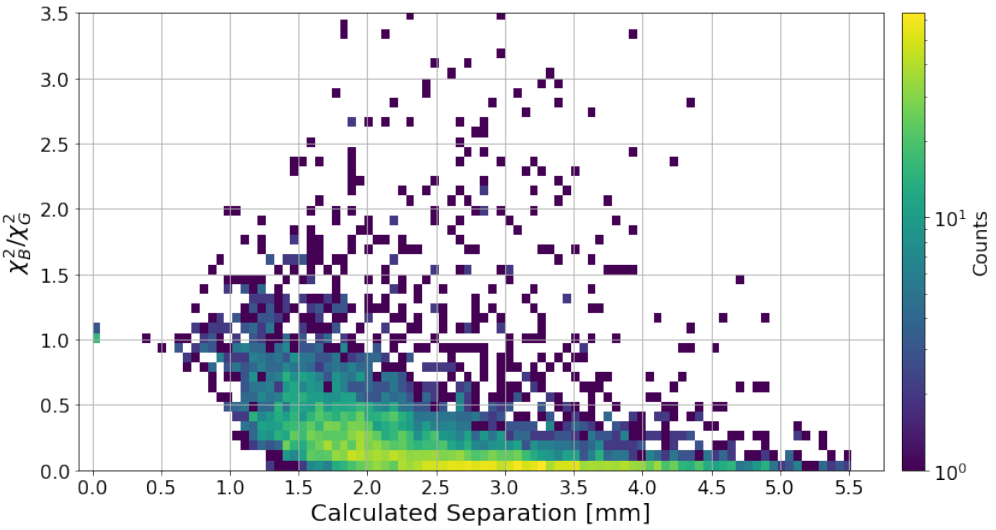

Figure 5.20: 2D Histogram of the χ^2 ratio with the reconstructed separation for MS candidates in the SR1 dataset.

The algorithm is capable of distinguishing two pulses with some level of confidence, which have their reconstructed separations just above the threshold. In this region, the pulses still can be considered to be very close to the expected normal distribution, however the width of the Gaussian fit (which is unrestricted) is clearly larger when compared with the width of the bimodal fit which is set based on the expected width for the corresponding drift time of the event. Example of waveforms with reconstructed separations near the threshold are shown in Figure 5.21 for both the lowest and highest drift time bins to illustrate how the algorithm is performing. Figures 5.21c and 5.21d show examples of pulses that LZap was not able to separate but that the algorithm clearly could find and reconstruct two identifiable distributions.

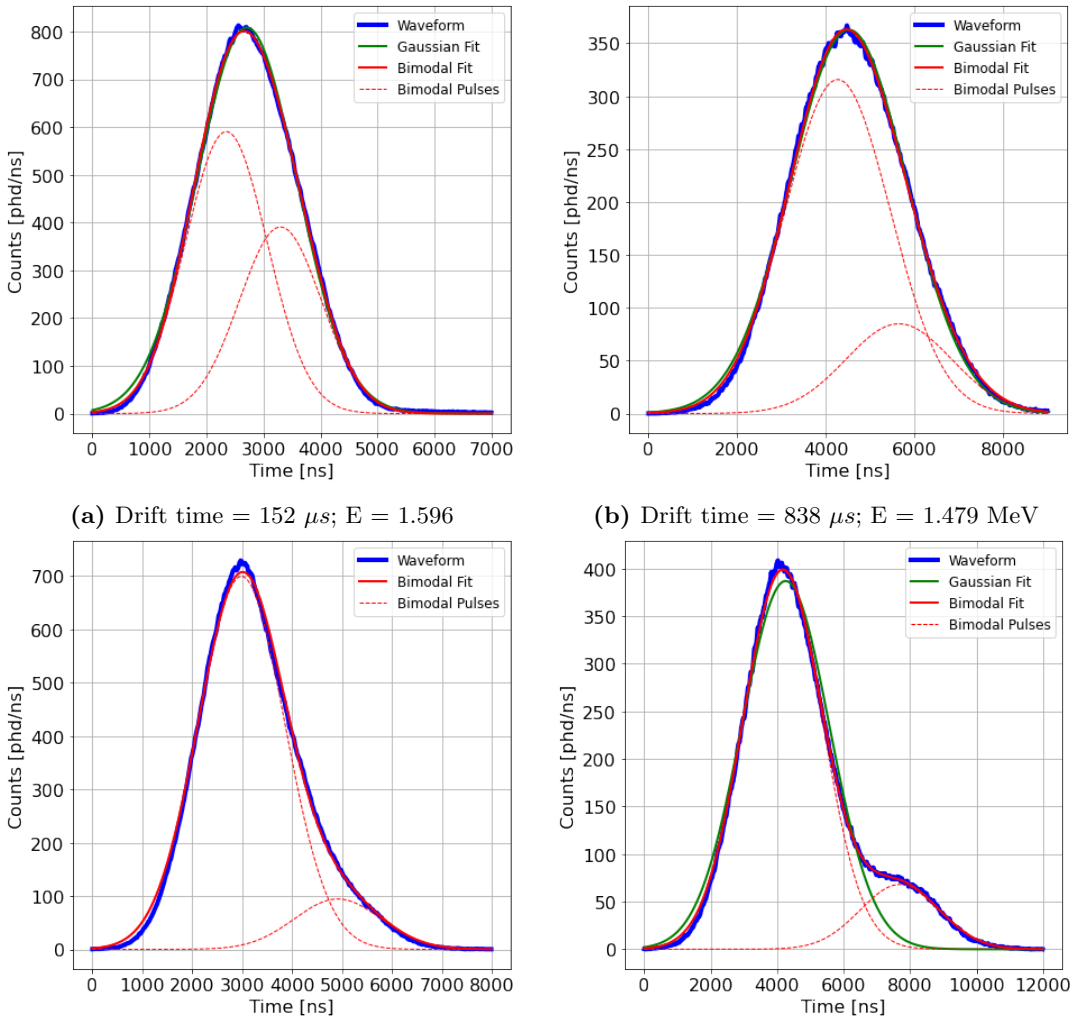

(a) Drift time = 152 μs; E = 1.596

(b) Drift time = 838 μs; E = 1.479 MeV

(c) Drift time = 339 μs; E = 1.418 MeV

(d) Drift time = 846 μs; E = 1.168 MeV

Figure 5.21: Separation limit of the algorithm for the lowest **(a)** and highest **(b)** drift time bins, with reconstructed separations of 1.45 and 2.11 mm, respectively. The range of time is kept constant for both pulses. For **(c)** and **(d)** examples of waveforms that LZap could not separate which were clearly reconstructed by the algorithm developed.

5.2.4 Trimodal Fit

As seen in Figure 5.20, some pulses have a high reconstructed separation but their χ^2 ratio is larger than unity. When looking directly at the distribution of χ^2_G against χ^2_B it was found that both fits were reconstructing the waveform poorly. This is a consequence of the algorithm only searching for single (Gaussian) or double (Bimodal) pulses, while in fact some pulses in this dataset have a multiplicity higher than two. The correct identification of these higher multiplicity pulses will also contribute for a higher sensitivity of the experiment, so they need to be taken into consideration.

To search for the possibility of higher multiplicity pulses, a model dubbed *trimodal* fit was set up,

which was straightforward to implement as it was only necessary to add two more parameters for a third pulse (as the width stays the same for each pulse). The constraints for the parameters remain unaltered to keep the results uniform. In equal manner to the previous discussed χ^2 ratio, if a new *trimodal* ratio (χ^2_{TR}) is defined as χ^2_B/χ^2_T where χ^2_T is the goodness of the fit of the trimodal fit. The discrimination power is similar to the original χ^2 ratio, resulting in a tool to identify possible pulses with multiplicity of 3. Even though no extensive analysis was done for the search of this class of pulses, several promising examples were found and a couple are shown in Figure 5.22, once more showing the potential of this algorithm for expanding the analysis of MS pulse discrimination.

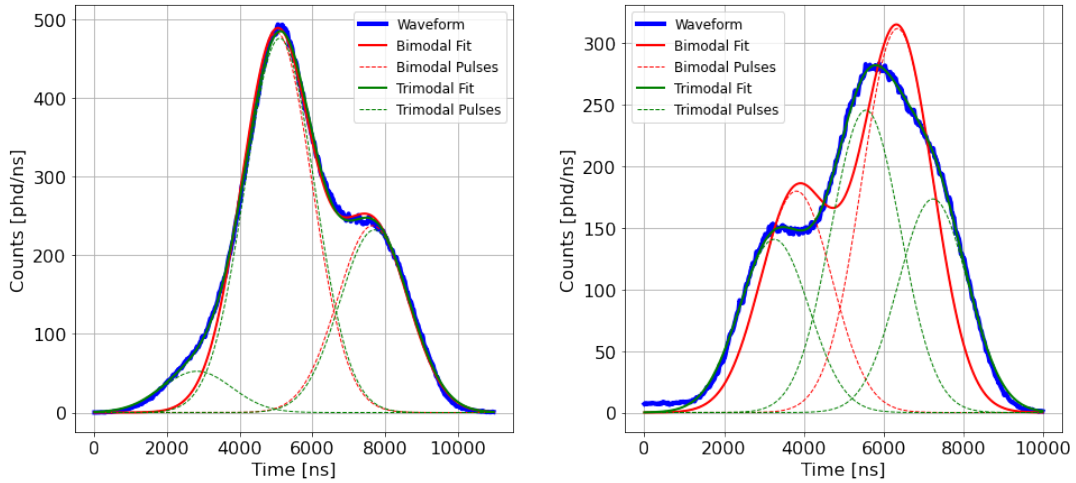

(a) Drift time = 447 μs; E = 1.755 MeV **(b)** Drift time = 340 μs; E = 1.190 MeV

Figure 5.22: Examples of some trimodal pulse candidates and the various levels of fits tested.

These are the two archetypes of pulses of multiplicity 3 found: in one of those (such as in Figure 5.22a) the Bimodal fit converged for two of the underlying S2 pulse positions correctly, and the other (such as in Figure 5.22b) where it could not fit the waveform as a whole. The first case usually happens when the third underlying pulse has a much lower area than the first two and its contribution to the minimization of the fit is negligible.

One aspect to take into consideration is the over fitting, meaning that a complex model can most times be fitted to a simpler distribution. This was already seen in the Bimodal fit where it sees two pulses in SS pulses, which was the reason that a threshold definition was needed in the first place. Nevertheless, higher multiplicity pulses should be included in a systematic analysis to discriminate as much MS pulse as possible.

Chapter 6

Conclusions

The Masters activities were carried out at the *Laboratório de Instrumentação e Física Experimental de Partículas* (LIP) at the Physics department of the University of Coimbra. The author has been an active member of the Dark Matter Group on which this work is inserted, participating in the weekly group meetings and on several activities promoted by LIP. The work performed was inserted in the LUX-ZEPLIN (LZ) Collaboration and XLZD Consortium for a next generation (G3) dark matter experiment where the authors work has been discussed with the prospect of being implemented to improve the sensibility of both experiments. The objective set for the Masters project was successfully completed and also surpassed the initial expectations. The work developed has shown great potential in increasing the sensibility for high energies for the LZ experiment and of being potentially used in different experiments using similar detection technologies. With the results obtained, it was shown that the algorithm developed has potential to help on the observation of the neutrinoless double beta decay ($0\nu\beta\beta$) in ^{136}Xe.

The objective set for this projected was the improvement of the data processing and analysis framework of LZ (LZap) on the capability of distinguishing merged pulses within the region of high energies on which the $0\nu\beta\beta$ decay is inserted. It was originally planed to use ^{22}Na calibration data from MDC3 (mock data from the simulations discussed in section 3.5) for the development of the algorithm, however this data was shown to have unforeseen issues and had to be discarded. So, a different approach was chosen were a S2 like pulse generator (*S2Generator*) was used to create sets of data to develop and fine tune the algorithm parameters. On later stages it was possible to analyse the performance of the algorithm in real data from the first *Science Run* (SR1) of LZ, which was not initially projected to be included in this work, representing a huge leap on the relevance of the work here presented. The objectives set for this work tried before by other people with mixed results. The reasons for the success of the approach presented

in this work are tied to the choice of the methods used, i.e. the regression analysis using Gaussian fits with very constraint parameters. This solution of strongly tightning the parameter space of the fit, with emphasis on the expected S2 width as a function of the drift time was not entirely clear at the start of the work but became the key feature of the algorithm.

The *S2Generator* was a simplistic tool designed taking into account the conditions of SR1 to provide S2 pulses similar to real waveforms of the LZ experiment. It gave the ability of creating large sets of data to be analysed, contributing to the well understanding and subsequent fine tuning of the algorithm as the metrics to classify the pulses could be studied in great detail. It is important to emphasize that the simplistic nature of the pulses was considered when discussing their analyses and how that influenced the results obtained and they compare with the performance of the processing framework of LZ (LZap). However, the algorithm showed that this philosophy works and that it has potential of separation of pulses for the drift times up to 2000 μs or 3 meters in depth, which are intended to be used on G3 xenon detectors.

The classification metrics where in part inspired (threshold) on [K$^+$22] which the first author contributed with very meaningful insight and discussions during the development of this work. The χ^2 analysis was a straight forward metric to use, since the core of this work is based on regressions to a set of data points.

For the SR1 data the algorithm performed beyond the expectations, improving the minimal vertical vertex separation assumed by LZ and was able to reconstruct multiple scatters events that LZap could not separate. In the best case scenario where the asymmetry of the pulses is only 50%, LZap can only separate pulses down to 3.7 mm and for all asymmetries its limit is at 4.4 mm. The algorithm far surpassed these limits by achieving a minimum separation of 2 mm for all the drift times with pulse asymmetries down to 15%. For low drift times it surpassed even the 1.5 mm limit for which the sensitivity to the half life of the $0\nu\beta\beta$ for the ^{136}Xe is expected to start decreasing due to the signal loss, meaning that this minimum limit can be reached and the sensitivity maximized.

Another important aspect to highlight is the consistency of the behavior metrics when analysing both generated and real data. This gives a good indication that they work reliably across different sets of data, demonstrating that the algorithm can be used in a variety of scenarios, not being limited to the LZ experiment. From the perspective of XLZD, this is of great importance as a background reduction tool. It was also found that the SS 98% acceptance threshold increases slower than the pulse width with respect to the drift time, which is given by Equation 3.10. Extrapolating for depths of 3 meters, this implies that the separation obtained for the LZ experiment would not deteriorate significantly for a TPC twice as deep, possibly resulting in a higher sensibility than is currently expected for G3 detectors. The algorithm also showed the capability of identifying and reconstructing pulses with multiplicities of three (three interactions distinguishable in the z direction), a result that was not initially planed.

Since this work was developed within a Masters project, the amount of time allocated for the development was limited, reaching only a fraction of what could be done. Therefore, this work has the potential of being the basis of a larger and far reaching project, where several other

studies and research could be done. These can include: studies on different choice of *regularS2* populations to understand how it influences the threshold, testing with different generators to further develop the metrics used, systematic analysis on pulse multiplicity higher than 2 and combine with xy plane separations.

This Masters program was integrated within two state-of-the-art experiments (LZ and XLZD, the latter still being planned), which provided the opportunity for the development of valuable programming and data analysis skills. Combining the individual knowledge acquired with the results obtained, it is fair to conclude that this project as a whole was a success.

References

[A+02] Rushdy Ahmad et al. Direct evidence for neutrino flavor transformation from neutral-current interactions in the sudbury neutrino observatory. *Physical review letters*, 89:011301, 08 2002. URL: https://journals.aps.org/prl/pdf/10.1103/PhysRevLett.89.011301, doi:DOI:10.1103/PhysRevLett.89.011301.

[A+16a] S. Andringa et al. Current status and future prospects of the sno+ experiment. *Advances in High Energy Physics*, 2016:6194250, 01 2016. doi:10.1155/2016/6194250.

[A+16b] S. Andringa et al. Current status and future prospects of the sno+ experiment. *Advances in High Energy Physics*, 2016, 01 2016.

[A+17a] M Agostini et al. First results from gerda phase ii. 888:012030, 09 2017. doi:10.1088/1742-6596/888/1/012030.

[A+17b] D. S. Akerib et al. Results from a search for dark matter in the complete LUX exposure. *Physical Review Letters*, 118(2), jan 2017. doi:10.1103/physrevlett.118.021303.

[A+17c] C. Alduino et al. The projected background for the cuore experiment. *Eur.Phys.J.C*, 77(8):543, 2017. URL: https://hal.archives-ouvertes.fr/hal-01645294, doi:10.1140/epjc/s10052-017-5080-6.

[A+19] G. Anton et al. Search for neutrinoless double-β decay with the complete exo-200 dataset. *Phys. Rev. Lett.*, 123:161802, 10 2019. doi:10.1103/PhysRevLett.123.161802.

[A+20a] M. Agostini et al. Final results of gerda on the search for neutrinoless double-β decay. *Phys. Rev. Lett.*, 125:252502, 12 2020. URL: https://link.aps.org/doi/10.1103/PhysRevLett.125.252502, doi:10.1103/PhysRevLett.125.252502.

[A+20b] D. S. Akerib et al. Projected sensitivity of the LUX-ZEPLIN experiment to the $0\nu\beta\beta$ decay in ^{136}xe decay. *Physical Review C*, 102(1), 07 2020. doi:10.1103/physrevc.102.014602.

[A+20c] D. S. Akerib et al. Projected WIMP sensitivity of the LUX-ZEPLIN dark matter experiment. *Physical Review D*, 101(5), mar 2020. doi:10.1103/physrevd.101.052002.

[A+20d] D.S. Akerib et al. The lux-zeplin (lz) experiment. *Nuclear Instruments and Methods in Physics Research Section A: Accelerators, Spectrometers, Detectors and Associated Equipment*, 953:163047, 2020. URL: https://www.sciencedirect.com/science/article/pii/S0168900219314032, doi:https://doi.org/10.1016/j.nima.2019.163047.

[A+20e] E. Armengaud et al. The cupid-mo experiment for neutrinoless double-beta decay: performance and prospects. *The European Physical Journal C*, 80:44, 01 2020. doi:10.1140/epjc/s10052-019-7578-6.

[A+21a] D. Adams et al. High sensitivity neutrinoless double-beta decay search with one tonne-year of cuore data. 04 2021.

[A+21b] D. Adams et al. High sensitivity neutrinoless double-beta decay search with one tonne-year of cuore data. 04 2021.

[A+21c] D. S. Akerib et al. Projected sensitivity of the LUX-ZEPLIN experiment to the two-neutrino and neutrinoless double decays of ^{134}xe. *Physical Review C*, 104(6), dec 2021. doi:10.1103/physrevc.104.065501.

[A+21d] D.S. Akerib et al. Simulations of events for the lux-zeplin (lz) dark matter experiment. *Astroparticle Physics*, 125:102480, 2021. URL: https://www.sciencedirect.com/science/article/pii/S0927650520300529, doi:https://doi.org/10.1016/j.astropartphys.2020.102480.

[A+21e] E. Armengaud et al. New limit for neutrinoless double-beta decay of mo 100 from the cupid-mo experiment. *Physical Review Letters*, 126, 05 2021. doi:10.1103/PhysRevLett.126.181802.

[A+22a] J. Aalbers et al. Background determination for the lux-zeplin (lz) dark matter experiment, 2022. doi:10.48550/ARXIV.2211.17120.

[A+22b] J. Aalbers et al. First dark matter search results from the lux-zeplin (lz) experiment. 2022. doi:10.48550/ARXIV.2207.03764.

[A+22c] J Aalbers et al. A next-generation liquid xenon observatory for dark matter and neutrino physics. *Journal of Physics G: Nuclear and Particle Physics*, 50(1):013001, dec 2022. doi:10.1088/1361-6471/ac841a.

[A+22d] S. Abe et al. A search for correlated low-energy electron antineutrinos in kamland with gamma-ray bursts. *The Astrophysical Journal*, 927(1):69, 03 2022. doi:10.3847/1538-4357/ac4e7e.

[A+22e] D. S. Akerib et al. Snowmass2021 cosmic frontier dark matter direct detection to the neutrino fog, 2022. doi:10.48550/ARXIV.2203.08084.

[AD10] E. Aprile and T. Doke. Liquid xenon detectors for particle physics and astrophysics. *Reviews of Modern Physics*, 82(3):2053–2097, jul 2010. doi:10.1103/revmodphys.82.2053.

[B+21] E. Bodnia et al. The electric field dependence of single electron emission in the PIXeY two-phase xenon detector. *Journal of Instrumentation*, 16(12):P12015, dec 2021. doi:10.1088/1748-0221/16/12/p12015.

[Bah01] John N. Bahcall. How many σ's is the solar neutrino effect? *Physical Review C*, 65, 2001. doi:10.1103/PhysRevC.65.015802.

[Ben15] Giovanni Benato. Effective majorana mass and neutrinoless double beta decay. *The European Physical Journal C*, 75(11), nov 2015. doi:10.1140/epjc/s10052-015-3802-1.

[Bol99] A.I. Bolozdynya. Two-phase emission detectors and their applications. *Nuclear Instruments and Methods in Physics Research Section A: Accelerators, Spectrometers, Detectors and Associated Equipment*, 422(1):314–320, 1999. doi:https://doi.org/10.1016/S0168-9002(98)00965-6.

[C+98] Bruce T. Cleveland et al. Measurement of the solar electron neutrino flux with the homestake chlorine detector. *The Astrophysical Journal*, 496(1):505–526, mar 1998. doi:10.1086/305343.

[CA13] V Chepel and H Araújo. Liquid noble gas detectors for low energy particle physics. *Journal of Instrumentation*, 8(04):R04001–R04001, apr 2013. doi:10.1088/1748-0221/8/04/r04001.

[CDF21] Alice Campani, Valentina Dompè, and Guido Fantini. Status and perspectives on rare decay searches in tellurium isotopes. *Universe*, 7(7), 2021. URL: https://www.mdpi.com/2218-1997/7/7/212, doi:10.3390/universe7070212.

[com] The SciPy community. scipy.aptimize.Curve_Fit. https://docs.scipy.org/doc/scipy/reference/generated/scipy.optimize.curve_fit.html. last accessed at 26 January 2023.

[CS21] Carla Maria Cattadori and Francesco Salamida. Gerda and legend: Probing the neutrino nature and mass at 100 mev and beyond. *Universe*, 7(9), 2021. URL: https://www.mdpi.com/2218-1997/7/9/314, doi:10.3390/universe7090314.

[D+62] G. Danby et al. Observation of high-energy neutrino reactions and the existance of two kinds of neutrinos. *Physical Review Letters*, 9(1):36–44, 1962. doi:10.1103/PhysRevLett.9.36.

[D+14] Davide D'Angelo et al. Recent borexino results and prospects for the near future. *EPJ Web of Conferences*, 126, 2014. doi:10.1051/epjconf/201612602008.

[D+16] Stefano Dell'Oro et al. Neutrinoless double beta decay: 2015 review. *Advances in High Energy Physics*, 2016:1–37, 2016. doi:10.1155/2016/2162659.

[D+21] Valerio D'Andrea et al. Neutrinoless double beta decay with germanium detectors: 10^{26} yr and beyond. *Universe*, 7(9):341, 2021. doi:10.3390/universe7090341.

[DLL19] Ubaldo Dore, Pier Loverre, and Lucio Ludovici. History of accelerator neutrino beams. *The European Physical Journal H*, 44(4-5):271–305, oct 2019. doi:10.1140/epjh/e2019-90032-x.

[DLR15] Luigi Di Lella and Carlo Rubbia. The Discovery of the W and Z Particles. *Adv. Ser. Direct. High Energy Phys.*, 23:137–163, 2015. doi:10.1142/9789814644150_0006.

[DNN08] Sacha Davidson, Enrico Nardi, and Yosef Nir. Leptogenesis. *Physics Reports*, 466(4):105–177, 2008. URL: https://www.sciencedirect.com/science/article/pii/S0370157308001889, doi:10.1016/j.physrep.2008.06.002.

[DPR19] Michelle J. Dolinski, Alan W.P. Poon, and Werner Rodejohann. Neutrinoless double-beta decay: Status and prospects. *Annual Review of Nuclear and Particle Science*, 69(1):219–251, 2019. doi:10.1146/annurev-nucl-101918-023407.

[DS98] Arnon Dar and Giora Shaviv. The solar neutrino problem - an update. *Physics Reports*, (311):115–141, 1998. doi:10.1016/S0370-1573(98)00094-5.

[F+98] Y. Fukuda et al. Evidence for oscillation of atmospheric neutrinos. *Phys. Rev. Lett.*, 81:1562–1567, Aug 1998. URL: https://link.aps.org/doi/10.1103/PhysRevLett.81.1562, doi:10.1103/PhysRevLett.81.1562.

[FY86] M. Fukugita and T. Yanagida. Baryogenesis Without Grand Unification. *Phys. Lett. B*, 174:45–47, 1986. doi:10.1016/0370-2693(86)91126-3.

[GER17] GERDA Collaboration. Searching for neutrinoless double beta decay with gerda. *Nuclear Instruments and Methods in Physics Research Section A: Accelerators, Spectrometers, Detectors and Associated Equipment*, 958, 10 2017. doi:10.1016/j.nima.2019.04.066.

[GK07] Carlo Giunti and Chung W. Kim. *Fundamentals of Neutrino Physics and Astrophysics*. OUP Oxford, 2007.

[GLC19] I. S. Guinn and J. M. L'opez-Castano. Current status of legend: Searching for neutrinoless double-beta decay in 76ge. part ii. *Proceedings of XXIX International Symposium on Lepton Photon Interactions at High Energies — PoS(LeptonPhoton2019)*, 2019.

[GLZ18] C. Giganti, S. Lavignac, and M. Zito. Neutrino oscillations: The rise of the PMNS paradigm. *Progress in Particle and Nuclear Physics*, 98:1–54, jan 2018. doi:10.1016/j.ppnp.2017.10.001.

[GM35] M. Goeppert-Mayer. Double beta-disintegration. *Phys. Rev.*, 48:512–516, Sep 1935. URL: https://link.aps.org/doi/10.1103/PhysRev.48.512, doi:10.1103/PhysRev.48.512.

[Gri08] David Griffiths. *Introduction to Elementary Particles*. WILEY-VCH Verlang GmbH & Co. KGaA, 2008.

[Gro] UCL HEP Group. Supernemo. URL: https://www.hep.ucl.ac.uk/nemo/superNemo.shtml.

[Gro19] The Group. Cupid pre-cdr. 07 2019.

[Gó16] H. Gómez. Latest results of nemo-3 experiment and present status of supernemo. *Nuclear and Particle Physics Proceedings*, 273-275:1765–1770, 2016. URL: https://www.sciencedirect.com/science/article/pii/S2405601415007737, doi:10.1016/j.nuclphysbps.2015.09.284.

[IR50] Mark G. Inghram and John H. Reynolds. Double beta-decay of te^{130}. *Phys. Rev.*, 78:822–823, Jun 1950. URL: https://link.aps.org/doi/10.1103/PhysRev.78.822.2, doi:10.1103/PhysRev.78.822.2.

[Jer20] Andrea Jeremie. The supernemo demonstrator double beta experiment. *Nuclear Instruments and Methods in Physics Research Section A: Accelerators, Spectrometers, Detectors and Associated Equipment*, 958:162115, 2020. URL: https://www.sciencedirect.com/science/article/pii/S0168900219305431, doi:10.1016/j.nima.2019.04.069.

[K$^+$19] M. Kleesiek et al. β-decay spectrum, response function and statistical model for neutrino mass measurements with the katrin experiment. *The European Physical Journal C*, 79, 03 2019. doi:10.1140/epjc/s10052-019-6686-7.

[K$^+$22] F. Kuger et al. Prospects of charge signal analyses in liquid xenon TPCs with proportional scintillation in the liquid phase. *Journal of Instrumentation*, 17(03):P03027, mar 2022. doi:10.1088/1748-0221/17/03/p03027.

[Kaj16] Takaaki Kajita. Nobel lecture: Discovery of atmospheric neutrino oscillations. *Rev. Mod. Phys.*, 88:030501, Jul 2016. URL: https://link.aps.org/doi/10.1103/RevModPhys.88.030501, doi:10.1103/RevModPhys.88.030501.

[KN12] Takaaki Kajita and Koichiro Nishikawa. Atmospheric neutrinos. *Advances in High Energy Physics*, 2012, 2012. doi:10.1155/2012/504715.

[Kra88] Kenneth S Krane. *Introductory nuclear physics*. Wiley, New York, NY, 1988. URL: https://cds.cern.ch/record/359790.

[KS88] S.Yu. Khlebnikov and M.E. Shaposhnikov. The statistical theory of anomalous fermion number non-conservation. *Nuclear Physics B*, 308(4):885–912, 1988. URL: https://www.sciencedirect.com/science/article/pii/0550321388901332, doi:10.1016/0550-3213(88)90133-2.

[L20] Legend-200. Accessed: 2022-08-15. URL: https://legend-exp.org/science/legend-pathway/legend-200.

[LEG21] LEGEND Collaboration. Legend-1000 preconceptual design report. 07 2021.

[Li21] Aobo Li. (kamland)-zen 800 status and prospect with the artificial intelligence powered analysis. *Journal of Physics: Conference Series*, 2156(1):012114, 12 2021. doi:10.1088/1742-6596/2156/1/012114.

[Lu21] Jun Lu. A rigorous introduction to linear models, 2021. doi:10.48550/ARXIV.2105.04240.

[M+17] B. J. Mount et al. LUX-ZEPLIN (LZ) Technical Design Report. 3 2017. arXiv:1703.09144.

[MA+15] J. Martín-Albo et al. Sensitivity of next-100 to neutrinoless double beta decay. *Journal of High Energy Physics*, 2016, 11 2015. doi:10.1007/JHEP05(2016)159.

[N+17] F. Neves et al. Measurement of the absolute reflectance of polytetrafluoroethylene (PTFE) immersed in liquid xenon. *Journal of Instrumentation*, 12(01):P01017–P01017, jan 2017. doi:10.1088/1748-0221/12/01/p01017.

[nEX18] nEXO Collaboration. nexo pre-conceptual design report. 05 2018.

[NIS] NIST. Nist/sematech e-handbook of statistical methods. https://www.itl.nist.gov/div898/handbook/pmd/section1/pmd142.htm. accessed at 21/01/2023. doi:10.18434/M32189.

[Pah08] R. B. Pahlka. The supernemo experiment. 2008. URL: https://arxiv.org/abs/0810.3169, doi:10.48550/arXiv.0810.3169.

[Pat01] Thomas Patzak. First direct observation of the tau neutrino. *Europhysics News*, 32:56–57, 03 2001. doi:10.1051/epn:2001205.

[Per22] Guilherme Pereira. Energy resolution of the lz detector for high-energy electronic recoils. LIDINE 2022 conference, September 23, 2022.

[QV15] X. Qian and P. Vogel. Neutrino mass hierarchy. *Progress in Particle and Nuclear Physics*, 83:1–30, jul 2015. doi:10.1016/j.ppnp.2015.05.002.

[RC53] F. Reines and C. L. Cowan. Detection of the free neutrino. *Phys. Rev.*, 92:830–831, Nov 1953. URL: https://link.aps.org/doi/10.1103/PhysRev.92.830, doi:10.1103/PhysRev.92.830.

[Rio11] Antonio Riotto. Baryogenesis and leptogenesis. *Journal of Physics: Conference Series*, 335(1):012008, dec 2011. URL: https://dx.doi.org/10.1088/1742-6596/335/1/012008, doi:10.1088/1742-6596/335/1/012008.

[Saa13] Ruben Saakyan. Two-neutrino double-beta decay. *Anual Review of Nuclear and Particle Science*, 2013(63):503–29, 2013. doi:10.1146/annurev-nucl-102711-094904.

[SftKZC17] Junpei Shirai and for the KamLAND-Zen Collaboratio. Results and future plans for the kamland-zen experiment. *Journal of Physics: Conference Series*, 888:012031, 09 2017. doi:10.1088/1742-6596/888/1/012031.

[SK18] P. Sorensen and K. Kamdin. Two distinct components of the delayed single electron noise in liquid xenon emission detectors. *Journal of Instrumentation*, 13(02):P02032–P02032, feb 2018. doi:10.1088/1748-0221/13/02/p02032.

[Smi03] A. Yu. Smirnov. The msw effect and solar neutrinos, 2003. doi:10.48550/ARXIV.HEP-PH/0305106.

[Sor11] Peter Sorensen. Anisotropic diffusion of electrons in liquid xenon with application to improving the sensitivity of direct dark matter searches. *Nuclear Instruments and Methods in Physics Research Section A: Accelerators, Spectrometers, Detectors and Associated Equipment*, 635(1):41–43, apr 2011. doi:10.1016/j.nima.2011.01.089.

[SŠF96] J. Schwieger, F. Šimkovic, and Amand Faessler. The pauli principle, QRPA and the two-neutrino double beta decay. *Nuclear Physics A*, 600(2):179–192, apr 1996. URL: https://doi.org/10.48550/arXiv.nucl-th/9602032, doi:10.1016/0375-9474(96)00024-3.

[Vag19] Sunny Vagnozzi. *Weight them all! - Cosmological searches for the neutrino mass scale and mass ordering*. PhD thesis, 06 2019.

[Zen22] Zen Collaboration. First search for the majorana nature of neutrinos in the inverted mass ordering region with kamland-zen. 2022. URL: https://arxiv.org/abs/2203.02139, doi:10.48550/ARXIV.2203.02139.

List of Figures

List of Tables